Quantum Optomechanics with Engineered Membrane Resonators

by

Pen-Li Yu

B.S., National Taiwan University, 2007

A thesis submitted to the

Faculty of the Graduate School of the

University of Colorado in partial fulfillment

of the requirements for the degree of

Doctor of Philosophy

Department of Physics

2016

This thesis entitled:
Quantum Optomechanics with Engineered Membrane Resonators
written by Pen-Li Yu
has been approved for the Department of Physics

Cindy Regal

Konrad Lehnert

Date _____

The final copy of this thesis has been examined by the signatories, and we find that both the content and the form meet acceptable presentation standards of scholarly work in the above mentioned discipline.

Yu, Pen-Li (Ph.D., Physics)

Quantum Optomechanics with Engineered Membrane Resonators

Thesis directed by Prof. Cindy Regal

Mechanical oscillators coupled to an electromagnetic cavity have emerged as a new frontier in quantum optics. This coupling presents an opportunity for manipulating the quantum state of light, connecting different quantum resources, and ultra-sensitive force detectors. A particular enabling platform utilizes high-stress silicon-nitride membrane resonators. Because of its large tensile stress, the membrane exhibits remarkable mechanical quality factors (Qs) that are even higher than that of single crystalline silicon. The membrane with such high Q combined with robust cryogenic Fabry-Perot cavity enables a variety of quantum optics experiments, such as squeezed light generation. Improving upon these encouraging results requires understanding and engineering the membrane resonators. The membrane dissipation can be classified as the internal loss and the external loss. We are able to manage the internal loss of a hybrid membrane with a curvature map, and control the external loss of a membrane with a phononic crystal (PnC) shield. In this dissertation, I will present squeezed light generation, our studies and engineering of high-stress membrane mechanics, and optomechanical Raman-ratio thermometry with a PnC-isolated membrane.

Dedication

To my best friend and dearest wife, Bethany Huo.

Acknowledgements

I am very grateful to my advisor Cindy Regal, who thoughtfully, wisely, and efficiently guided the overall development of my thesis work. I also thank Thomas Purdy for his humor and hands-on help. I thank Nir Kampel for valuable insights. I am grateful for Katrina Cicak's awesome fabrication. I especially wish to thank Yeghishe Tsaturyan for creative input. I also want to thank Robert Peterson for delightful discussions. I thank Adam Kaufman and Brian Lester for creating a relaxed community. I thank every staff in JILA for being so supportive. David Alchenberger, Hans Green, Blaine Horner, and J.R. Raith are enormously appreciated. I am very proud to work in this vibrant and creative environment. I will always be a JILAn!

Contents

Chapter

Chapter 1

Introduction

Mechanical oscillators coupled to an electromagnetic cavity have emerged as a new frontier in quantum optics. This coupling presents an opportunity for manipulating the quantum state of light, connecting different quantum resources, studying quantum measurement back-action in the optical detection of macroscopic objects, and ultra sensitive force detectors. A diverse suite of quantum optomechanical systems have been developed, covering nearly 20 orders of magnitude in effective mass and 10 orders of magnitude in frequency [1]. A particular enabling platform utilizing high-stress silicon-nitride membrane resonator was introduced by the Harris group in 2008 [2, 3]. In this realization, a membrane is placed in a standard high-finesse Fabry-Perot cavity. The silicon nitride membrane exhibits remarkable mechanical quality factors (Qs) that are even higher than that of single crystalline silicon. Because of their large tensile stress, Si_3N_4 membranes can have Q-frequency products exceed 10^{14} Hz.

Membranes with such high Q combined within robust cryogenic Fabry-Perot cavity [4] have proven fruitful. Our lab focuses on making cryogenically compatible membrane optomechanics devices where thermal effects can be reduced and quantum aspects of the optomechanical system revealed. Our experiments can often be discussed using a common metric for ones ability to reach a quantum limit. We define an optomechanical cooperativity as $C = 4G^2/\kappa\gamma_m$, where G is the many-photon optomechanical coupling, κ is the cavity linewidth, and γ_m is the mechanical dissipation (these parameters will be defined in more

detail later). Cooperativity greater than the thermal phonon occupancy (n_{th}) enables a variety of experiments: observation of quantum measurement backaction [5], squeezed light generation [6], cooling the mechanical mode to its motional ground state [7], and microwave to optical frequency conversion [8].

Improving upon these encouraging results and exploring new directions requires understanding and engineering the membrane resonators. Early work in my dissertation focused on understanding tensioned membrane resonators whose quality factors and their dependences were not clear to the optomechanics community [9, 10, 11, 12, 13]. These studies focused on investigating both internal loss and external loss-mechanisms, and have resulted in important predictive power. In this thesis, I show how we are able to manage the internal loss of a hybrid membrane by understanding a spatial map of the curvature of a membrane [14], and we control the external loss of a membrane by creating a phononic crystal (PnC) shield [15, 16]. I have also been involved in the optomechanics experiments within the larger group; I worked on our study of squeezed light generation [6], and in this dissertation I elaborate on how to understand the ponderomotive squeezing we realized. As a final goal of my dissertation work, I wanted to show that engineered membranes can have a positive impact on quantum cavity optomechanics experiments. This was realized in our experiments on optomechanical Raman-Ratio thermometry with a PnC-isolated membrane that I present in this dissertation [7, 4]. Lastly, as I discuss in the outlook, the PnC-isolated membranes are seeing application in a number of new experiments in progress.

1.1 Outline

1.1.1 High Stress Membrane Mechanics

Tension in the Si_3N_4 membrane strongly alters its dynamics. A variety of loss mechanisms considered extensively for untensioned resonators in the fields of micro- and nanoelectromechanical systems (MEMS and NEMS) required analysis in the large stress regime.

Around 2010, the internal loss in this regime (loss associated with the elasticity of the resonator), is first analyzed by scientists in the context of silicon nitride strings [11, 12]. In Chapter 2, we develop a theoretical model to interprets our results of the 2-dimensional Si_3N_4 membranes with and without a metallic layer. We focus on the spatial dependence of the internal loss and experimentally verify the prediction from the model that the damping can be reduced significantly by patterning the metal film.

In Chapter 3, we investigate the external loss, loss associated with the surrounding environment of the Si_3N_4 membrane. I provide two intuitive physical pictures, and support them with experimental and simulation results. In Chapter 4, I extend these pictures to design, measure, and understand a membrane mechanical resonator in a PnC I design. A unique aspect of our PnC design is it allows us to preserve the high tension of the membrane.

1.1.2 Generation of Squeezed Light

In Chapter 5 we investigate optomechanical squeezed light. The squeezing experiment would be an important demonstration of the capabilities of manipulating the quantum state of light. It is a natural extension of the RPSN work described in Ref. [5]. We first discuss the physics of ponderomotive squeezing in the context of Kerr squeezing. We show that the nonlinearity, described by the magnitude of the complex Kerr coefficient, can be approximated as the optomechanical cooperativity. We experimentally realize $C/n_{\mathrm{th}} \sim 5$ and demonstrate strong and continuous optomechanical squeezing of 1.7 ± 0.2 dB below the shot-noise level. The observed squeezing spectra suffer from the thermal noise of the substrate modes, and hence the results are a good example of experiments that will be improved in the future by PnC membrane devices. The peak level of squeezing measured near the mechanical resonance is well described by a model whose parameters are independently calibrated and that includes thermal motion of the membrane with no other classical noise sources.

1.1.3 Raman-Ratio Thermometry

In Chapter 6, with a PnC-isolated membrane, we investigate using Raman sideband asymmetry observed for a membrane with low phonon occupation for the measurement of effective and physical temperatures of the membrane. Exceptionally good isolation from the environment by the PnC allows us to perform this thermometry at variety of environment temperatures. In addition to the thermometry, this experiment also demonstrates near ground state cooling of a membrane mechanical resonator.

Chapter 2

Internal Loss of High-Stress Membrane Resonator

2.1 Introduction

The dynamics of the high-stress membranes have many qualitative differences from the more typical flexural mode resonators. For examples, the resonant frequency of our high-stress Si_3N_4 membrane is 1000 times larger than a non-stressed plate resonator with the same dimension. These high-stress resonators are found to have remarkable mechanical Qs, but their dependences on the stress was not always clear to the MEMS and optomechanics community [9, 10]. For the case of Si_3N_4string, an elastic model including the stress effect was verified quantitatively in the experiments of Ref. [11, 12]. The loss energy was found to be proportional to the bending energy and observed to change much less than the total energy as the stress increased.

In this chapter, I investigate the internal loss of the 2D high-stress membranes. As discussed in Chapter 3, we believe that in much of our work with pure Si_3N_4 membranes we are limited by external loss, but internal loss is also imperative to understand quantitatively. By coating ultrahigh-Q Si_3N_4 membranes with a more lossy metal, we can precisely measure the effect of material loss on Q's of mechanical modes over a large range of frequencies. We can also examine the spatial dependence of loss by patterning the coated metal. We develop a theoretical model that interprets our results and predicts the damping can be reduced significantly by patterning the metal film. Using such patterning, we fabricate Al-Si_3N_4 membranes with ultrahigh Q at room temperature. Our work elucidates the role of material

loss in the Q of high-stress membrane resonators.

In addition, this work informs the design of hybrid mechanical oscillators for optical-electrical-mechanical quantum interfaces. A variety of proposed cavity mechanics experiments would be enabled by the addition of a metallic layer to Si_3N_4 while maintaining high Q [17, 18, 19, 20]. Foremost, a metallic membrane section could form a capacitor plate that couples to a microwave LC resonator; in fact, pure metallic drums have recently been ground-state cooled using a combination of cryogenic and microwave cavity cooling [17]. With a hybrid dielectric/metallic membrane, one could couple mechanical motion simultaneously to optical light and a microwave electrical circuit in the quantum regime [18]. Such a device could solve the difficult, yet crucial, problem of transferring quantum states between microwave and optical photons. It could also enable enhanced detection of excitations in a room-temperature electrical circuit via photodetection [19]. Further, a magnetic metallic film could be used for magnetic coupling of spins to membrane motion [20]. However, the success of these applications will hinge on creating hybrid membranes with a sufficiently high quality factor at relevant temperatures.

2.2 Quality Factors of High-Stress, Fully Metalized Membranes

To distinguish the material loss and the external loss of a metalized membrane, we first measured the Q's of pure Si_3N_4 membranes. We use 50 nm-thick stoichiometric LPCVD nitride membranes that are supported by a 200 μm-thick silicon frame (from Norcada Inc.). The membranes are in a square geometry of side length l=0.5 mm or 1 mm with tensile stress $\sigma\sim$0.9 GPa and mass density $\rho\sim$2.7 g/cm^3. The membrane mode shapes are given by approximately sinusoidal functions like those shown in Fig. 2.1(b) with resonant frequencies $f_{mn} \sim \sqrt{\sigma(m^2+n^2)/4\rho l^2}$, where m, n are the integer mode indices representing the number of antinodes. The silicon frame is glued at three corners to a metal form on a piezoelectric actuator. To probe the mechanical displacement, we position the membrane at the end of one arm of a Michelson interferometer. We characterize the mechanical quality factor by

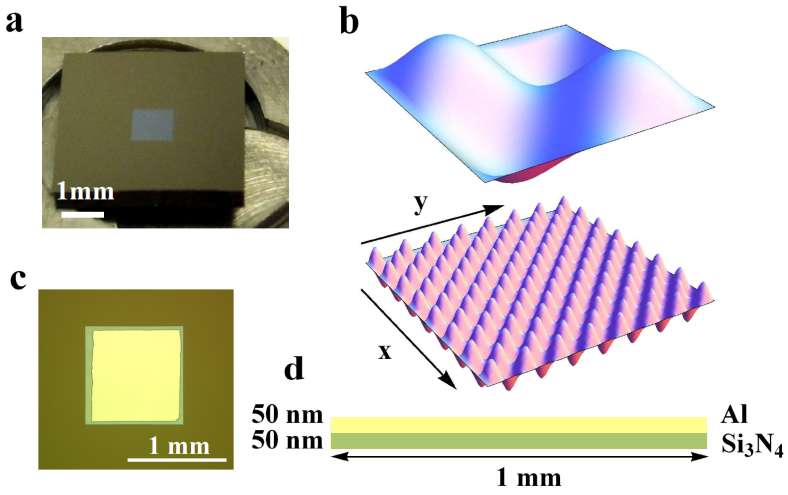

Figure 2.1: Geometry of membrane modes. (a) Image of a 1 mm membrane in its silicon frame. (b) Illustrations of the $(m, n) = (2, 2)$ and $(15, 15)$ modes. (c) Image of a patterned Al film on top of Si_3N_4. The central square is Al and the rim is Si_3N_4 suspended on a Si frame. (d) Schematic diagram of the Al/Si_3N_4 bilayer membrane (50 nm Al and 50 nm Si_3N_4).

monitoring the ringdown of the mechanical excitation in vacuum of less than 10^{-6} torr.

We deposit 50 nm of Al using e-beam evaporation on top of the pure Si_3N_4 membrane measured in Fig. 2.2(a) (green points). The membrane remains under large tensile stress, but adding the additional film does decrease the effective stress to $\sigma_{\text{eff}} = 0.35$ GPa. With the addition of the metal, we see a drop in Q to a maximum of $\sim 2 \times 10^5$ as shown in Fig. 2.2(a). By drawing on our knowledge of the Q's of the pure Si_3N_4 membrane [Fig. 2(b)], we can clearly distinguish material loss and external loss (See Chapter 3). The open squares in Fig. 2.2(a) represent the asymmetric modes found to be radiation-loss limited for the pure Si_3N_4 membrane. If we remove these points from the Al-Si_3N_4 membrane measurements, we arrive at a clean set of points (closed squares) representing the material loss-limited Q as a function of frequency. Damping rates $\gamma = 2\pi f/Q$ for two datasets obtained using this method are shown in Fig. 2.2(b).

We have developed a theoretical framework to describe the frequency dependence of

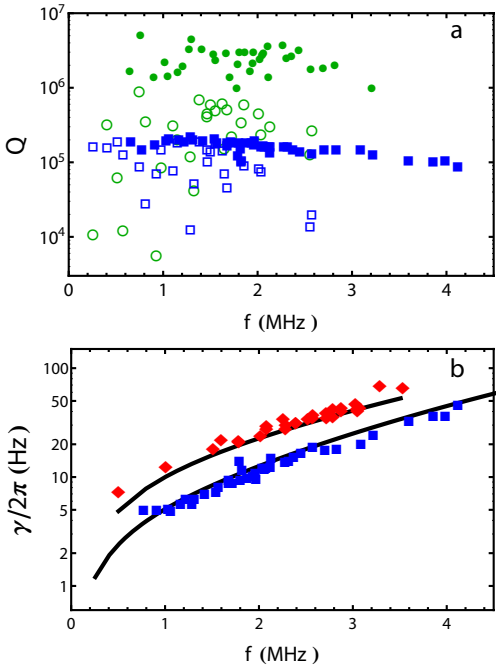

Figure 2.2: Extracting the material loss-limited Q. (a) Measured quality factors of a square Si_3N_4 membrane before (green circles) and after (blue squares) adding a 50 nm film of Al. The modes limited (not limited) by radiation loss are marked by open (closed) circles. The data are plotted as a function of frequency measured after adding the Al. (b) Mechanical linewidth of the modes limited by the material loss of Al for 0.5×0.5 mm (red diamonds) and 1×1 mm (blue squares) membranes. To compare to theory, we calculate the damping rate $\gamma_{mn}/2\pi$ for each mode, and the points are connected with the displayed lines.

the material loss-limited quality factors of our two-dimensional structures. We model the membrane as an anelastic plate that dissipates mechanical energy under cyclic loading [21]. Under oscillation, the material's strains and stresses are not in phase, and the energy supplied by the out-of-phase stresses is converted irreversibly to heat. This picture has been successfully developed to understand damping in one dimensional Si_3N_4 strings [11, 12].

In our case, we start by applying standard plate theory with an in-plane force [22], i.e., under tensile stress, to determine the normal modes. The modes must satisfy the boundary conditions of the clamped plate $W{=}(\partial/\partial x)W{=}0$ or $W{=}(\partial/\partial y)W{=}0$ for all four edges. We express the 2D mode function $W_{mn}(x, y)$ as a product of stressed-beam functions

$u_m(x)u_n(y)$. We have verified the accuracy of this description via perturbation theory (see appendix A). We use a closed-form expression for the function $u_n(x)$:

$$u_m(x) = \begin{cases} v_m(x), & 0 \le x \le \frac{l}{2} \\ (-1)^{m+1} v_m(l-x), & \frac{l}{2} < x \le l \end{cases} \tag{2.1}$$

$$v_m(x) = \sqrt{2a}\left\{\sin\left[\frac{m\pi x}{l}\right] + \frac{\lambda m\pi}{2}\left(\exp\left[\frac{-x}{\lambda l/2}\right] - \cos\left[\frac{m\pi x}{l}\right]\right)\right\} \tag{2.2}$$

$$\omega_m \sim \frac{m\pi}{l}\sqrt{\frac{\sigma}{\rho}}. \tag{2.3}$$

It is a sinusoid with an exponential correction near the edge for the clamped boundary condition.

For each mode, we can calculate the loss due to anelasticity. The oscillation of the plate induces oscillating strains $\varepsilon_{xx}e^{i\omega t}, \varepsilon_{yy}e^{i\omega t}$, and $\varepsilon_{xy}e^{i\omega t}$, and the accompanying stresses are given by the usual constitutive equation of classical plate [23] with the complex Young's modulus $\tilde{E} = E_1 + iE_2$, where E_2 is called the loss modulus. During one cycle, the full expression for the energy lost is

$$\Delta U = \int \frac{2\pi E_2(x,y)}{1+\nu}\Big\{\frac{(\varepsilon_{xx}+\varepsilon_{yy})^2}{2(1-\nu)} + \frac{\varepsilon_{xy}^2}{4} - \varepsilon_{xx}\varepsilon_{yy}\Big\}dV \tag{2.4}$$

where ν is the Poisson's ratio (see appendix A). Note, the strain term $\varepsilon_{xx} = -z(\partial^2 W/\partial x^2)$ is proportional to the curvature of the mode function. To calculate the quality factor, we also need an expression for the total stored energy. It can be obtained from the maximum kinetic energy $U = 2\rho\pi^2 f^2 \int W(x,y)^2 dV$. The quality factor for a particular mode W_{mn} is then given by $Q_{mn} = 2\pi U_{mn}/\Delta U_{mn}$.

We start by using our theory to calculate the damping of fully-metalized membranes. We apply a least-squares fit to the two datasets (two different-sized membranes) in Fig. 2.2(b) assuming a single frequency-independent loss modulus. This reveals an effective bilayer $E_2 = 0.55$ GPa. The corresponding Al loss modulus is consistent with typical values for thin-film polycrystalline Al at room temperature, as measured, for example, via depositing

Al on a low-loss Si cantilever [24]. The presumed microscopic origin of the loss is related to crystallographic defects such as grain boundary sliding [25, 26] or kinks on dislocations [27]. Despite this underlying complexity, our model assumes very little about the microscopic origin of the loss. Namely, we assume that the defects are uniformly distributed within the deposited metal in the x and y directions. We also assume the temperature stays sufficiently constant in our measurements so as not to affect the loss modulus. We have verified that the heating due to our measurement laser of power 150 μW is not a significant effect by measuring constant quality factors as the power is varied from 10 to 900 μW.

2.3 Discussion: High-Stress Membrane Mechanics

With continued analysis of the theory we can not only model, but understand the Q dependencies seen in Fig. 2.2, and put our observations in the context of other studies in 1D and 2D [28, 29, 11, 12]. We would like to understand: (1) The frequency dependencies, i.e., why an extremely corrugated mode has only a slightly lower Q than the fundamental mode in our measurements (2) The geometry dependence, i.e., how damping should scale with resonator size. First, we address the frequency dependence. As noted above in the discussion of Eq. (1), the loss is given by an integral of terms proportional to the mode curvatures. We identify two contributions to the curvature, namely that induced at the clamped edge and that near the antinodes in the interior of the membrane. If the curvature at the edge dominates we expect a flat Q as a function of frequency, or if the antinode contribution dominates we expect a decreasing Q as the frequency (and correspondingly the number of antinodes) increases. We quantify these statements by deriving a simplified expression for Q as a function of mode indices m and n for the limit of (1) an isotropic membrane, i.e. constant E_2 in x and y and (2) high-stress quantified by small λm and λn where $\lambda = \sqrt{E'h^2/3\sigma l^2}$ is a dimensionless stress parameter. Here $E' = E_1/(1-\nu^2)$ and h, l, and σ are the height, length, and stress of the membrane respectively. In these limits, Eq. (1) becomes an integral over squared sinusoidal terms (antinode contribution) and an

exponential term (edge contribution) to give a total Q of (see appendix A)

$$Q_{mn} \sim \frac{1}{\lambda}\frac{E_1}{E_2}\left(\underbrace{1}_{\text{edge}} + \underbrace{\lambda\frac{(m^2+n^2)\pi^2}{4}}_{\text{antinode}}\right)^{-1} \tag{2.5}$$

The term $\lambda(m^2+n^2)\pi^2/4$ determines whether there will be a frequency-dependent Q. For our experiments, and similar experiments with large membranes [28, 29], $\lambda \sim 10^{-4}$–10^{-3}, and hence we expect a relatively flat Q. However, if the edge length is decreased, λ increases and the antinode contribution can become large. Hence, a frequency dependence appears for experiments such as those in Ref. [11] where shorter strings (< 35 μm) are used.

Further, the prefactor $1/\lambda$ in Eq. (2) determines the geometry and stress dependence for the Q of the fundamental mode. Physically, λ can be written as the ratio of bending energy to elongation energy (see appendix A), and as discussed in Ref. [11], exciting energy in the form of elongation energy rather than bending energy leads to higher Q. More concretely, based upon Eq. (2), we predict that if the membrane side length l is doubled, Q of the fundamental mode will double for the same loss modulus, and this is exactly what is observed in Fig. 2.2(b); the analogous effect in 1D was observed in Ref. [11]. We also see that as the stress is varied, Q scales with $\sqrt{\sigma}$, and hence the linewidth $\gamma = 2\pi f/Q$ remains constant. While Eq. (2) only holds in the stressed limit, a calculation in the zero stress (flexural) limit reveals the linewidth increases by a only a few factors from the highly-stressed case.

2.4 Ultrahigh-Q Metallized Membrane by Avoiding the Edge Curvature

Our analysis above indicates that by making the loss modulus near the membrane edge small, we can reduce the loss significantly. Using our ability to control the addition of material loss with the Al film, we can directly test this prediction. The inset to Fig. 2.1(c) shows a 1×1 mm membrane where we deposited Al nearly everywhere except in a small $\sim$50 μm region near the edge. The quality factors of this membrane were measured to be dramatically higher (blue circles) than a control experiment (red squares) in which an

identical layer of Al was deposited everywhere on a separate membrane (Fig. 2.3). For these data we show the Q's measured for all modes, but identify the lower-Q asymmetric modes by open circles or squares. For both datasets in Fig. 2.3 we anneal the membranes at 340° C after depositing the Al film resulting in an effective stress of $\sigma_{\text{eff}} = 0.6$ GPa. While annealing was not necessary for studying the fully-metallized membranes of Fig. 2.2, the unequal stress of the Al film in the partially-metallized membrane makes the higher-order modes difficult to identify. The annealing mitigates this problem, but we still cannot identify modes past 3 MHz. Hence past this point we analyze the Q envelope by measuring the highest Q mode in every 50 kHz window.

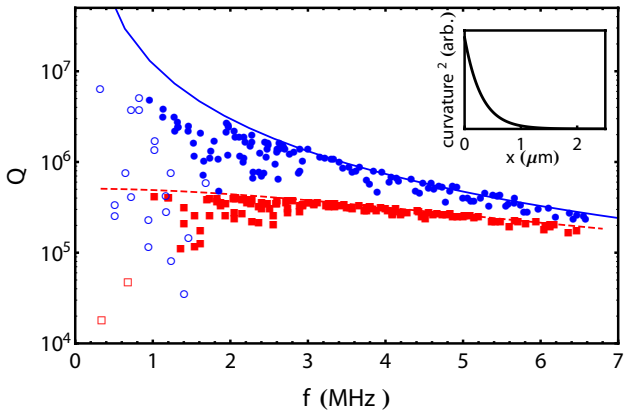

Figure 2.3: Ultrahigh-Q metal-covered membranes. Measured quality factors of two Si_3N_4 membranes with Al everywhere but near the edge of the membrane (blue circles) [see Fig. 2.1(c)] and a full film of Al as a control experiment (red squares). Asymmetric modes (with one mode index less than or equal to two) are marked by open circles or open squares. Calculated quality factors for each geometry are shown by the two lines; a single loss modulus is used for both. (Inset) The square of the curvature of a stressed mode as a function of distance along one coordinate of the membrane. This function decays exponentially near the membrane edge.

We can again apply our theory to quantitatively predict the Q for this new geometry. Since E_2 now becomes a function of position on the membrane, we return to using the full expression of Eq. (1). We assign a finite loss modulus for the Al region and zero loss for the Si_3N_4 rim. We approximate the mode functions as those expected for a uniformly stressed

membrane. This reveals the solid line in Fig. 2.3, which we find scales as $1/n^2$ for diagonal modes, as expected from antinode contributions. The dashed line shows the corresponding result for the fully metallized membrane using the same loss modulus. (The loss modulus found here is $E_2 = 0.3$ GPa, which is a smaller value than for Fig. 2.2 due to the annealing.) We find the theory successfully traces out the envelope of the measured Q's. The lowest order modes of the partially-metallized membrane reach as high as $Q = 6.5 \times 10^6$; this falls short of the predicted Q just from Al material loss (blue line) likely because these modes are now again limited by radiation loss (see Chapter 3). In comparison, recent measurements of metal microstrings at room temperature revealed Q's of $10^3 - 10^5$ [30, 31], and even at cryogenic temperatures, where the metal's material loss is significantly reduced, observed Q values for tensioned microresonators are typically $10^5 - 10^6$ [32, 33, 27, 17].

It is elucidating to understand what would happen to the Q trends we observe for the partially-metallized membrane upon varying the membrane stress. This requires analysis of the spatial dependence of the mode curvature in the membrane plane. In the inset to Fig. 2.3 we see the high-curvature area only occupies a very small $\sim$1 μm region near the edge of a high-tension membrane (here we use our lowest $\sigma_{\text{eff}} = 0.35$ GPa); specifically, the decay length is $\lambda l/4$ (see appendix A). As the stress is reduced (and hence λ is larger), the mode curvature becomes more uniformly distributed over the membrane plane. Hence we would not expect a dramatic difference in Q for a purely flexural mode when avoiding lossy material only at the edge.

The localized mode curvature of the tensioned membrane that we observe provides insight into a variety of membrane applications. Note for higher-order two-dimensional modes the curvature varies along the edge of the membrane, i.e. there are low-curvature regions near the nodes at the membrane edge (see appendix A). Thus, to create an electrical link between a central metallized patch and external circuits, and maintain high-Q performance, one could tailor metal connections to match up with the low-curvature regions near nodes at the membrane edge (see appendix A). Further, membrane patterning via holes is a promis-

ing technique to increase reflectivity of membranes for optomechanics experiments, but like metal deposition, also has potential to introduce defects. A full understanding of the mode curvature of the two-dimensional membrane is important for understanding the change in Q, or a lack of a decrease in Q, in recent patterning experiments [34, 35].

Chapter 3

External Loss of High-Stress Membrane Resonators

External loss is loss associated with the structure surrounding the resonator. Specifically, in our system, the structure is the supported silicon frame and the epoxy [see Fig. 3.1(a)]. The finite elastic coupling between the membrane and the silicon frame enables a dissipation channel and extraneous noise. It is an important limitation to the mechanical dissipation, and hence the optomechanical cooperativity. These experiments include the ponderomotive squeezing studied in chapter 5, optomechanical cooling, and optomechanical Raman-ratio thermometer discussed in chapter 6. In this chapter, I describe two physical pictures of the external loss [Fig. 3.1(b)-(c)], and provide theory, simulation, and experimental evidences. These two pictures are equivalent to some extent and complimentary to each other. The understanding and observation of the external loss led to the project of phononic crystal (PnC) that is discussed in chapter 4.

3.1 Picture I: Radiation Loss

The most intuitive picture of the external coupling is radiation loss. In this picture, we have a vibrating membrane and an infinitely large surrounding structure. As the membrane oscillates, it radiates acoustic energy through generating elastic waves on the surrounding structure. The energy is lost because the waves never return. They go off to infinity or realistically are absorbed by lossy material (such as epoxy) surrounding the finite-sized supporting structure.

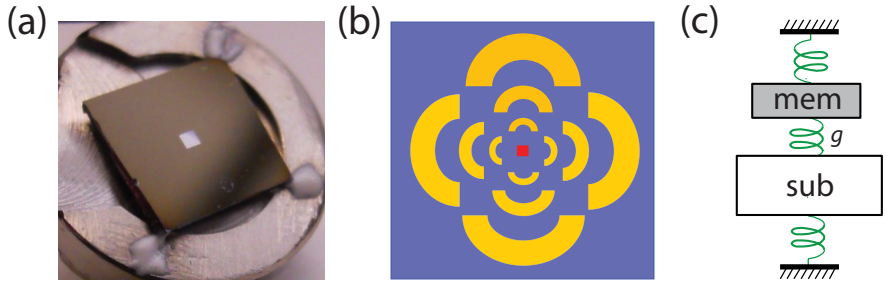

Figure 3.1: Basics of the external loss. (a) Photograph of a glued Si_3N_4 device. The semi-transparent square in the center is the Si_3N_4 membrane. The black chip is the silicon frame. The white globules in the three corners are epoxy. (b) Cartoon picture of the radiation loss. Oscillating membrane (red) radiates elastic waves (yellow) on the supporting substrate (purple). (c) Coupled-modes model. The energy of the membrane mode (labeled as 'mem') is dissipated through coupling to the substrate mode (labeled as 'sub'). The spring between them represent the coupling between the two modes.

The radiation loss is expected to be low for symmetric modes ($n = m$) and high for asymmetric modes ($n \neq m$ and $n = 1$ or $m = 1$). Therefore the radiation-loss-limited Qs as a function of mode frequencies are non-monotonic. This trend was first studied by Ignacio Wilson-rae and the Parpia group in Cornell [28]. This expectation can be understood by the destructive interference of the elastic waves. We can think of the antinodes near the periphery as point radiators with alternating π phase. Therefore, a more symmetric mode generates higher-order destructive interference. One expectation from this picture is that the symmetric modes with even number indices have even lower radiation loss because the total force applied on the surrounding environment is zero. Specifically, $(2, 2)$ mode and $(4, 4)$ mode are expected to have higher Q compared with $(3, 3)$ and $(5, 5)$. This parity dependence is roughly consistent with our observations when the membrane are glued at four corners.

An analytic expression of the radiation loss for high-stress, square membrane resonators is given by [28, 36, 37]:

$$Q_{mn}^{\mathrm{rad}} = \alpha \frac{1}{16\pi} \frac{\sqrt{n^2+m^2}}{n^2 m^2} \left[\frac{1}{n^4} + \frac{1}{m^4}\right]^{-1} \frac{l}{h} \frac{\rho_s}{\rho_r}, \tag{3.1}$$

where ρ_s and ρ_r are the mass densities of the substrate and the membrane, respectively. The

prefactor α is a geometry-independent constant representing the acoustic mismatch between the membrane and the substrate. As expected, the radiation loss is minimal at $n = m$. It is is maximal when $n = 1$ or $m = 1$ and $n \neq m$. However, this model predicts that $Q_{nn} \propto n$, regardless of the parity. It is worthwhile to note that in this expression, the radiation-loss limited Q scales with the aspect ratio l/h.

3.2 Picture II: Hybridization of the Membrane Modes and the Substrate Modes

Another picture of the external loss employs a coupled-oscillator model [Fig. 3.1(c)]. The two coupled modes are the membrane mode and the mechanical mode of the substrate. The coupling enable the two modes to exchange energy when their resonant frequencies are close to each other [29]. The energy of the membrane mode can then dissipated through the mechanical loss of the substrate. The loss could be large if a fair amount of epoxy is applied to the substrate. This coupled-modes picture is equivalent to the radiation-loss picture because mechanical modes of the substrate are needed to carry radiated elastic waves. The symmetry of the membrane modes determine the coupling strength between the substrate mode and the membrane mode

In addition to an extra loss channel, the hybridization leads to extra mechanical modes in the spectrum of the membrane. These non-membrane modes have been observed and limited optomechanical effects such as ground state cooling and ponderomotive squeezing discussed in chapter 5 and Ref. [5]. The non-membrane modes have a large effective mass and hence can always clearly distinguish between low-mass membrane modes and modes that have a substrate component. The non-membrane modes are discussed in more detail in Chapter 4.

3.3 Experimental Evidence I: Qs Depend on the Mode Shape Symmetry.

To probe the mechanical Q, we position the membrane at the end of one arm of a Michelson interferometer as described in Chapter 2. As shown in Fig. 3.2, we have the ability to measure the quality factors of many modes (up to 150) with different symmetries and to confidently assign a mode (m, n) to all measured points. When the data are plotted versus resonant frequency [green circles in Fig. 3.2(c)], the Q is non-monotonic. However, when the data are plotted as a function of mode index in each dimension [Fig. 3.2(a)-(b)], we see that the asymmetric modes (indices n and m dissimilar) have strikingly smaller quality factors than do the more symmetric modes (n and m nearly equal). This observation is consistent with expected trends for radiation loss of elastic waves through the membrane clamp. While we see consistently low Q's with highly asymmetric modes, we see some variability due to the membrane mounting structure, especially among the lowest order modes [38], as expected for a radiation loss mechanism. We note that, for the high-order symmetric modes that asymptote to Q's over a million, it becomes unclear whether radiation or material loss is the dominant effect.

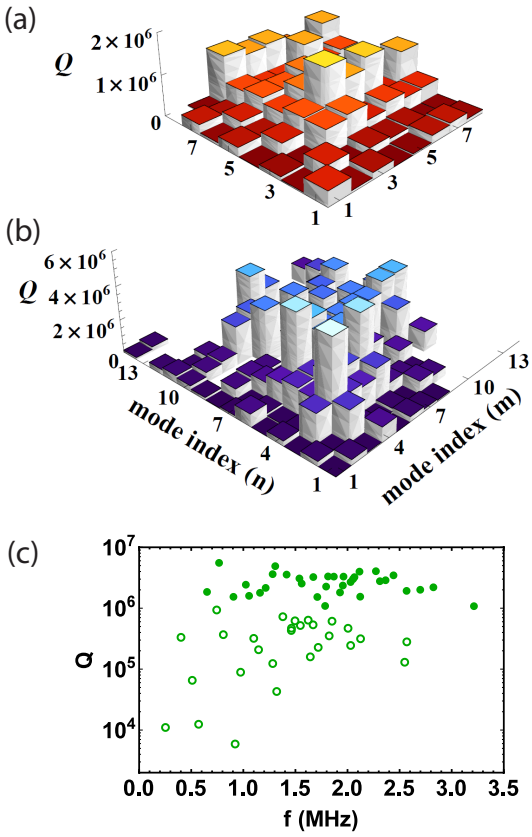

Figure 3.2: Radiation loss for a square membrane. Measurements of quality factors for many different modes of an (a) 0.5×0.5 mm and (b) 1×1 mm Si_3N_4 membrane. The symmetric modes generally have higher Q than asymmetric modes, as predicted by a radiation loss model [28].

3.4 Experimental Evidence II: Qs Depend on the Frequency of the Substrate Mode.

In this section, I describe an experimental observation of the hybridization between a membrane mode and a substrate mode. The experiment is similar to that in the last section, except here I measure the displacement spectrum driven by the piezo actuator. In a narrow frequency range, I identified a membrane mode (the sharp features) and a non-membrane mode (the bumps in the center) that are very close in frequency. I monitor them over a period of more than one week. The resonant frequency of the membrane is drifting toward

the non-membrane mode at a speed of -0.3 kHz/day. The drifting may be the result of a stress reduction due to stress relaxation in membrane or mounting epoxy, or difference in mass loading from surface contamination. I find that the Q of the membrane mode decreases monotonically as their frequency separation ($\Delta f = f_{\mathrm{mem}} - f_{\mathrm{sub}}$) is reduced. The Q decreases from a initial value of $\sim 3 \times 10^6$ to $< 4 \times 10^5$ when $\Delta f < 0.2$ kHz.

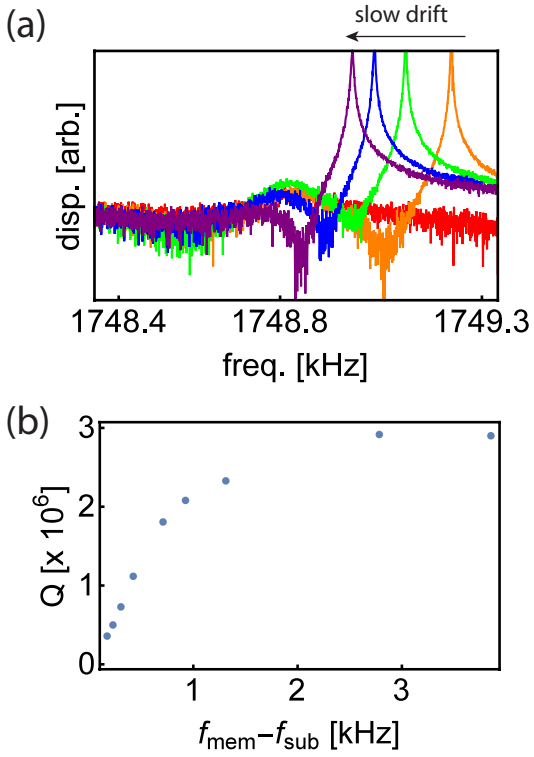

Figure 3.3: Hybridization of a membrane mode and a non-membrane mode. (a) A membrane mode (sharp features) drifts toward a non-membrane mode (bump features around 1748.8 kHz). (b) The membrane Q decreases monotonically as their frequency separation ($\Delta f = f_{\mathrm{mem}} - f_{\mathrm{sub}}$) is reduced.

3.5 FEM Simulation of the External Loss

In this section, I employ a finite-element-method (FEM) software COMSOL to simulate the whole membrane device in order to visualize the external loss. See Chapter 4.7 for simulation outline. I found many membrane modes and non-membrane modes of the device.

The membrane modes can be identified by the energy distribution: more than 99% of the energy is stored in the membrane. Even through there is little energy stored in the substrate, the energy distributions on the substrate show the interference patterns (see Fig. 3.4), as expected from the radiation loss.

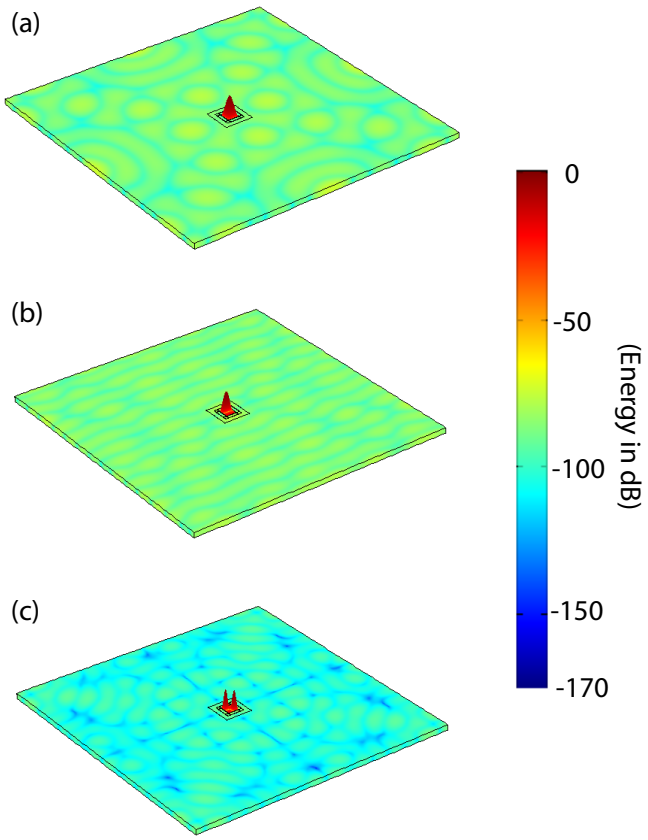

Figure 3.4: Simulated interference patterns. (a) (1,1) mode. (b) (1,2) mode with directional interference. (c) (2,2) mode with a higher-order interference. The energy stored in the membrane is higher than the other two modes, as indicated by the color of the energy distribution.

Chapter 4

A Phononic Bandgap Shield for High-Q Membrane Microresonators

Before the work described in this chapter, the external loss in the membrane devices in our group and others has been addressed mainly by varying the techniques for grasping the silicon frame [38, 39, 4]. Specifically, in our experiment we minimize the amount of epoxy and the contact area between the silicon frame and its holder. However more sophisticated techniques for control of acoustic waves have been extensively studied in the field of acoustic metamaterials. In particular, a phononic crystal (PnC) with acoustic bandgaps can be used to filter or confine acoustic waves [40, 41, 41, 42, 43, 44]. The use of PnC bandgaps to suppress the radiation loss of gigahertz, in-plane resonators has been demonstrated in the fields of microelectromechanical systems (MEMS) and optomechanics [45, 46].

This chapter describes our first attempt to implement the PnC technique to isolate our membrane. This work is originated from my experimental and theoretical work on the substrate engineering and Yeghishe Tsaturyan's work on the PnC simulation. We demonstrate a high-tension membrane inside of a silicon PnC structure that provides a shield for acoustic modes at megahertz frequencies. We probe the membrane modes and the non-membrane modes by measuring the displacement spectra of the membrane and different components of the support structure. We find that inside the observed bandgaps the density and the amplitude of the non-membrane modes are greatly suppressed. In addition, the membrane modes inside the observed bandgap are shielded from an external mechanical drive by up to 30 dB.

The Qs from these first attempt devices were not particularly high; $Q \sim 3 \times 10^6$ at a temperature of 5K. This is possibly because these membranes are limited by the material loss from defects generated in this new fabrication process. Nevertheless, based on the isolation provided by one device described in this chapter, we have demonstrated a wide-range Raman-Ratio thermometer over a wide temperature range. With continuing engineering, we have observed a Q of $(17 \pm 2) \times 10^6$ for the (2,2) mode of a 500 μm $\times$ 500 μm $\times$ 100 nm membrane in a dilution fridge with a base temperature of $\sim$ 500 mK. The device was fabricated in the NIST cleanroom.

4.1 Geometry of the PnC Devices

The device consists of a patterned silicon substrate with a center island that contains the high-tension square film of Si_3N_4 suspended across a mm-scale frame [Fig. 4.1(a)]. The fabricated membranes in the PnCs are experimentally confirmed to be under a high tensile stress of 1 GPa: The fundamental membrane frequency for devices A and B is 1.1 MHz. The unit cell length scale required to create a bandgap centered at a frequency f can be estimated by $\lambda/2 = v/2f \sim 1$ mm, where λ and v are the acoustic wavelength and velocity in silicon, respectively. For bandgaps centered at megahertz frequencies, we can fit 3 to 4 unit cells around the membrane with a 1 cm square chip. Our unit cell is composed of a square block with four bridges [Fig. 4.1(c)] [47, 48].

We study two different devices (A and B) with different PnC shields [Fig. 4.1(a)], and a reference device (C) without the PnC shield. (See Table 4.1 for measured geometry parameters.) In Figs. 4.3(a) and (b), we display the band diagrams for the two different PnCs with a infinite number of unit cells; this calculation is completed with the finite-element-method (FEM) software COMSOL using the measured device parameters.

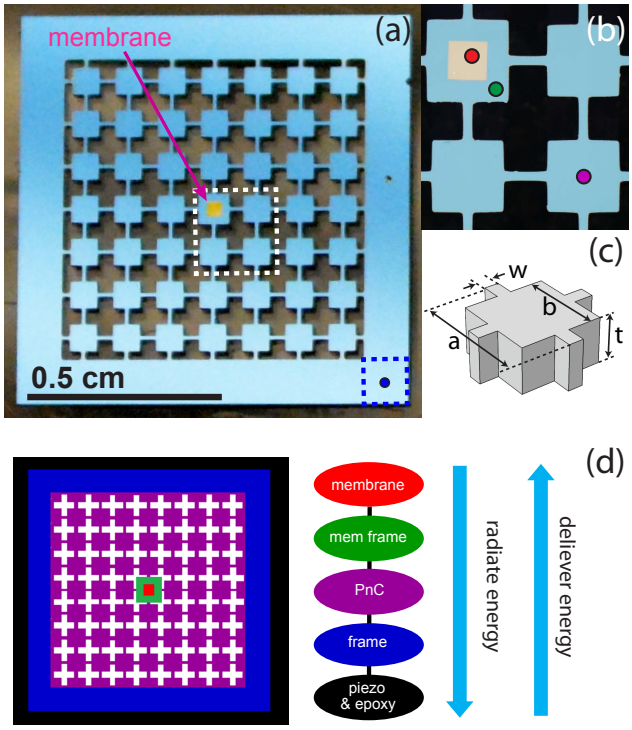

Figure 4.1: (a) Photograph of device A. The outermost chip frame (CF) is connected to the piezoelectric actuator at four corners (the blue dashed region). (b) Expanded view of the white-dashed regions shows a square membrane (M, yellow) surrounded by a membrane frame (MF, light blue) and a PnC unit cell (PnC, light blue). The red, green, and purple spots in (b) and the blue spot in (a) are locations of displacement measurements in Fig. 4.3 (c)-(f). (c) Schematic of the PnC unit cell and definitions of the geometry parameters. See Table 4.1 for the values of these parameters for the devices A and B.

4.2 Fabrication of the PnC Devices

This section outlines our first fabrication recipe developed by Katarina Cicak (Fig. 4.2). The fabrication was carried out by Kat and me. The process begins with the growth of a 100-nm-thick Si_3N_4 film by low-pressure chemical vapor deposition on both sides of a 300-μm thick Si wafer. The membrane and PnC structure are created in two sequential steps; each starts with the patterned removal of the back Si_3N_4 layer followed by deep reactive-ion etching (DRIE) for bulk Si machining. In the first step, the DRIE stops 10s of microns short of etching fully through the wafer, and a KOH wet etch completes the release of the

Table 4.1: Measured geometry parameters of the devices

Definition [μm]	symbol	Device A	Device B	Device C[a]
number of unit cells[b]		3	4.5	-
unit cell size	a	1100 μm	800 μm	-
block length	b	686	542	-
bridge width	w	97	96	-
wafer thickness	t	300	300	-
membrane length	l	372	367	500
membrane frame size		786	783	10^4
membrane thickness		0.1	0.1	0.04

[a] Norcada Inc.
[b] between the center and the edge of the chip

square Si_3N_4 membrane on the front of the wafer. In the second step, the PnC crosses are micromachined with DRIE all the way through the wafer (resulting in PnC holes that are vertical to $\sim 1^\circ$). During fabrication (except for the KOH step), the front side of the wafer is glued with processing adhesive to a protection substrate, and the final devices are released from the protection substrate and cleaned using solvents and a sulfuric-acid-based solution.

4.3 Isolation Profile: Externally Driven Mechanical Spectrum

To characterize the mechanical properties of the devices, we employ the reciprocity principle: delivering energy from the chip frame to the membrane is the reverse process of radiating energy from the membrane to the chip frame. Therefore the displacement spectrum of the membrane under an external drive is a measure of the isolation profile. We excite the chip at different frequencies through a piezoelectric ring actuator connected to all four frame corners with double-sided tape and measure displacement using a Mach-Zehnder interferometer. This interfermetry scheme allows us to easily probe displacement at different chip locations. In addition, compared with the detection system used in previous chapters, we improve the ground loops to reduce the noise floor and enhance displacement sensitivity.

First we present studies in which we probe the displacement of the Si_3N_4 membrane. We position the optical spot slightly off the membrane center to allow a variety of modes

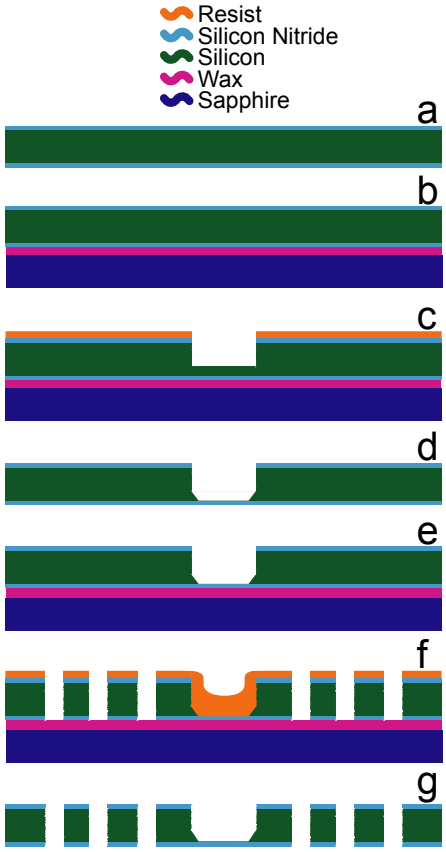

Figure 4.2: Fabrication process of the PnC-shielded membrane. (a) 100 nm of high-stress Si_3N_4 film is grown by LPCVD process on a 300-μm-thick Si wafer. (b) The sample wafer is attached to a mounting sapphire substrate with processing wax. (c) Membrane window is lithographically defined in a resist mask on the sample, followed first by a CF_4 + O_2 plasma etch to remove the top Si_3N_4, then by deep reactive ion etching (DRIE) into the Si wafer. The etch is stopped with tens of micrometers of Si left in the trench. (d) The sample wafer is separated from the mounting substrate by heating to reflow the wax and soaking in acetone. The remaining Si in the trench is removed by a KOH wet etch, finally releasing the Si_3N_4 membrane. (e) Next, the sample wafer is carefully attached to a mounting substrate again. (f) Phononic crystal pattern is lithographically defined in a resist mask on the sample, followed first by a CF_4 + O_2 plasma etch to remove the top Si_3N_4, then by a DRIE etch all the way through the Si wafer and bottom Si_3N_4 film forming cross-shaped phononic crystal holes. (g) Individual sample chips are separated from the sapphire substrate by soaking them in acetone. Chips are cleaned by a sequence of aggressive solvents and a sulfuric-acid-based solution to remove any processing debris.

to be probed. The driven displacements as a function of frequency for devices A and B are compared with that of a control device C in Fig. 4.3(c) and (d), respectively. We find that

the displacement is clearly suppressed in the frequency ranges of 1.5-2.75 MHz and 4.05-4.45 MHz (2.65-3.25 MHz and 3.5-4.5 MHz) for device A (B), resulting in a flat response that is limited by the shot noise of optical detection. These "observed bandgaps" roughly overlap with the calculated bandgaps [grey regions in both Fig. 4.3(a),(b) and (c),(d)]. The center frequencies of the observed and predicted bandgaps are consistent within ∼10%.

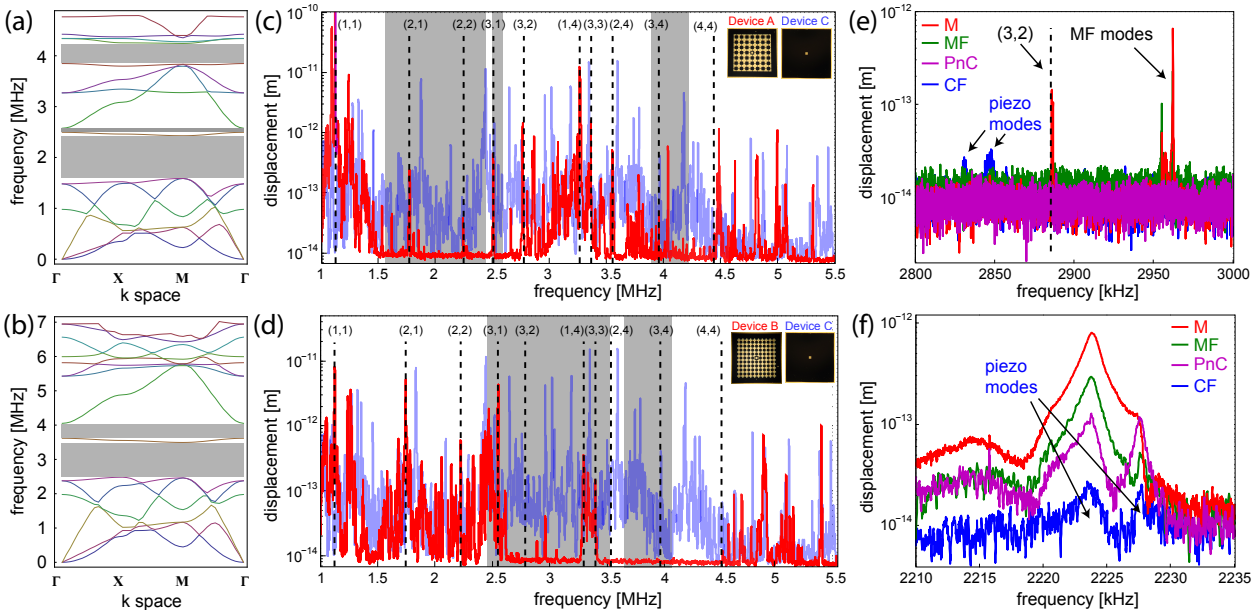

Figure 4.3: Frequency-dependent mechanical response. (a)-(b) Simulated band diagrams for infinite number of the unit cells used in devices A and B. Bandgap ranges are shown in grey. (c)-(d) Measured membrane displacement spectra of devices A, B, and C. The data are smoothed with a 4 kHz bandwidth. The ranges of ideal bandgaps are shown in grey. Membrane modes predicted based on the observed fundamental mode frequencies of devices A and B (up to the (4,4) mode) are shown by dashed lines. (e)-(f) Probing the non-membrane modes via measuring displacement spectra at different locations on device B: At the membrane (red), the membrane frame (MF, green), the PnC (purple), and the corner of chip frame (CF, blue). (e) An example spectral region in an observed bandgap in device B. (f) An example of two non-membrane modes of device B outside the observed bandgaps.

4.4 Probing the Non-Membrane Modes

Most of the modes we see in Fig. 4.3(c) and (d) are non-membrane modes; the finite number of membrane modes are shown by dashed lines. To further understand the spectrum,

we meassurent the displacement spectra of different locations on the device. Physically, the chip consists of (1) the membrane (M, red), (2) the membrane frame (MF, green), (3) the PnC structure (PnC, purple), and (4) the chip frame (CF, blue) [Fig. 4.1(d)]. The membrane and the MF together form a "defect" embedded in the PnC lattice. We optically probe the MF, the PnC, and the CF by focusing on the three different locations indicated in Fig. 4.1(b). Looking at these spectra in conjunction with the membrane displacement, we can understand the origin of the non-membrane modes. The piezoelectric actuator itself has a frequency-dependent structure, and measuring at the CF reveals information about this structure. Mainly the displacement measured on the corner of CF is limited by the detection noise, but some "piezo-modes" are clearly identifiable [see Fig. 4.3(e) and (f) for two examples].

We find that the combined spectra have distinct features inside and outside the observed bandgaps. Inside the observed bandgap, the spectra of the PnC, the MF, and the membrane are flat except a couple of "defect modes" observed in the spectra of the MF and the membrane [see Fig. 4.3(e) for one example]. While the mechanical modes of the MF cannot be completely avoided in the bandgap, they only occur sparsely and are clearly separable from the membrane modes. Outside the observed bandgaps, most modes, except for the membrane modes, have comparable motion in the membrane, the MF, and the PnC [see Fig. 4.3(f) for one example]. We also find that piezo modes greatly enhance the motion of other components. While inside the observed bandgaps, the piezo modes do not induce any of the observed motion of other components [compare Fig. 4.3(f) and (e)].

4.5 Simulation of the Membrane Modes and the Non-Membrane Modes

The observed eigenmodes include admixtures of modes created by the membrane, the MF, the PnC, and the CF. We use a FEM to simulate the whole device in order to visualize and characterize the expected frequency-dependent structure of all the modes. The boundary conditions for the simulation fix the corners of the back side of the chip. We find all the eigenmodes between 1 and 5 MHz. To estimate the motion that will be observed on the

Si_3N_4 membrane [as measured in Fig. 4.3(c) and (d)], for each mode we calculate a "partition coefficient" defined by the ratio of the energy stored in the membrane to the energy stored in the whole device:

$$\mathcal{E}_{\text{mem}} \equiv \frac{\int_{\text{mem}} \varrho(\mathbf{x})|\mathbf{u}(\mathbf{x})|^2 d^3x}{\int_{\text{whole}} \varrho(\mathbf{x})|\mathbf{u}(\mathbf{x})|^2 d^3x}, \tag{4.1}$$

where $\mathbf{u}(\mathbf{x})$ is the simulated displacement field and $\varrho(\mathbf{x})$ is the mass density field.

The partition coefficient $\mathcal{E}_{\text{mem}}$ is plotted in Fig. 4.4 as a function of mode frequency using the parameters for devices B and C. The membrane modes are clearly identifiable as the $\mathcal{E}_{\text{mem}} \simeq 0$ dB; these modes have the small effective mass associated with the Si_3N_4 membrane. A majority of the non-membrane modes of device C have an $\mathcal{E}_{\text{mem}}$ between -40 to -60 dB; these modes have a much larger effective mass associated with the silicon substrate. For device B, there are two ranges with reduced $\mathcal{E}_{\text{mem}}$ that roughly overlap with the ideal calculated bandgaps. The reductions are finite ($\mathcal{E}_{\text{mem}}$ between -70 to -130 dB) and smoothly degraded because the simulation takes into account the finite number of unit cells. There are also a finite number of non-membrane modes with $\mathcal{E}_{\text{mem}} > -40$ dB. Inside the device-B bandgap, these modes can be classified as defect modes with $\mathcal{E}_{\text{mem}} < -30$ dB. Outside of the device-B bandgap and in device C, there is a larger number of modes ($\sim 4\%$ of the modes) with $\mathcal{E}_{\text{mem}} > -40$ dB. These modes with the largest $\mathcal{E}_{\text{mem}}$ tend to be clustered near the expected membrane mode frequencies.

In Fig. 4.4(b)-(f) we also show the displacement profile of example modes on a logarithmic scale. We see that the non-membrane modes inside the bandgaps are dominated by the MF or the CF, and the displacement field decays exponentially in the PnC [Fig. 4.4(c),(d)]. On the contrary, the non-membrane modes outside the bandgaps have a uniformly distributed displacement field [Fig. 4.4(b)]. We also find that for the membrane modes inside and outside the bandgaps [Fig. 4.4(e) and (f)], the displacement fields in the PnC behave the same as the non-membrane modes inside and outside the bandgaps. In other words, inside the bandgap, the PnC acts as a passive mechanical filter that decouples the CF and

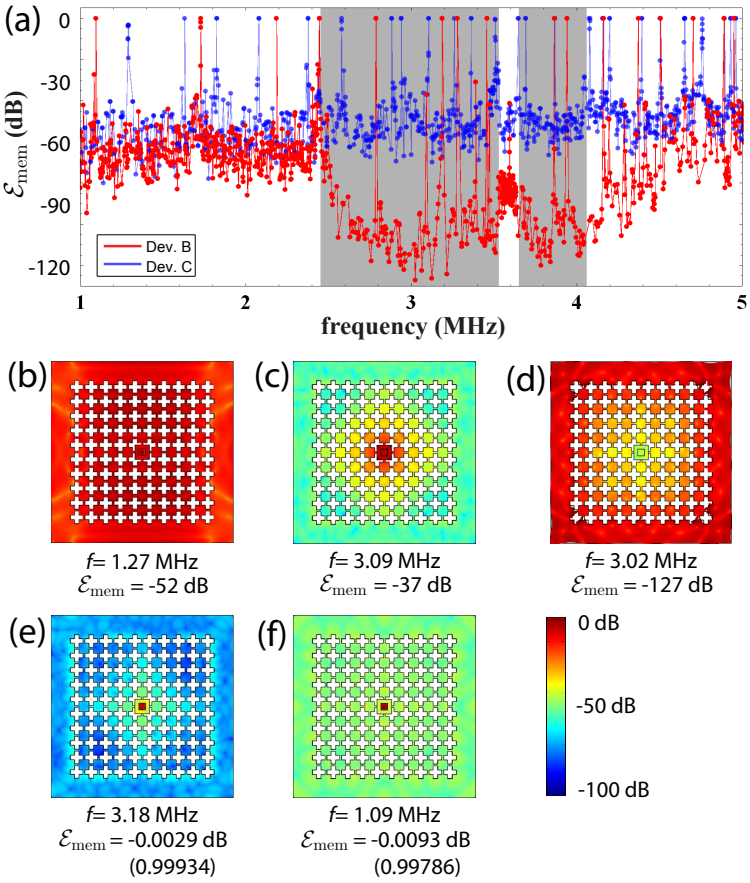

Figure 4.4: Simulated membrane and non-membrane modes for devices B and C. (a) Simulated partition coefficient $\mathcal{E}_{\mathrm{mem}}$ of devices B and C. Data of device B (C) are red (blue). Data of each device are connected by lines to see the trend. Ideal calculated bandgaps are shown in grey. (b)-(f) Simulated displacement field for four kinds of modes. Color scheme represents the amplitude of displacement in a logarithmic scale. (b) An example of a non-membrane mode outside the bandgap. (c) An example of a MF mode inside the bandgap. (d) An example of a CF mode inside the bandgap. (e)-(f) Two examples of membrane modes inside/outside the bandgap.

the "defect"; outside the bandgap, the PnC moves with all the other components together, i.e., they can be strongly coupled.

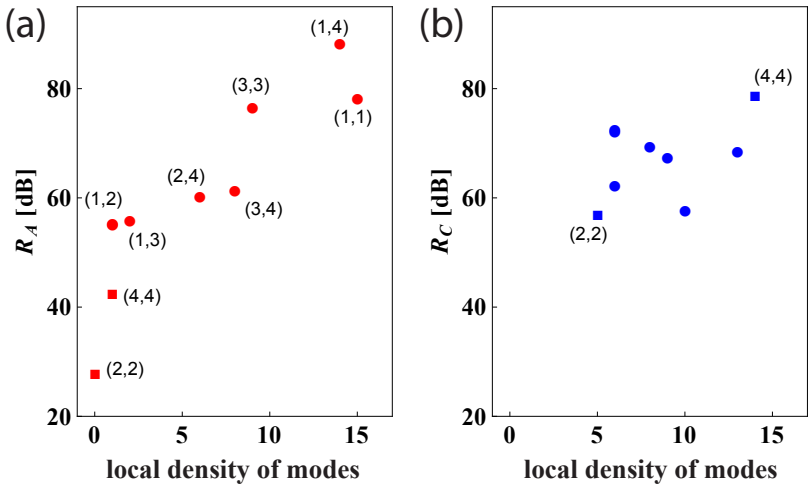

Figure 4.5: The ratio of the actuated energy of the membrane modes provided by the piezoelectric actuator to that by the thermal fluctuating force as a function of a local density of modes. The density is determined from the data in Fig. 4.1(c) by counting the number of observed modes in a 50 kHz range centered at each membrane mode. (a) Data for device A. The membrane mode indices are labeled. (b) Data for device C. The corresponding modes with lowest R in (a) are shown with square symbols.

4.6 Loss Factor Ratio

In the previous sections we have discussed the mechanical properties of the devices over a large frequency range and gained understanding of the non-membrane modes. In this section we focus on the narrow spectra near the membrane modes. We quantitatively analyze the isolation of the membrane modes by recording the piezo actuated energy of the (1,1) through (4,4) membrane modes of devices A and C. To obtain a calibrated measure of the relative actuated energy, we also measure the thermal fluctuating energy for each mode, which is not shielded by the PnC. We define the ratio of the driven to thermal energies:

$$R = R(p, f, B_w) \propto \frac{|\mathcal{D}(p, f)/\eta|^2}{[\mathcal{S}_d(f)/\eta^2]B_w} = \frac{|\mathcal{D}(p, f)|^2}{\mathcal{S}_d(f)B_w}, \tag{4.2}$$

where $\mathcal{D}(p, f)$ is the driven displacement amplitude measured with a network analyzer under external driving power p, $\mathcal{S}_d(f)$ is the displacement spectral density measured with a spectrum analyzer without external driving power, η is the overlap factor between the optical spot and the membrane mode shape, and B_w=2 Hz is the resolution bandwidth of the spectrum analyzer. The lower the R, the higher the mode is isolated.

Another useful measure is the local mode density near each membrane mode. The piezoelectric actuator does not directly drive the membrane; it drives the membrane through the chip frame, the PnC, and the membrane frame. In other words, the piezoelectric actuator actuates the membrane mode through the non-membrane modes. This measure provides an estimate of the expected driving efficiency, but not necessarily a rigorous correspondence, because the set of optically measured modes will not necessarily correspond to the set of modes that couples best to a particular membrane mode.

In Fig. 4.5 we plot R as a function of the local mode density near each membrane mode. We see a positive correlation between the driven motion and this mode density for device A. We also observe a much larger dynamic range in R for device A than for device C, which is as expected because the phononic crystal structure introduces a nonuniformity to the local mode structure. A direct comparison between devices A and C shows the smallest R in device A is 30 dB smaller than the smallest R in device C, indicating that in the bandgap membrane modes can be significantly isolated from the chip frame.

4.7 FEM Simulation

In this section, I outline the simulations of the band diagrams and the mechanical modes of our devices with COMSOL. The first task is to simulate the eigenmodes of an infinite crystal, while the second task is to simulate the eigenmodes of the physical devices. The intial studies of these simulations were carried out by Yegeishe Tsaturyan [49].

To simulate the band diagram of the infinite crystal, we implement a unit cell with a *Periodic Condition*. We select the boundary and set the *periodicity* to *Floquet periodicity*.

We need to specify a k-vector that defines the phase difference between the adjcent unit cells in the infinite crystal. To generate the band diagram, we have to calculate the eigenmodes of the crystal with the representative k-wave vectors. We simulate the eigenmodes with a *parametric sweep* to vary the k-vector along the boundary of the first Brillouin zone. Then the eigenfrequecies as a function of these k-wave vectors are plotted as the band diagram. Note that the meshes on the peridoc boundaries have to be matched.

To simulate the mechanical modes of the physical devices, we include the membrane, the silicon frame, and even the epoxy. The simulation of the mechanical modes is straightfoward, but extra care is needed to mesh to the objects. The default tetrahedral mesh will take us infinite amount of time to complete the simulation. The reason is that the size of tetrahedral mesh is defined by the smallest dimension of our device - the membrane thickness. Hence we use a *swept* technique for the membrane, and define the smallest dimension with the *distribution setting*.

Chapter 5

Ponderomotive Squeezing with a Membrane Mechanical Resonator

In this chapter, I discuss the physics of ponderomotive squeezing and our experimental results. The experiment is a natural extension of the RPSN work described in Ref. [5]. For this experiment, I built the balanced homodyne detection, contributed to data taking and analysis, and helped with the manuscript. Later on I developed the conceptual and theoretical framework discussed in Sec. 5.3. A number of the figures and some of the text are taken directly from Ref. [6] written in conjunction with Thomas Purdy, Robert Peterson, and Nir Kampel.

5.1 Introduction to Ponderomotive Squeezing

Coherent light is a ubiquitous tool for metrology. However, as dictated by quantum mechanics, any measurement of the properties of the coherent state will be limited by quantum noise. Quantum noise, unlike classical noise, cannot be eliminated by any technical trick (Fig. 5.1). However, it is possible to generate light with less noise in a selected quadrature than the noise of a coherent state. Such light is called squeezed light.

The history of squeezed light is intimately linked to quantum limited displacement sensing [50], owing to proposals to increase the displacement sensitivity of large scale gravitational wave observatories with squeezed light [51, 52, 53, 54]. Squeezed light was first produced using atomic sodium as a nonlinear medium [55], and was soon followed with experiments employing optical fibers [56] and nonlinear crystals [57]. Substantial squeezing

has been achieved in modern experiments (up to 12.7 dB [58]), and using squeezing has allowed a enhanced sensitivity in gravitational wave detectors [59] and in biological measurements [60]. Squeezed microwave fields, which have now been demonstrated with up to 10 dB of noise suppression [61], are an important tool in quantum information processing with superconducting circuits.

Early on, searches for ever-better squeezing materials led to suggestions that an optomechanical cavity, in which radiation pressure changes the cavity length proportional to optical intensity, could act as a low-noise Kerr nonlinear medium [62, 63, 64], and hence could be a useful source of squeezed light [65]. This optomechanical method of manipulating the quantum fluctuations has historically been termed ponderomotive [66] squeezing. A unique advantage of utilizing optomechanical nonlinearity is that correlations induced by a mechanical object can be used to enhance displacement sensitivity for that same object [54, 67].

However, experimentally it has proven difficult to realize the substantial interplay between mechanical motion and quantum fluctuations of light required for ponderomotive squeezing. Early on, radiation pressure induced optical non-linearity (bistability) was experimentally demonstrated in a cavity with a pendulum-suspended end mirror [68]. Recently, novel optomechanical systems have been developed to manipulate mechanical motion with radiation pressure. Ponderomotively squeezed light at the few percent level has been demonstrated using a mechanical mode of an ultracold atomic gas inside an optical cavity [69], and very recently using a silicon micromechanical resonator [70]. The former experiment was limited by nonlinearities in this interaction and the latter by excess mechanical thermal motion. In our experiment, we observe ponderomotive squeezing at 1.7±0.2 dB below (32% below) the shot noise level and optical amplification of quantum fluctuations by over 25 dB. The squeezing is realized on light transmitted through a Fabry-Perot optical cavity with an embedded, mechanically-compliant, dielectric membrane. The squeezing attained here is dramatically larger, and the spectrum contains considerably less technical noise in the data than previous studies.

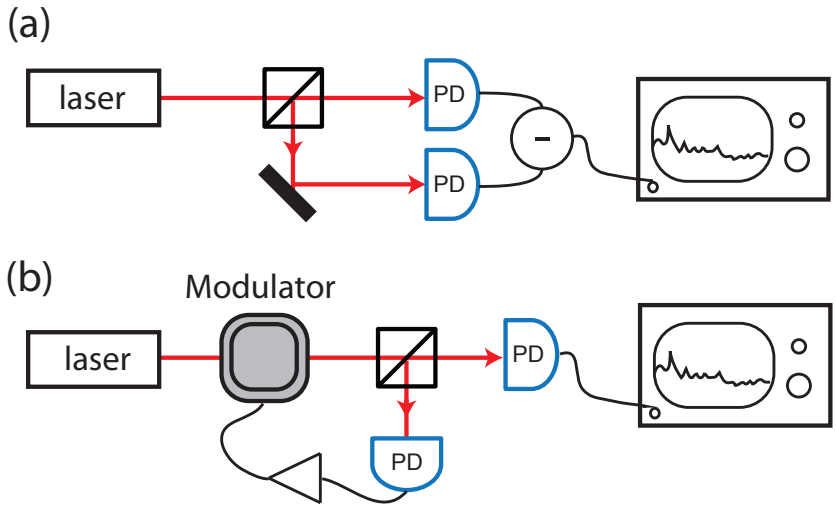

Figure 5.1: The shot noise cannot be eliminated by any technical trick (see Ref. [71] and appendix C) (a) An attempt to kill quantum noise by difference detection. The laser beam is divided into two beams with equal power and detected by two photodetectors. The two detectors will simultaneously sense any technical noise of the laser. Using a difference amplifier, the common technical noise will be subtracted. However, the scheme fails to kill quantum noise. (b) Another attempt to kill quantum noise by feedback control. An intensity modulator and two photodetectors are used. A fraction of laser beam is directed to the detector B. The detected signal is feedback to the intensity modulator. This technique fails to kill quantum noise in detector A.

5.2 Quantum Descriptions of Light

In this section we develop the necessary language to describe quantum properties of squeezed light.

5.2.1 Quadrature Amplitudes

In this subsection, we first define the quadrature amplitudes and phasor diagram in classical optics. Then we show their quantum version.

Light, an electromagnetic wave, can be described by

$$E(r,t) = E_0[\alpha(r,t)e^{i\omega t} + \alpha^*(r,t)e^{-i\omega t}]p(r,t), \tag{5.1}$$

where E_0 is the electrical field amplitude and $p(r,t)$ is the polarization vector. The dimen-

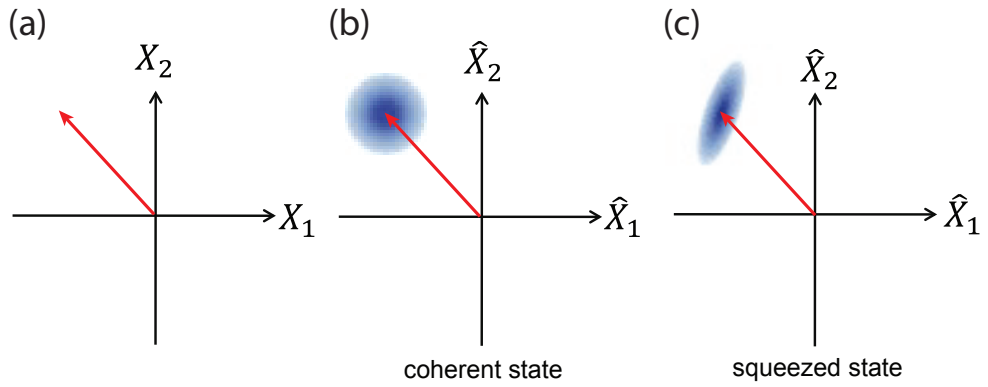

Figure 5.2: Phasor representation of light. (a) Noiseless classical light. (b) A coherent state. (c) A squeezed state.

sionless complex amplitude $\alpha(r,t)$ of the wave can be written as a magnitude $\alpha_0(r,t)$ and a phase $\phi(r,t)$.

$$\alpha(r,t) = \alpha_0(r,t)e^{i\phi(r,t)} \tag{5.2}$$

As a complex number, we can also represent $\alpha(r,t)$ in a complex plane (Fig. 5.2(a)). In optics, this geometrical representation is called the phasor diagram. The x-axis (real part) is called the amplitude quadrature, and the y-axis (imaginary part) is called the phase quadrature:

$$X_1(r,t) = 2\mathrm{Re}[\alpha(\mathrm{r,t})] = \alpha(r,t) + \alpha^*(r,t) = 2\alpha_0(r,t)\cos[\phi(r,t)] \tag{5.3}$$

$$X_2(r,t) = 2\mathrm{Im}[\alpha(\mathrm{r,t})] = i[\alpha(r,t) - \alpha^*(r,t)] = 2\alpha_0(r,t)\sin[\phi(r,t)] \tag{5.4}$$

We can also define an arbitrary quadrature by

$$X_\theta(r,t) = X_1(r,t)\cos(\theta) + X_2(r,t)\sin(\theta) \tag{5.5}$$

In addition, the fluctuations or modulations in both amplitude and phase can be represented as fluctuations in the quadrature values:

$$\alpha(t) = \alpha + \delta X_1(t) + i\delta X_2(t) \tag{5.6}$$

In the quantum mechanical model of light, the complex amplitude α is quantized to be $\hat{a}$,

hence the quadrature amplitudes are quantized to be:

$$\hat{X_1} = \hat{a} + \hat{a}^\dagger \tag{5.7}$$

$$\hat{X_2} = i(\hat{a}^\dagger - \hat{a}) \tag{5.8}$$

$$\hat{X_\theta} = \hat{X_1}\cos(\theta) + \hat{X_2}\sin(\theta) \tag{5.9}$$

$$= \hat{a}e^{-i\theta} + \hat{a}^\dagger e^{i\theta} \tag{5.10}$$

Now the quantum mechanics comes into play. As a result of non-zero commutation relation between $\hat{X_1}$ and $\hat{X_2}$, the variances of the operators in any state have to obey

$$\langle|\Delta\hat{X_1}|^2\rangle\langle|\Delta\hat{X_2}|^2\rangle \geq 1 \tag{5.11}$$

$$\langle|\Delta\hat{X_\theta}|^2\rangle\langle|\Delta\hat{X}_{\theta+\pi/2}|^2\rangle \geq 1. \tag{5.12}$$

Therefore, we will always have quantum noise in all quadratures. Note that we use a convention that the minimum product is 1. Some references use 1/4.

5.2.2 Coherent States and Squeezed States

The coherent state is a minimum uncertainty state and

$$\langle|\Delta\hat{X_1}|^2\rangle = \langle|\Delta\hat{X_2}|^2\rangle = \langle|\Delta\hat{X_\theta}|^2\rangle = 1. \tag{5.13}$$

The limit imposed by quantum noise affects all the quadratures of a coherent state evenly. In other words, at all quadratures the light is shot noise limited. Since the coherent state is a Gaussian state, we can present it in the phasor diagram as an area centered around its expectation value $(\langle\hat{X_1}\rangle, \langle\hat{X_2}\rangle)$. The area describes the uncertainty distribution and has a diameter of 1 (Fig. 5.2(b)).

On the other hand, the noise of a squeezed state is less than the shot noise in a selective quadrature $\langle|\Delta\hat{X_\phi}|^2\rangle < 1$. As dictated by uncertainty principle, the noise is "squeezed" into the orthogonal quadrature $\langle|\Delta\hat{X}_{\phi+\pi/2}|^2\rangle > 1$. In the phasor diagram, its uncertainty area is an ellipse with major radius $\langle|\Delta\hat{X}_{\phi+\pi/2}|^2\rangle$ and minor radius $\langle|\Delta\hat{X_\phi}|^2\rangle$ (Fig. 5.2(c)).

5.3 Squeeze Light by Correlating Two Quadratures

To generate a squeezed state out of a normal coherent state, a key is to correlate two quadratures. One way to generate such a correlation is to pass a light beam through a nonlinear medium such as a Kerr medium. A Kerr medium has an intensity-dependent refractive index. The amplitude fluctuation will modulate the refractive index, which, in turn, will modulate the phase of the transmitted light. Therefore, it generates correlation between the amplitude quadrature and the phase quadrature.

An optomechanical system can be thought of as an effective Kerr medium, and hence ponderomotive squeezing can be understood using many of the same ideas as typical nonlinear media. To understand this, consider a light bouncing off a flexible mirror. Light carries radiation pressure that is proportional to its amplitude. The radiation pressure produced by the amplitude fluctuation drives the flexible mirror. As the mirror moves, the phase of the reflected light is modulated. This creates the correlation between the amplitude quadrature and the phase quadrature.

In the following subsection, we describe the mathematical models for a regular Kerr medium [72] and an optomechanical system. We point out their features and compare their differences.

5.3.1 Kerr Medium

Consider a beam traveling through a medium with an intensity-dependent refractive index. The input beam and output beam can be described by Eq. 5.6. Specifically, $\alpha^{\text{in}}(t) = \alpha^{\text{in}} + \delta X_1^{\text{in}}(t) + i\delta X_2^{\text{in}}(t)$ and $\alpha^{\text{out}}(t) = \alpha^{\text{out}} + \delta X_1^{\text{out}} + i\delta X_2^{\text{out}}$. The nonlinear refractive index can be described by $n(\alpha) = n_0(1 + n_2\alpha^2)$, where n_0 is its linear refractive index and n_2 is the second-order nonlinear refractive index. The modulated output phase can be expressed as:

$$\phi_{\text{out}} = \phi_{\text{in}} + \frac{2\pi n L}{\lambda} = \frac{2\pi L}{\lambda}\left\{n_0 + n_2(\alpha_{\text{in}}(t) + \delta X_1^{\text{in}}(t))^2\right\}, \tag{5.14}$$

where L is the length of the medium. On the other hand, the amplitude of the light does not change.

$$\alpha^{\text{out}} = \alpha^{\text{in}} = \alpha \tag{5.15}$$

We can write the changes in terms of the quadrature amplitudes:

$$\delta X_1^{\text{out}} = \delta X_1^{\text{in}} \tag{5.16}$$

$$\delta X_2^{\text{out}} = \delta X_2^{\text{in}} + \frac{4\pi n_0 n_2 L}{\lambda}\alpha^2 \delta X_1^{\text{in}}(t) \equiv \delta X_2^{\text{in}} + 2r_{\text{Kerr}}\delta X_1^{\text{in}}(t) \tag{5.17}$$

where r_{Kerr} is a parameter describe the degree of correlation. It includes the nonlinearity and the amplitude of the input field.

When the input beam is a coherent state, the variance of the output quadrature, $\langle|\Delta\hat{X}_\theta{}^2|\rangle = \langle|\delta\hat{X}_1^{\text{out}}\cos(\theta) + \delta\hat{X}_2^{\text{out}}\sin(\theta)|^2\rangle$, is given by

$$V(\theta) = \langle|\Delta\hat{X}_\theta{}^2|\rangle = 1 + 2r_{\text{Kerr}}\sin(2\theta) + 4r_{\text{Kerr}}^2\sin^2(\theta). \tag{5.18}$$

The squeezing is achieved when $V(\theta) < 1$. The optimal squeezing and quadrature angle are given by

$$V(\theta_s) = 1 - 2r_{\text{Kerr}}\sqrt{1 + r_{\text{Kerr}}^2} + 2r_{\text{Kerr}}^2 \tag{5.19}$$

$$\theta_s = -\frac{1}{2}\arctan\left[\frac{1}{r_{\text{Kerr}}}\right] \tag{5.20}$$

The level of squeezing increases steadily with the Kerr coefficient [Fig. 5.3(b)]. The optimal angle asymptotically approaches the value 0, the amplitude quadrature [Fig. 5.3(a)]. But note that the variance of amplitude quadrature, $V(\theta = 0)$, is always equal to the shot noise limit. This feature is independent of the nonlinearity and is the signature of the Kerr squeezing.

5.3.2 Optomechanical Kerr Effect

While the full calculation of squeezed light had been studied in our group [6], I wanted to gain a more complete understanding of the parallels betweens our devices and typical

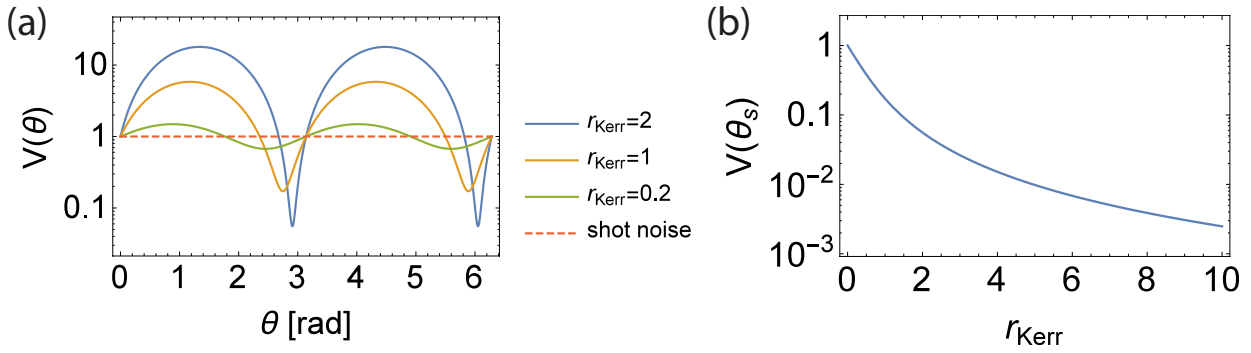

Figure 5.3: (a) The variance as a function of quadrature angle for three different Kerr coefficient values. (b) The minimum variance as a function of the Kerr coefficient.

Kerr media. To investigate this, I formulate the optomechanical interaction into a Kerr-like interaction. I consider the canonical cavity optomechanical system where the mechanical oscillator is a mirror of a one-sided cavity. The cavity enhances the amplitude of the light and the phase shift. The interaction Hamiltonian is $\hbar g N z$, where z is the operator of the effective mechanical coordinate and N is the intracavity photon number operator [64, 63].

5.3.2.1 The Complex Kerr Coefficient

Here, for simplicity, the input light is the shot noise entering the cavity, and the output light is the modulated light inside the cavity. We start with the equation of motion for intracavity light fluctuations in the frequency domain [4]:

$$\hat{d}(\omega) = \chi_c(\omega)\left(-ig\bar{a}\hat{x}(\omega) + \sqrt{\kappa}\hat{\xi}_{in}(\omega)\right) \equiv -ig\bar{a}\chi_c(\omega)\hat{x}(\omega) + \mu(\omega) \tag{5.21}$$

where $\mu(\omega)$ is the input shot noise operator in the cavity:

$$\mu(\omega) \equiv \chi_c(\omega)\sqrt{\kappa}\hat{\xi}_{in}(\omega) \tag{5.22}$$

The intracavity light consists of the phase fluctuation due to the position fluctuation of the mechanical oscillator and the shot noise. The mechanical oscillator is driven by the radiation

pressure of the intracavity shot noise and the thermal fluctuating force:

$$\begin{aligned}\hat{x}(\omega) &= -\frac{2\omega_m}{\mathbb{N}(\omega)} g\bar{a}(\hat{\mu}^\dagger + \hat{\mu}) + \frac{\sqrt{\Gamma}}{\mathbb{N}(\omega)}\tilde{\eta}_+(\omega) \\ &= -ig\bar{a}\chi_m^{\text{eff}}(\omega)(\hat{\mu}^\dagger + \hat{\mu}) + \frac{i\sqrt{\Gamma}}{2\omega_m}\chi_m^{\text{eff}}(\omega)\tilde{\eta}_+(\omega) \end{aligned} \tag{5.23}$$

where

$$\tilde{\eta}_+ = \frac{\hat{\eta}^\dagger(\omega)}{\chi_m(\omega)} + \frac{\hat{\eta}(\omega)}{\chi_m^*(-\omega)} \tag{5.24}$$

$$\mathbb{N}(\omega) = \mathbb{N}_0(\omega) + 2\omega_m \left(g\bar{a}\right)^2 \pi_-(\omega) = i\frac{2\omega_m}{\chi_m^{\text{eff}}(\omega)} \tag{5.25}$$

Now I substitute Eq. 5.23 into Eq. 5.21 and define the input and output operators of the amplitude and phase quadratures to be

$$\hat{u}_+^{\text{in}} = \hat{\mu}^\dagger + \hat{\mu} \;\&\; \hat{u}_-^{\text{in}} = -i\left(\hat{\mu}^\dagger - \hat{\mu}\right) \tag{5.26}$$

$$\hat{u}_+^{\text{out}} = \hat{d}^\dagger + \hat{d} \;\&\; \hat{u}_-^{\text{out}} = -i\left(\hat{d}^\dagger - \hat{d}\right) \tag{5.27}$$

We arrive at

$$\hat{u}_+^{\text{out}} = \left(1 - i(g\bar{a})^2\pi_-(\omega)\chi_m^{\text{eff}}(\omega)\right)\hat{u}_+^{\text{in}} + ig\bar{a}\frac{\sqrt{\Gamma}}{2\omega_m}\pi_-(\omega)\chi_m^{\text{eff}}(\omega)\tilde{\eta}_+(\omega) \tag{5.28}$$

$$\hat{u}_-^{\text{out}} = \hat{u}_-^{\text{in}} - i(g\bar{a})^2\pi_+(\omega)\chi_m^{\text{eff}}(\omega)\hat{u}_+^{\text{in}} + ig\bar{a}\frac{\sqrt{\Gamma}}{2\omega_m}\pi_+(\omega)\chi_m^{\text{eff}}(\omega)\tilde{\eta}_+(\omega) \tag{5.29}$$

where we define

$$\pi_+(\omega) \equiv \chi_c^*(-\omega) + \chi_c(\omega) = 2\frac{\frac{\kappa}{2} - i\omega}{\left(\frac{\kappa}{2} - i\omega\right)^2 + \Delta^2} \tag{5.30}$$

$$\pi_-(\omega) \equiv i\left[\chi_c^*(-\omega) - \chi_c(\omega)\right] = \frac{2\Delta}{\left(\frac{\kappa}{2} - i\omega\right)^2 + \Delta^2} \tag{5.31}$$

In the limit of negligible thermal noise and zero detuning, the equations are simply

$$\hat{u}_+^{\text{out}} = \hat{u}_+^{\text{in}}(\omega) \tag{5.32}$$

$$\hat{u}_-^{\text{out}} = \hat{u}_-^{\text{in}}(\omega) + \tilde{r}(\omega)\hat{u}_+^{\text{in}}(\omega) \tag{5.33}$$

where I define

$$\tilde{r}(\omega) = -i(g\bar{a})^2 \pi_+(\omega) \chi_m^{\text{eff}}(\omega) \tag{5.34}$$

Therefore, the cavity optomechanical system is equivalent to a Kerr medium with a complex Kerr coefficient $\tilde{r}(\omega)$. Not surprisingly, the Kerr coefficient is proportional to the optomechanical coupling strength and weighted by the mechanical and cavity response. The magnitude of $\tilde{r}(\omega)$ is peaked at the mechanical resonance $\omega = \omega_m$ and can be expressed as

$$|\tilde{r}(\omega)|^2 = (g\bar{a})^4 \frac{4}{(\kappa/2)^2 + \omega_m^2} \frac{1}{(\Gamma/2)^2} = 4C^2(1 + (2\omega_m/\kappa)^2)^{-1}, \tag{5.35}$$

where $C = 4(g\bar{a})^2/\kappa\Gamma = 4\bar{N}g^2/\kappa\Gamma$ is the optomechanical cooperativity, and $\bar{N} = \bar{a}^2$ is the average intracavity photon occupation. That is, the magnitude of the complex Kerr coefficient is about equal to the optomechanical cooperativity in the unresolved sideband regime. In other words, a small cavity and mechanical linewidth are desired for large nonlinearity. We note that the cavity linewidth cannot be too small compared to the mechanical frequency. The resolved sideband factor $(1 + (2\omega_m/\kappa)^2)^{-1}$ is in the equation because the quantum fluctuation at the mechanical frequency need to be large inside the cavity.

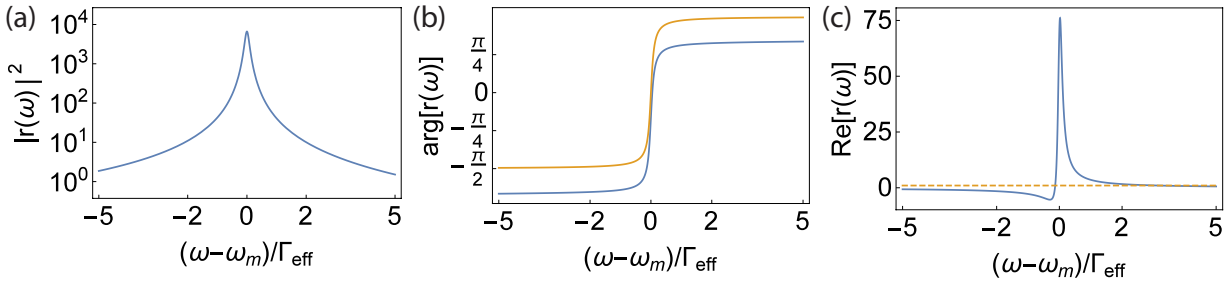

Figure 5.4: Frequency dependence of the optomechanical Kerr coefficient $\tilde{r}(\omega) = r(\omega)e^{i\phi_r(\omega)}$. (a) The magnitude square $|r(\omega)|^2$ follows the mechanical response function $|\chi(\omega)|^2$. The bandwidth of nonlinearity is the mechanical bandwidth. (b) The phase provided by $\tilde{r}(\omega)$. The Orange line is the phase response provided by $\chi_m^{\text{eff}}(\omega)$. (c) The real part of the complex Kerr coefficient. $\text{Re}[\tilde{r}(\omega)] = |\tilde{r}(\omega)| \cos[\phi_r(\omega)]$. It has a fano-shape.

The variance of the output quadrature, $\langle|\hat{u}_\theta|^2\rangle = \langle|\hat{u}_+^{\text{out}} \sin(\theta) + \hat{u}_-^{\text{out}} \cos(\theta)|^2\rangle$, is given

by

$$S_\theta(\omega) = 1 + \mathrm{Re}[\tilde{\mathrm{r}}(\omega)]\sin(2\theta) + |\tilde{\mathrm{r}}(\omega)|^2\sin^2(\theta) \tag{5.36}$$

$$= 1 + \mathrm{Re}[\tilde{\mathrm{r}}(\omega)]\sin(2\theta) + \mathrm{Re}[\tilde{\mathrm{r}}(\omega)]^2\sin^2(\theta) + \mathrm{Im}[\tilde{\mathrm{r}}(\omega)]^2\sin^2(\theta) \tag{5.37}$$

Compared with Eq. 5.18, we see that the they are basically the same except the extra term $\mathrm{Im}[\tilde{\mathrm{r}}(\omega)]^2\sin^2(\theta)$, which comes from the imaginary Kerr coefficient. This term reduces the amount of squeezing and enhances the amount of anti-squeezing.

I can draw a number of conclusions based on the frequency dependence of $\mathrm{Re}[\tilde{\mathrm{r}}(\omega)]$ (Fig. 5.4). First, $\mathrm{Re}[\tilde{\mathrm{r}}(\omega)]$ is concentrated around the mechanical frequency with a frequency range characterized by the effective mechanical linewidth. Second, $\mathrm{Re}[\tilde{\mathrm{r}}(\omega)]$ has a fano-shape. Hence, the squeezing spectrum will be a fano-shape, as well. Third, $\mathrm{Re}[\tilde{\mathrm{r}}(\omega)]$ is negative below resonance and positive above the mechanical frequency. That means the squeezed angle is below 0 when the frequency is below the mechanical resonance and above zero when the frequency is above the resonance. In other words, if we look at negative quadrature angles, the squeezing will happen above the resonance; if we look at positive quadrature angles, the squeezing will happen below the resonance (See Fig. 5.5). Fourth, $\mathrm{Re}[\tilde{\mathrm{r}}(\omega)]$ vanishes as $\omega \to \infty$ but remain finite at $\omega = 0$. With the experimental parameters described in the later section, we have $\mathrm{Re}[\tilde{\mathrm{r}}(0)] \sim 0.2$ and $\mathrm{Re}[\tilde{\mathrm{r}}(\omega)] \sim 0$. Hence, in principle, the mechanism allows squeezing at DC [65].

5.4 Experimental Requirements for Observing Ponderomotive Squeezing

To observe ponderomotive squeezing, like other-types of squeezing experiments, we need a large nonlinearity and a detection system with a good quantum efficiency. Any optical loss in the detection will attenuate the squeezing. A large nonlinearity requires a large optomechanical cooperativity, specifically, large optomechanical coupling, small mechanical dissipation, and small optical linewidth. The necessary size of nonlinearity is determined by the size of the mechanical thermal noise.

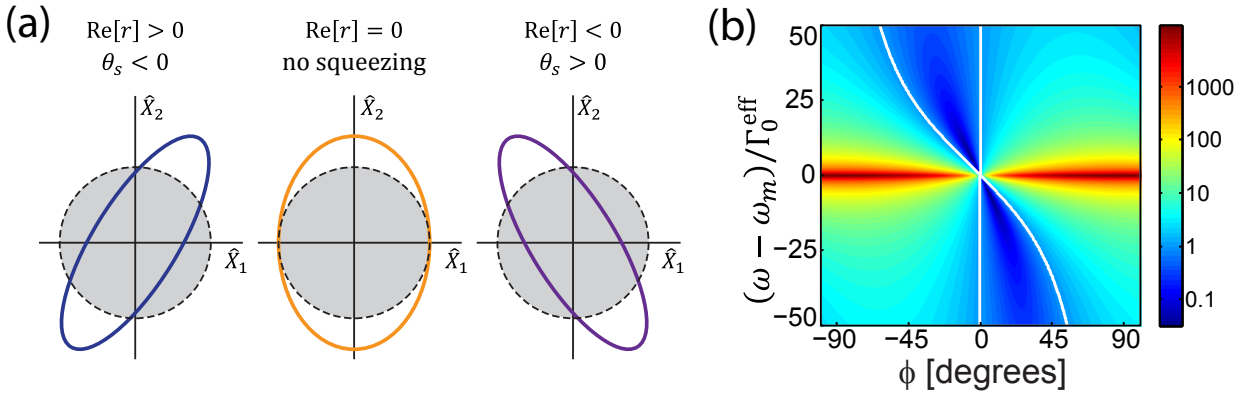

Figure 5.5: Phasor diagrams of the signal beam for real parts of $\tilde{r}$, the complex Kerr parameter. The dashed circle represents the variance of the Gaussian noise distribution of the vacuum state. Distributions inside the dashed circle represent squeezed states. (d) Calculated signal-beam quadrature spectrum from Heisenberg-Langevin equations. We set $\Delta - 0$ in the idealized case of zero temperature and no optical loss . Otherwise, parameters are set to experimental values: $\kappa/2\pi = 1.7$ MHz, $\Gamma_0^{\rm eff}/2\pi = 2.6$ MHz, $\omega_m/2\pi = 1.53$ MHz, and $\sqrt{\bar{N}}g_0/2\pi = 350$ kHz. The spectrum is displayed on a logarithmic scale. The region between the white contours is squeeze.

5.4.1 RPSN Needs to be Greater than the Thermal Noise

Thermal motion of the membrane imprints excess noise onto the phase quadrature of the light (Eq. 5.23), which is uncorrelated with the quantum noise in the amplitude quadrature and hence can limit the level of squeezing. To obtain significant squeezing near the mechanical resonance, the level of the optical force, termed radiation pressure shot noise (RPSN), relative to the thermal force driving the membrane should be large [5]. For a beam with laser-cavity detuning near zero, this ratio is given by $R = C/n_{\rm th} \times (1+(2\omega_m/\kappa)^2)^{-1}$ where C is the optomechanical cooperativity and $n_{\rm th}$ is the thermal occupation of the mechanical state.

5.4.2 Quantum Efficiency

Suppose we have an input beam with variance $V(\theta)$. When it passes through a detection system with a quantum efficiency of ϵ, the output variance $V_d(\theta)$ is given by

$$V_d(\theta) = \epsilon V(\theta) + (1 - \epsilon) \tag{5.38}$$

If the input beam is squeezed and described by $V(\theta_s) = 1 - s$ where $s > 0$, we have

$$V_d(\theta_s) = \epsilon(1 - s) + (1 - \epsilon) = 1 - \epsilon s \tag{5.39}$$

The degree of squeezing is attenuated by the quantum efficiency.

5.4.3 Maximum Squeezing with Sufficiently Large Nonlinearity

With sufficient large nonlinearity, the level of squeezing is purely determined by the ratio of RPSN to thermal noise R and the quantum efficiency ϵ. It is found through analytical approximation and numerical comparison that the maximum squeezing one could get is given by

$$\epsilon \frac{R}{1 + R} \tag{5.40}$$

The level of squeezing gives lower bounds on R and the total quantum efficiency ϵ. In the limit of $R \gg 1$, the level of squeezing can be used to calibrate the total quantum efficiency.

5.5 Our System and Experiment

Our optomechanical cavity (see Fig. 5.6 and Ref. [4]) consists of a 40 nm thick by 500 μm square silicon nitride membrane inside of a 3.54 mm long Fabry-Perot optical cavity [3]. We work with the (2,2) drum-head mode of the membrane, with two antinodes along each transverse direction, yielding a mechanical resonance frequency of $\omega_m = 2\pi \times 1.524$ MHz and mechanical dissipation rate $\Gamma_0 = 2\pi \times 0.22$ Hz. With $g = 2\pi \times 33$ Hz, $\kappa = 2\pi \times 1.7$ MHz, and in a helium flow cryostat with a base temperature of 4.6 K, we achieve $R > 5$ when operating

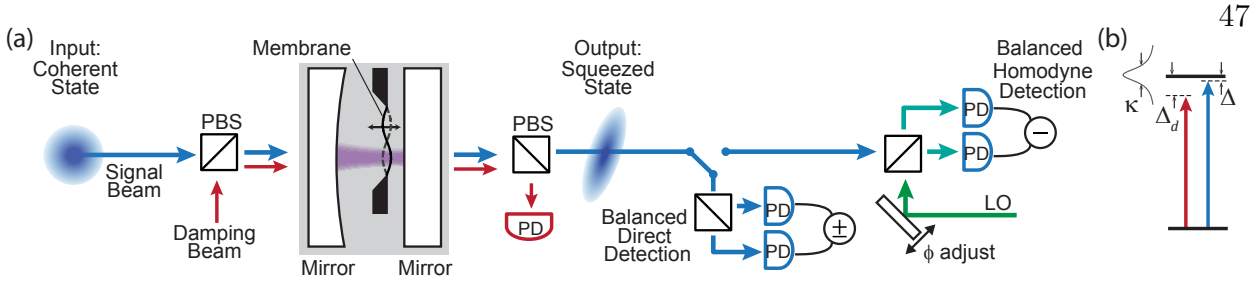

Figure 5.6: Experimental Diagram for Optomechanical Squeezing. (a) The signal beam (blue) enters the optomechanical cavity as a coherent state. After the optomechanical interaction, a squeezed state emerges. The signal beam is detected, either with balanced direct photodetection or with balanced homodyne detection by mixing with an optical local oscillator (LO) (green). A weaker damping beam (red) orthogonally polarized to the signal beam is also injected into the cavity. The two beams are combined before the cavity and separated after the cavity with polarizing beamsplitters (PBS) and detected with photodetectors (PD). (b) Signal and damping beam detunings from the cavity resonance.

with $\bar{N} \sim 10^8$. This ratio is much larger than achieved in previous work [5], mainly due to increased optomechanical coupling. In addition to our main signal beam, we inject another laser into the orthogonal polarization cavity mode. This damping beam has a much weaker power than the signal beam but is detuned by $\Delta_d \sim -\omega_m$ from the cavity resonance. The damping allows us to avoid parametric instability and work with a mechanical mode with an effective mechanical linewidth of $2\pi \times 2.6$ kHz.

5.5.1 Direct Photodetection

In our first set of experiments, we use direct photodetection to measure the power spectrum of the amplitude quadrature, $S_I(\omega)$, which is normalized such that the detected shot noise is unity. Although a Kerr mechanism does not generate squeezing at the amplitude quadrature, we can rotate the quadrature by a single beam with a finite detuning Δ. Off-resonant phase fluctuations are partially converted into intracavity amplitude fluctuations and vice versa. The rotated angle is given by $\phi_c = \tan^{-1}(2\Delta/\kappa)$. Besides, with sufficient large nonlinearity, the squeezed angle is close to the amplitude quadrature (see Eq. 5.19 and Fig. 5.3). Hence only a small amount of detuning is needed in our experiment.

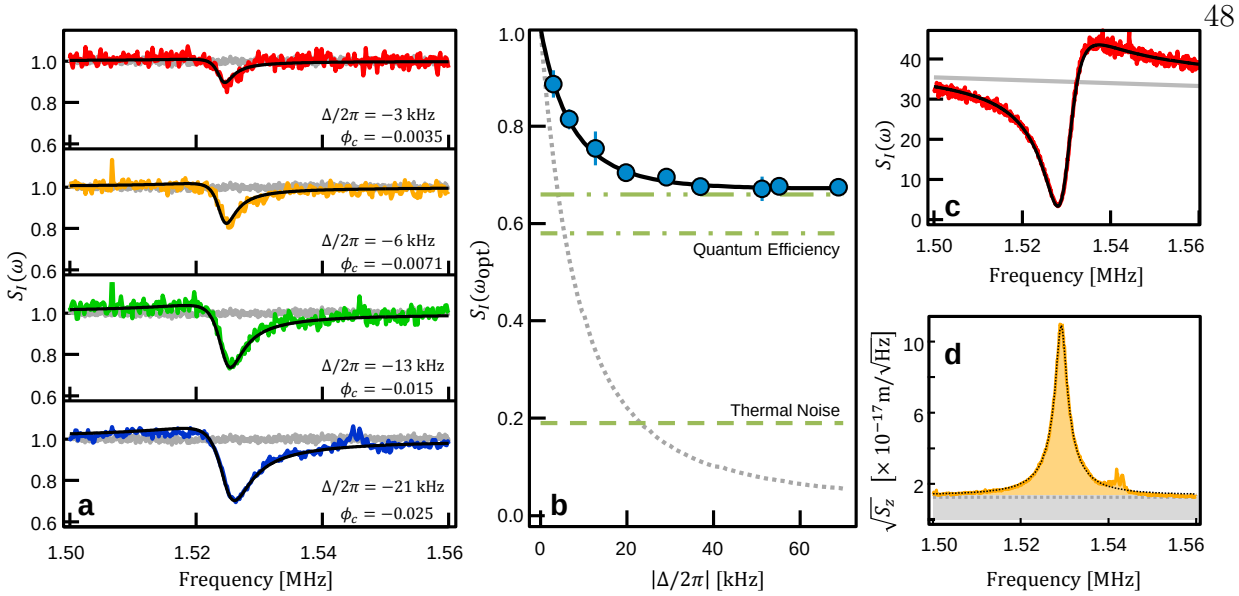

Figure 5.7: Quantum Intensity Noise Suppression. (a) Directly detected optical intensity noise signal beam spectra for several signal beam detunings. Also displayed are the measured shot noise level (gray) and the theoretical predictions (black). A 200 Hz bandwidth is used. The ratio of RPSN relative to thermal drive, R, is fixed at 5.1. The damping beam provides $\Gamma_0^{\rm eff}/2\pi = 2.7$ kHz and $\omega_m^{\rm eff}/2\pi = 1.524$ MHz. However, the total mechanical damping rate and resonance frequency change with the signal beam detuning Δ. (b) The minimum value of S_I for spectra as displayed in (a) (blue circles). Statistical error bars indicate the standard deviation. The frequency where the minimum occurs, $\omega_{\rm opt}$, shifts with Δ due to the optical spring effect. Also displayed are the mechanical thermal noise floor for our current parameters $1/R$ (dashed green), limit set by finite detection efficiency $1-\epsilon$ (dot-dashed green), sum of thermal and detection efficiency limit (dot-dot-dashed green), and expected squeezing in the absence of optical loss and thermal motion (dotted gray). (c) The directly detected optical intensity noise signal beam spectrum with intentionally added white, classical amplitude noise (red), theoretical prediction (black), and level of added amplitude noise (gray). (d) The mechanical displacement spectrum inferred from the damping beam transmission spectrum (orange), and Lorentzian fit (dotted black). Detection noise floor is also shown (dotted gray). One additional peak due to excess noise is visible in the bottom panel of (a) and in (d) at frequencies ~ 1.545 MHz due to a mechanical mode of the cavity support structure. The mode may be thermally occupied or driven by piezo noise.

Figure 5.7(a) shows S_I for several values of Δ, all at an average transmitted signal beam power of 110 μW corresponding to $\bar{N} = 1.1 \times 10^8$ or $R = 5.1$. A dip in noise below the shot noise level is visible in the vicinity of ω_m, a clear signature of squeezed light. The squeezing becomes more pronounced as $|\Delta|$ is increased because the maximally squeezed quadrature is rotated toward the amplitude quadrature. The data shows excellent

agreement over most of its frequency range, with a Heisenberg-Langevin model including quantum-noise-limited input optical fields, a thermally occupied mechanical bath coupled to the membrane, and no other classical noise sources (see appendix B). However, a small excess of classical noise is visible at the largest detuning, a few tens of kHz above the mechanical resonance. Here, cavity frequency noise induced from a thermally occupied mechanical mode of the optomechanical cavity support structure [4] is increasingly converted in amplitude noise at larger $|\Delta|$. All of the system parameters used to generate the theory curves of Fig. 5.7(a) are independently measured, except Δ is calibrated, in part, using the displayed data.

The shot noise level for the data of Fig. 5.7 is calibrated using balanced direct detection (see appendix C). The transmitted signal is split into two equal power beams and directed onto a pair of nearly identical photodetectors. Taking the sum of the detected signals is equivalent to single detector direct detection. However, taking the difference of the detected signals removes classical and quantum correlations. We achieve up to 20 dB common mode suppression. The difference signal consists of only the uncorrelated shot noise level and a small $\sim 5\%$ contribution from the photodetector dark noise. S_I is computed by taking the ratio of the power spectra of the sum and difference signals, after subtracting the measured photodetector dark noise.

The limits of the detected squeezing (Eq. 5.40) are illustrated in Fig. 5.7(b) where the minimum measured value of S_I is plotted as a function of Δ. The finite quantum efficiency of our detection system is the largest limit to the detected squeezing. Including losses associated with the cavity $\epsilon_c = 0.6$, propagation to the photodetector $\epsilon_p = 0.8$, and photodetector conversion efficiency $\epsilon_d = 0.87$, we estimate an overall quantum efficiency of $\epsilon = \epsilon_c \epsilon_p \epsilon_d = 0.42$.

Although the transmitted signal beam intensity spectrum is decidedly non-Lorentzian, the mechanical displacement still follows a simple Lorentzian form. The damping beam transmitted intensity spectrum acts as a probe of mechanical motion uncomplicated by

strong quantum correlations because its intensity, and thus RPSN effects on the membrane are small [5]. The mechanical displacement spectrum derived from the damping beam [Fig. 5.7(d)] shows the mechanics still retains a Lorentzian response to locally white force fluctuations.

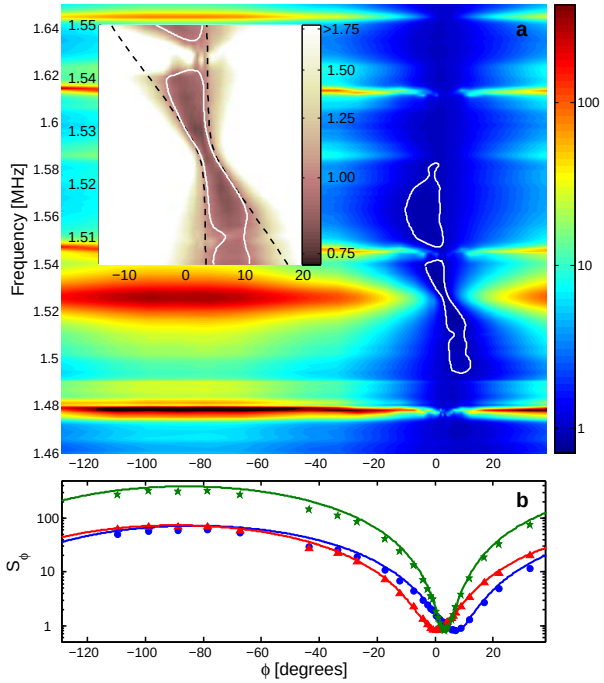

Figure 5.8: Optical Quadrature Spectrum. (a) Color map of S_ϕ. The white contour is at the shot noise level, and the region inside this contour is squeezed. Several additional noise peaks are evident at frequencies away from the mechanical resonance, due to the motion of thermally occupied modes of the support structure. The inset shows the squeezed region in more detail and also includes a theoretical prediction (dashed black) of the expected shot noise contour. The experimental parameters are the same as in Fig. 5.7, except $\Delta/2\pi = -42$ kHz. (b) Cuts through quadrature phase at three different frequencies 1.517 MHz (blue circles), 1.526 MHz (green stars), and 1.535 MHz (red triangles), averaged over a 1 kHz bandwidth, and corresponding theoretical models with no free parameter (colored solid curves).

5.5.2 Balanced Homodyne Detection

We next explore all quadratures of the transmitted signal beam with balanced homodyne detection. We interfere the transmitted signal beam with an optical local oscillator

whose phase is stabilized relative to the signal beam. Different quadratures can be detected by adjusting the relative phase between the local oscillator and the signal beam. In Fig. 5.8(a), optical quadrature spectra, $S_\phi(\omega)$, over varying quadrature phase, ϕ, are displayed. S_ϕ is normalized such that the measured shot noise level is unity. The phase $\phi = 0$ corresponds with the amplitude quadrature and gives information equivalent to that obtained in the direct detection discussed above. (Note, for these measurements $\Delta = -2\pi \times 42$ kHz, allowing some squeezing to be rotated into the amplitude quadrature.) Regions with noise spectral density below the shot noise level are visible over a frequency range of ~ 100 kHz, and ϕ ranging over tens of degrees. The range of observed squeezing is limited to a region smaller than predicted by theory because of the thermal motion of the cavity mirrors and support structure mentioned above. The depth of the observed squeezing in homodyne detection is also lower than that observed in direct detection. This is partially accounted for by imperfect overlap between the probe beam and homodyne local oscillator, contributing an additional effective optical loss, $\epsilon_m = 0.8$. Also, we operate in a regime where the homodyne local oscillator power is only a factor of less than 10 larger than the probe power, making the measurement slightly susceptible to the noise of the local oscillator (see appendix B and C).

Homodyne detection also allows us to quantify the coherent amplification of optical quantum fluctuations in our measurement. In Fig. 5.8(b), we compare our data to a theoretical calculation based upon a Heisenberg-Langevin model. The agreement between the model and the data allows us to interpret the large noise spectral density ($S_\phi \sim 330$) near the phase quadrature at $\phi = \pm 90°$ as arising mainly from coherent amplification of quantum noise or so-called anti-squeezing. This amplification persists despite the large imaginary component of the mechanical response, which has the potential to limit squeezing and add thermal noise.

5.6 Discussion, Conclusions, and Future Aspects

5.6.1 A Kerr Medium with Finite Response Time

It is worthwhile to discuss the meaning of the complex Kerr coefficient. A consequence of the imaginary component of the Kerr coefficient is that our system has a finite response time. The delay time can be calculated by differentiating the phase response versus frequency:

$$\tau(\omega) = -\frac{\partial}{\partial\omega}\Big[\arg[\tilde{r}(\omega)]\Big] = -\frac{\partial\phi_r(\omega)}{\partial\omega}, \tag{5.41}$$

where $\tilde{r}(\omega) = r(\omega)e^{i\phi_r(\omega)}$. Now we separate the discussion by the resonance case and off-resonance case. On mechanical resonance, it can be found that the delay time is just the response time of the mechanical resonator:

$$\tau(\omega_m) \sim -\frac{\partial}{\partial\omega}\Big[\arg[\chi_m(\omega)]\Big]\Big|_{\omega=\omega_m} = 2/\Gamma_0^{\text{eff}}, \tag{5.42}$$

provided that $\kappa \gg \Gamma_0^{\text{eff}}$. The response time is inversely proportional to the effective mechanical linewidth. While the response time can be reduced by optomechanical damping, the optomechanical Kerr coefficient will reduced accordingly. In fact,

$$\text{peak nonliearity} \times (\text{response time})^{-1} \sim |r(\omega_m)|/\tau \sim 2C/(2/\Gamma_0^{\text{eff}}) = 4(g\bar{a})^2/\kappa \tag{5.43}$$

$$\text{peak nonliearity} \times \text{squeezing bandwidth} \sim |r(\omega_m)|\Gamma_0^{\text{eff}} \sim 2C\Gamma_0^{\text{eff}} = 8(g\bar{a})^2/\kappa \tag{5.44}$$

In other words, the *resonant-enhanced* optomechanical Kerr nonlinearity comes with the price of the finite response time and a finite bandwidth. We typically operate the system with an effective mechanical linewidth of 1 kHz. This corresponds to a Kerr coefficient of 100 and a response time of 1 ms.

For the off resonance case, I plot $|\tilde{r}(\omega)|$ and $\tau(\omega)$ in Fig. 5.9. While both functions peak at mechanical resonance and decay at off-resonance, they have different lineshapes. It turns out that the maximum of $|\tilde{r}(\omega)|/\tau(\omega)$ occurs at a few mechanical linewidth away from the mechanical resonance.

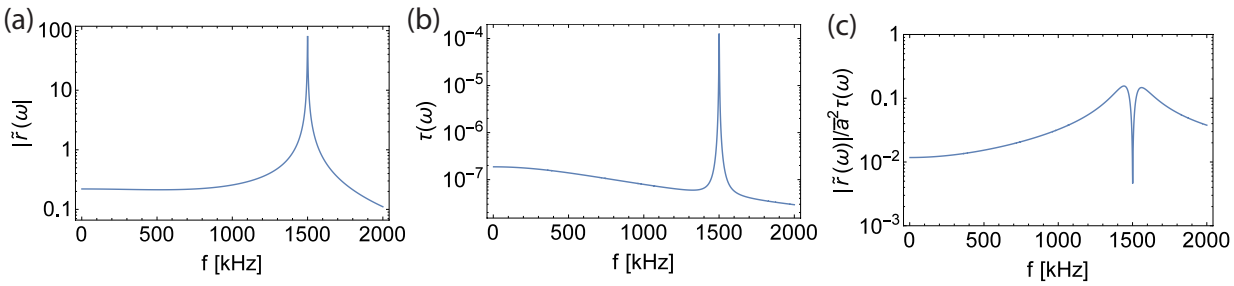

Figure 5.9: Optomechanical Kerr coefficient $|\tilde{r}(\omega)|$ and delayed time $\tau(\omega)$ from DC to mechanical frequency. (a) $|\tilde{r}(\omega)|$ as a function of frequency. It peaks at the mechanical resonance (1500 kHz) and flatten at DC. (b) The delayed time $\tau(\omega)$ as a function of frequency. It also peaks at the mechanical resonance, but a different lineshape. (c) The ratio of $|\tilde{r}(\omega)|$ to $\tau\omega$. We normalize it by photon number in the cavity $\bar{a}^2 \sim 10^8$. The maximum occurs at a few mechanical linewidth away from the mechanical resonance.

The Kerr mechanism is a third order nonlinearity. Here we compare the optomechanical nonlinearity achieved in this squeezing experiment to other $\chi^{(3)}$ mechanisms. While the nonlinearity strength of different mechanism can vary by ten orders of magnitude, the nonlinear strength divided by the response time is roughly the same [73]. In the following table, I calculate the Kerr coefficient per photon ($r_{\mathrm{Kerr}}/\bar{a}^2$) for a few nonlinear mechanisms and divide it by their response time ($r_{\mathrm{Kerr}}/\bar{a}^2\tau$). Here I assume interaction length L for each mechanism is 1 cm (see Eq. 5.14), except for the optomechanical Kerr nonlinearity. With the experimental parameters in the chapter, the optomechanical Kerr coefficient is large compared with that of other mechanisms, but its Kerr coefficient divided by its response time is comparable.

Mechanism	n_2 (cm^2/W)	Response time (sec)	$r_{\mathrm{Kerr}}/\bar{a}^2$	$r_{\mathrm{Kerr}}/(\bar{a}^2\tau)$ (sec^{-1})
Electronic polarization	10^{-16}	10^{-15}	10^{-15}	1
Molecular orientation	10^{-14}	10^{-12}	10^{-13}	0.1
Electrostriction	10^{-14}	10^{-9}	10^{-13}	10^{-4}
Saturated atomic absorption	10^{-10}	10^{-8}	10^{-9}	0.1
Thermal effects	10^{-6}	10^{-3}	10^{-5}	10^{-2}
optomechanics	NA	0.1-10^{-3}	10^{-6}	10^{-3}

5.6.2 Conclusions and Future Aspects

In conclusion, we have experimentally demonstrated that an optomechanical system well into the RPSN dominated regime is capable of creating squeezed light. The 1.7 dB strength of optomechanical squeezing we achieve is significantly larger than previous optomechanical realizations [69, 70]. However, stronger squeezing has, of course, been realized with more developed techniques [58]. Increasing detection efficiency and reducing thermal noise will be required to study the ultimate limits to deeply ponderomotively-squeezed light.

Employing the PnC-shield membrane with ultrahigh Q described in Chapter 4 will reduce thermal noise. In addition, the phononic bandgap will eliminate the extraneous noise due to the substrate modes [Fig. 5.7(d) and Fig. 5.8].

Chapter 6

Optomechanical Raman-Ratio Thermometry

In this chapter, I discuss the first optomechanical experiment that utilized the PnC-shielded membrane described in Chapter 4. Exceptionally good isolation from the environment by the PnC allows us to perform optomechanical Raman-ratio thermometry at variety of environment temperatures. For this experiment, I integrated the PnC-shield membrane with the optical cavity, contributed to data taking and analysis, and helped with the manuscript. A number of the figures and much of the text is taken directly from Ref. [7] written in conjunction with Thomas Purdy, Robert Peterson, Nir Kampel, Katarina Cicak, and Raymond Simmonds.

6.1 Introduction

Raman light scattering has proven to be a robust and powerful technique for in situ thermometry. Many material-specific properties governing Raman transitions, such as the Stokes shift, spectral linewidth, and scattering rate vary with temperature. However, for any Raman system the ratio of spontaneously scattered Stokes versus anti-Stokes photons is a direct measure of the initial population of the motional state. For example, at zero temperature the process of anti-Stokes scattering, which attempts to lower the motional state below the ground state, is entirely suppressed; whereas the Stokes scattering, which raises the motional state, is allowed. For thermally occupied states, an absolute, self-calibrating temperature measurement is possible by measuring this asymmetry in Raman scattering. Distributed

optical fiber sensors [74] and solid state systems [75, 76, 77] make use of spontaneous Raman scattering between optical phonon levels for temperature measurements, and combustion chemistry diagnostics use rotational-vibrational molecular levels in a similar fashion [78].

In principle, Raman scattering from any mechanical degree of freedom in a solid-state environment has the potential to provide local temperature measurements, but for low-frequency micromechanical resonances, this is a considerable challenge. Recent experiments in the field of quantum cavity optomechanics [79, 80, 81] use cavity enhancement to collect Raman-scattered light from localized acoustic resonances demonstrating the Stokes/anti-Stokes asymmetry. However, the potential for using this asymmetry to perform absolute, self-calibrated thermometry remains relatively unexplored. Here we measure the asymmetry of Raman scattering in a membrane-in-cavity optomechanical system (Fig. 6.1) over a wide range of physical temperatures between 4.8 K and 50 K. We find agreement with conventional thermometry over this range to within ten percent, and we discuss the sensitivity of the measurement to a variety of parameters.

In our optomechanical system, the motional states are the MHz frequency vibrational levels of a membrane mechanical resonator, and an optical resonance is provided by an optical cavity surrounding the membrane. Departing from previous measurement schemes [79, 81], the Stokes and anti-Stokes peaks are simultaneously derived from a single, resonant laser tone. The Raman asymmetry becomes more pronounced in certain mechanical normal modes of the resonator when they are optically cooled near their ground state with a separate laser tone. We are able to realize a damped displacement spectral density near the membrane resonance frequency equal to that expected from a resonator occupied with as low as $\bar{n} \sim 2$ vibrational quanta (150 μK effective temperature) [82, 83, 84, 85]. We then measure the physical temperature of our device by extrapolating the Raman sideband asymmetry to zero optical damping.

6.2 Principle of Raman-Ratio Thermometry

Raman-ratio thermometry is based on the idea that at a finite temperature the ground state manifold of the Raman levels is occupied according to a well understood statistical weighting. The ratio of Stokes to anti-Stokes Raman transitions is equal to $R_{sa} = e^{\hbar\omega_m/k_bT} = (\bar{n}+1)/\bar{n}$, where ω_m is the mechanical resonance frequency and T is the temperature [86, 87]. The spectrum of Raman scattered light transmitted through an optomechanical cavity (Fig. 6.1(b)) is given by:

$$S(\omega) \propto \frac{\bar{n}}{\left(\frac{\Gamma_m}{2}\right)^2 + (\omega_m - \omega)^2} + \frac{\bar{n}+1}{\left(\frac{\Gamma_m}{2}\right)^2 + (\omega_m + \omega)^2}.$$

This assumes the laser is resonant with the optical cavity, and the optical cavity linewidth is much larger than Γ_m. The first (second) term corresponds to anti-Stokes (Stokes) scattering peak shifted by ω_m ($-\omega_m$) from the input laser frequency, and ω is the frequency relative to the input laser frequency. The peaks are broadened by the mechanical linewidth, Γ_m. Taking the ratio of the amplitude of the Stokes and anti-Stokes peaks directly yields the mechanical occupation, $\bar{n} = 1/(R_{sa} - 1)$.

6.3 Experimental Setup

We use the membrane-in-cavity optomechanical system in the helium flow cryostat described in Chapter 5 [Fig. 6.1(a)]. The cryostat temperature, T_0, is set in the range of 4.8 to 50 K. We have employed two devices for our measurements. The data shown in 6.2(a) focus on the $(2,2)$ mode of a 500 μm square by 40 nm thick membrane, with resonance frequency $\omega_m^{(2,2)}/2\pi = 1.509$ MHz and intrinsic linewidth $\Gamma_0^{(2,2)}/2\pi = 0.46$ Hz. The data shown in Figs. 6.2(b) and 6.3 are primarily from the $(3,2)$ mode of a 375 μm square by 100 nm thick membrane, $\omega_m^{(3,2)}/2\pi = 2.637$ MHz, $\Gamma_0^{(3,2)}/2\pi = 0.84$ Hz, which is shielded by a PnC substrate described in Chapter 4. The acoustic band structure is engineered to provide

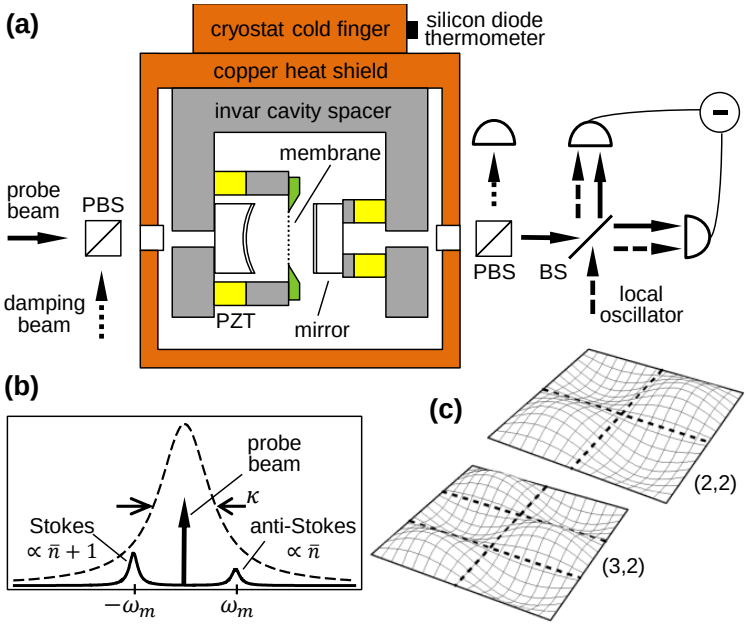

Figure 6.1: Optomechanical Raman-ratio thermometry. (a) Two orthogonally polarized laser beams are coupled into a cryogenic membrane-in-cavity optomechanical system. Raman scattered light from the resonant probe beam is analyzed with balanced heterodyne detection. The red detuned damping beam Raman sideband cools membrane motion. Beam splitter (BS), polarizing beam splitter (PBS), piezoelectric transducer (PZT). (b) The spectrum of transmitted probe beam light shows Raman scattering peaks shifted by $\pm\omega_m$, where ω_m is the mechanical resonance frequency. The asymmetry in the spectral peaks, dependent on the effective thermal occupation of the mechanical mode, forms the basis for a self-calibrating thermometer. Also indicated is the spectral response of the optical cavity (dashed curve). (c) Spatial profile of the $(2,2)$ and $(3,2)$ drumhead mode of the membrane.

a gap in the substrate mechanical mode density around the $(3,2)$ mode[1] , which diminishes noise from thermally occupied modes of the substrate [16, 88].

The optical cavity consists of two mirrors separated by 3.5 mm, each with 10^{-4} fractional transmission. The optical linewidth, κ, is dependent on the location of the membrane in the cavity [38], and is on the order of a few Megahertz. Optomechanical coupling is achieved as the optical resonance frequency is modulated by the displacement of the vibrating membrane along the optical standing wave. This interaction is characterized by a single

[1] We note that measured mechanical resonances of all of the membrane modes are shifted lower in frequency compared to those reported in this reference. This shift moves the (3,2) resonance closer to the center of mechanical band gap. The change may be the result of a stress reduction due to differences in sample mounting technique, mass loading from surface contamination, or device aging.

photon coupling rate of $g_0^{(2,2)}/2\pi = 33$ Hz for the data in Fig. 6.2(a) or $g_0^{(3,2)}/2\pi = 18$ Hz for the data in Fig.6.2(b) and Fig. 6.3. The cavity is driven with two orthogonally polarized laser beams derived from the same 1064 nm laser source (Fig. 6.1(a)). The probe beam is actively stabilized to be resonant with the optical cavity. The transmitted Raman scattered light from this beam is analyzed with an optical heterodyne detection system. The orthogonal polarization mode is driven by the damping beam, which is tuned to a frequency lower than the optical resonance.

6.4 Optical Damping and Effective Mode Temperature Measurement

For the red-detuned damping beam, the anti-Stokes scattering rate is resonantly enhanced by the cavity [86, 87]. Each anti-Stokes scattered photon that exits the cavity carries one vibrational quantum of energy out of the system. The mode reaches an equilibrium when the optical cooling rate is matched by the rate at which thermal excitations enter the system. The effective temperature of a mode is approximately $T_{\text{eff}} = T_0 \frac{\Gamma_0}{\Gamma_m}$, in the experimentally relevant case where $\Gamma_0 \ll \Gamma_m \ll \kappa$, here Γ_m is the optically induced mechanical damping rate, and Γ_0 is the intrinsic mechanical damping rate. The cooling is more efficient when the resolved sideband parameter $\omega_m/\kappa \gg 1$. However, such a ratio will suppress the Raman peaks generated by the resonant probe beam. We build our system with $\omega_m/\kappa \sim 1$ so that we can maintain cooling efficiency and detect the Raman signals generated by one probe beam.

By varying the power of the damping beam, we are able to damp motion and reduce the effective mode temperature by up to a factor of 3×10^4. We take the Stokes/anti-Stokes peak amplitudes generated by the resonant probe beam as the damping beam power, P_d, is increased. The power of the transmitted probe beam, P_p, is held at constant. As expected, the height of the anti-Stokes peak decreases with damping beam power as the mode is cooled. For weak damping the two Raman peaks are equal in amplitude, whereas at strongest damping the Stokes peak is 50% larger than the anti-Stokes peak as the mode

approaches its quantum ground state. From the Stokes/anti-Stokes ratio we compute the effective temperature of the mode, as displayed in Fig. 6.2. Raman-ratio thermometry indicates that for frequencies near ω_m, the (2,2) mode reaches $\bar{n}(\omega_m) = 2.1 \pm 0.2$. However, for this mode, the occupations measured over a wide range of damping beam power are systematically ∼15% larger than predicted by Raman sideband cooling. This discrepancy, which is absent in the PnC-isolated (3,2) mode [Fig. 6.2(b)], is likely due to the influence of substrate motion and is discussed below.

To compute the effective temperature of the mode, we numerically integrate the Raman peaks over a 4 kHz span around the mechanical resonance and calculate their ratios. This narrowband analysis minimizes the effect of noise from the thermally-occupied mechanical modes of the non-PnC substrate [16, 4]. Besides, the mechanical occupation near the resonance is a relevant figure of merit for many applications of optomechanics, including resonant force sensing and the generation of optomechanically-squeezed light [6]. The analysis indicates that the (2,2) mode reaches $\bar{n}(\omega_m) = 2.1 \pm 0.2$. We stop at this number because the extraneous noise is significant. In addition, for this mode, the occupations measured over a wide range of damping beam power are systematically ∼15% larger than predicted by Raman sideband cooling. This discrepancy, which is absent in the PnC-isolated (3,2) mode (Fig. 6.2(b)), is likely due to the influence of substrate motion.

It is worthwhile to discuss the mechanical occupation one can reliably measure with Raman-ratio thermometry. The sensitivity is ultimately limited by the Heisenberg measurement-disturbance uncertainty principle. As we increase the probe beam power to increase the signal to noise ratio, the optical forces from the shot noise (radiation pressure shot noise, RPSN) [5] will increase as well. The RPSN-driven motion set the lowest temperature one can measure. In the data of $\bar{n}(\omega_m) = 2.1$, the signal to noise ratio is ∼1 dB. The contribution from RPSN is 0.2 quantum.

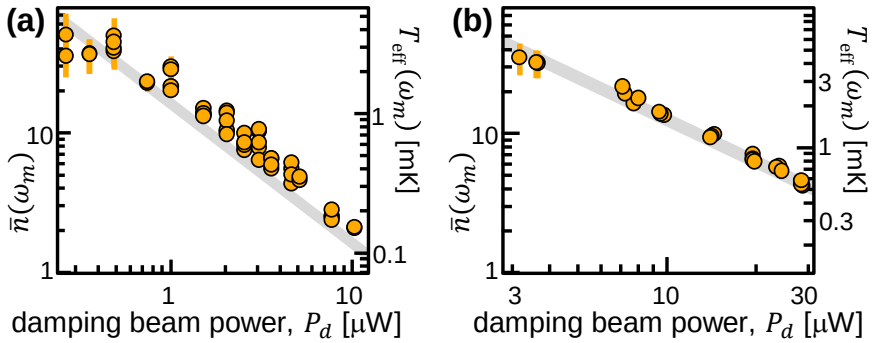

Figure 6.2: Effective mode occupation at mechanical resonance. Numerically integrating the Raman peaks over a 4 kHz span around the mechanical resonance and taking their ratio yields a measure of the mode effective temperature (orange circles) for (a) the (2,2) mode of the non-PnC device and (b) the (3,2) mode of the PnC device. Due to decreased optomechanical coupling, the (3,2) mode does not reach as low a mechanical occupation as the (2,2) mode. Gray bands are the prediction of Raman sideband cooling whose width stems from uncertainty in T_0 as measured by the diode thermometer. Vertical error bars represent estimated statistical standard deviation.

6.5 Physical Temperature Measurement

We next consider Raman-ratio thermometry as a means to determine the physical temperature of the device. Here we employ a membrane resonator embedded in a PnC substrate, which reduces the effects of substrate motion to a level below the statistical noise. The Raman asymmetry of undamped modes is small ($\sim 10^{-4}$) and precludes directly ascertaining the physical device temperature. Nevertheless, with our ability to perform strong optomechanical cooling, we can extrapolate the temperature of the undamped membrane modes from measurements of the asymmetry as a function of optical damping (Fig. 6.3(a)). The undamped occupation of the mechanical mode is given by $(dR_{sa}/dP_d)^{-1} \times d\Gamma_m/dP_d \times 1/\Gamma_0$.

Here we employ a membrane resonator embedded in a PnC substrate, which reduces the effects of substrate motion to a level below the statistical noise. Thermometry is performed on the $(3, 2)$ mode with the cryostat held at several different temperatures between 4.8 K and 50 K. In Fig. 6.3(c) the extrapolated temperatures are compared to the temperature as measured by a silicon diode thermometer attached to the cryostat. The results agree within

the statistical uncertainty with an average deviation of less than 10%. As an additional confirmation, we perform the same thermometry procedure on the $(5,2)$ mode, which is also located in a phononic band gap of the substrate and find agreement with the previous measurements. However, the statistical error on the $(5,2)$ mode measurement is much larger because the optomechanical coupling is smaller than to the $(3,2)$ mode.

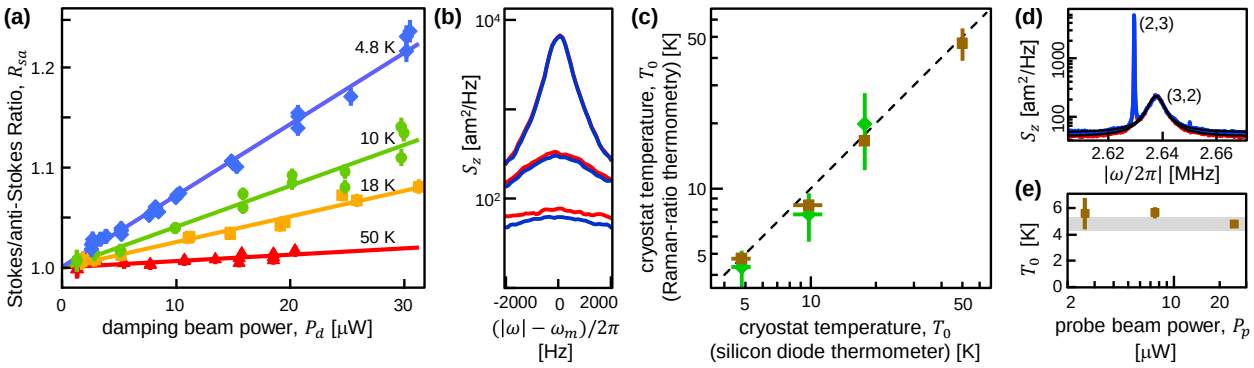

Figure 6.3: (a) Stokes/anti-Stokes peak ratio for the $(3,2)$ mode at four cryostat temperatures. Solid curves are linear fits to the data. $P_p = 26$ μW and $\kappa/2\pi = 2.7$ MHz. (b) Stokes (red) and anti-Stokes (blue) spectra near the (3,2) mode for P_d of 3.2 μW (top), 14 μW (middle), and 28 μW (bottom). Resolution bandwidth is 100 Hz. (c) Comparison of Raman-ratio thermometry with silicon diode thermometer for the $(3,2)$ mode (brown squares) and $(5,2)$ mode (green diamonds). Dashed line indicates agreement between the two methods. (d) Raman spectra of (2,3) and (3,2) mode at $P_d = 25$ μW. Black curves are fit Lorentzians excluding the region around the (2,3) mode. (e) Extracted temperature, T_0, for various probe powers. Vertical error bars in (a), (c), and (e) represent estimated statistical standard deviation. Horizontal error bars in (c) and width of gray band in (e) represent a combination of the diode thermometer accuracy (± 0.5 K) and inaccuracy introduced by drift and oscillations in the temperature over the span of the measurement.

6.6 Systematic Error

Thermometry relying on sideband asymmetry does not require accurate knowledge of often-difficult-to-measure system parameters such as the optomechanical coupling rate, effective modal mass, circulating optical power, or optical detection efficiency. Additionally, the single-resonant-probe method [80] employed in this work reduces the sensitivity to

many systematic errors as compared to techniques that employ multiple off-resonant probe tones [79, 81]. Such effects include drift in the relative amplitude of the probes, optomechanical modification of the mechanical susceptibility, coherent optomechanically induced interference between the probes [89], and increased sensitivity to classical laser noise [90]. However, many systematic effects in our system can lead to in temperature determination, and we now discuss several of these potential error sources.

A necessary external input parameter to extract the physical temperature is the intrinsic mechanical linewidth, which is measured via mechanical ringdown with an uncertainty of a few tenths of a percent. However, long term drift in the mechanical linewidth can be at the percent level. The intrinsic linewidth is recorded at each cryostat temperature, and found to increase from 0.84 Hz at 4.8 K to 1.07 Hz at 50 K. The optically-damped mechanical linewidths are obtained by Lorentzian fits to Raman spectra.

Heating induced by absorbed laser light can cause thermal gradients between the membrane and silicon diode thermometer and increase $\bar{n}$. We see no evidence for absorptive heating, which would cause deviations from linearity in the data of Fig. 6.3(a).Another, more fundamental, systematic effect is the RPSN drive motion, as discussed above. It contributes 0.2 K to T_0 for $P_p = 26$ μW probing the $(3, 2)$ mode. We apply this correction to the extracted physical temperature data in Fig. 6.3(c) and the theoretical expectation bands of Fig. 6.2.

In addition to the quantum noise of the probe beam, optomechanically mediated correlations in the classical laser noise can also lead to systematic error. Such noise-squashing or noise-cancellation effects can change the relative heights of the Raman peaks leading to an underestimate of the effective mode occupation [90, 91, 81]. To assess this systematic, we have independently measured the classical phase and amplitude noise as well as the detuning of the input probe beam (see appendix C). These measurements constrain the potential error [90] on temperature due to classical laser noise correlations to be at the percent level or less under all operating conditions. Additionally, we have reduced the probe beam power by

an order of magnitude and observed only a weak trend in extracted temperature (Fig. 6.3(e)), which confirms that the effects of both classical laser noise and absorptive heating are small.

The $(3, 2)$ membrane mode is nearly degenerate with the $(2, 3)$ mode, with a frequency difference between the two modes of 7.2 kHz (Fig. 6.3(d)). For all values of employed optical damping, the (3,2) mode and (2,3) mode are well resolved in the spectra. For thermometry, Raman peaks are always compared within ± 2 kHz of the peak of $(3, 2)$ mode resonance. Thus we believe the presence of the $(2, 3)$ mode is a negligible perturbation on the thermometry data shown in Fig. 6.3. Increasing the optical damping well beyond the level presented here could cause mode hybridization and significantly complicate the interpretation of the Raman spectra [92].

6.7 Conclusion

In conclusion, we have shown that Raman asymmetry is a viable technique to diagnose both the effective mode temperature of an optically damped membrane resonator and the physical temperature of the same device. These measurements demonstrate the self-calibrating nature of the method and elucidate many of the systematic uncertainties. Our results show that the quantum effects governing the asymmetry [93, 81] are visible in a membrane-in-cavity optomechanical system operated within an order of magnitude of room temperature.

The PnC substrate has reduced our susceptibility to noise from thermally occupied mechanical modes of the substrate [16]. Without PnC isolation, we have observed that frequency noise of the optical resonance due to substrate motion can contribute a systematic uncertainty in Raman-ratio thermometry at the tens of percent level.

Chapter 7

Future Directions and Conclusions

We see a bright future for the quantum optomechanics with PnC-shielded, high-stress membranes. For the first generation of the devices, we observed sideband asymmetry even at 50K. In the course of writing this thesis, the third generation of the PnC devices entered a deep RPSN regime. We operated a PnC-shielded membrane in a 1.7 mm-long Fabry-Perot cavity in a dilution refrigerator. We observed a mode of 17 million Q and cooled it to the ground state with a phonon occupation of less than 0.2. The experiment paves the way for evading measurement backaction, beating the standard quantum limit, and realizing mechanical squeezed states. For future devices we now collaborate with Norcada Inc. to optimize the device quality and yield. It would also be interesting to investigate the highest Q-frequency product one can get with Si_3N_4 membrane shielded by the PnC. We also learned that the membrane is highly functionalizable. For example, the device for microwave to optical frequency conversion in our group utilize the metalized membrane. Its mechanical dissipation can be engineered with the curvature map and the PnC developed in this thesis.

Appendix A

High-Stress Membrane Mechanics

In the world of elasticity, a membrane is a thin film under high tension. The restoring force of a membrane mode is dominated by tensile rather than internal elastic stress. As such, the elastic contribution (i.e. the term associated with the Young's modulus) is ignored in the equation of motion for a vibrating membrane. However, we find that even though the elastic contribution in membrane resonant frequencies is negligible, it plays a significant role in the mechanical dissipation of our membrane. Therefore, our equation of motion must include both the elastic and the tensile stress contribution. The proper jargon of such object in elasticity is "a plate with uniform boundary tension" or "a plate with hydrostatic inplane force".

A.1 Equation of Motion

For an isotropic plate with uniform boundary tension, the differential equation for a transverse mode $w(x, y, t)$ is [22]

$$D\nabla^4 w - \sigma h \nabla^2 w + \rho \frac{\partial^2 w}{\partial t^2} = 0, \tag{A.1}$$

where D is the flexural rigidity defined by $D = Eh^3/[12(1-\nu^2)]$, E is the Young's modulus, h is the plate thickness, ν is the Poisson's ratio, σ is the inplane stress, and ρ is the mass per unit volume. Assuming sinusoidal oscillation, Eq. A.1 becomes

$$D\nabla^4 W - \sigma h \nabla^2 W - \rho\omega^2 W = 0. \tag{A.2}$$

In Cartesian coordinates it reads

$$D\left\{\frac{\partial^4 W}{\partial x^4}+\frac{\partial^4 W}{\partial y^4}+2\frac{\partial^4 W}{\partial x^2\partial y^2}\right\}-\sigma h\left\{\frac{\partial^2 W}{\partial x^2}+\frac{\partial^2 W}{\partial y^2}\right\}=\rho\omega^2 W. \tag{A.3}$$

It is convenient to express the equation in dimensionless form. For a square plate with side length l, let $\xi = x/l$, $\eta = y/l$, and $\Omega = \omega\sqrt{\rho l^2/\sigma}$:

$$\frac{D}{\sigma h l^2}\left\{\frac{\partial^4 W}{\partial \xi^4}+\frac{\partial^4 W}{\partial \eta^4}+2\frac{\partial^4 W}{\partial \xi^2\partial \eta^2}\right\}-\left\{\frac{\partial^2 W}{\partial \xi^2}+\frac{\partial^2 W}{\partial \eta^2}\right\}=\Omega^2 W. \tag{A.4}$$

A.1.1 Boundary Condition

There are three types of boundary conditions for the modes of a vibrating plate: clamped, simply-supported (pinned), and free boundary conditions (see Fig. X). The correct boundary condition for all four sides are the clamped boundary condition. That is

$$W(\xi,\eta)\Big|_{\text{all edges}}=\frac{\partial W(\xi,\eta)}{\partial n}\Big|_{\text{all edges}}=0, \tag{A.5}$$

where n is the axis perpendicular to the edge.

A.2 Normal Modes of a High-Tension Plate

To solve Eq. (A.6) with boundary condition Eq. (A.5), note that the coefficient of the cross term $2\partial^4 W/\partial\xi^2\partial\eta^2$ is small for our devices: $2D/(\sigma h l^2) \sim 10^{-6} \ll 1$. Therefore, we can apply standard perturbation theory with $\epsilon \equiv 2D/(\sigma h l^2)$ as the "small parameter" and $\partial^4/\partial\xi^2\partial\eta^2$ as the perturbation operator.

$$\frac{D}{\sigma h l^2}\left\{\frac{\partial^4 W}{\partial \xi^4}+\frac{\partial^4 W}{\partial \eta^4}\right\}-\left\{\frac{\partial^2 W}{\partial \xi^2}+\frac{\partial^2 W}{\partial \eta^2}\right\}+\underbrace{\frac{2D}{\sigma h l^2}\frac{\partial^4 W}{\partial\xi^2\partial\eta^2}}_{\text{perturbation term}}=\Omega^2 W. \tag{A.6}$$

Then the unperturbed equation can be solved by separation of variables. Let $W(\xi,\eta) = X(\xi)Y(\eta)$, $\Omega^2 = \Omega_\xi^2 + \Omega_\eta^2$, and $E' = E/(1-\nu^2)$. We have

$$\begin{aligned}
&\frac{E'h^2}{12\sigma l^2}\frac{\partial^4 X}{\partial\xi^4}-\frac{\partial^2 X}{\partial\xi^2}=\Omega_\xi^2 X, \quad X\Big|_{\xi=0,1}=\frac{\partial X}{\partial\xi}\Big|_{\xi=0,1}=0,\\
&\frac{E'h^2}{12\sigma l^2}\frac{\partial^4 Y}{\partial\eta^4}-\frac{\partial^2 Y}{\partial\eta^2}=\Omega_\eta^2 Y, \quad Y\Big|_{\eta=0,1}=\frac{\partial Y}{\partial\eta}\Big|_{\eta=0,1}=0.
\end{aligned} \tag{A.7}$$

These are just the dimensionless equations of doubly clamped beams with Young's modulus $E'$and pre-stress σ .

A.2.1 1D Eigensolutions

The eigensolutions $u_m(\xi)$ and the corresponding frequencies Ω_m of Eq. A.7 are given by [94]

$$u_m(\xi) = \begin{cases} v_m(\xi), & 0 \le \xi \le \frac{1}{2} \\ (-1)^{m+1} v_m(1-\xi), & \frac{1}{2} < \xi \le 1 \end{cases} \tag{A.8}$$

$$v_m(\xi) = \sqrt{2a} \left\{ \sin[\beta_m \xi] + \frac{\beta_m}{\alpha_m} \left(\exp[-\alpha_m \xi] - \cos[\beta_m \xi] \right) \right\} \tag{A.9}$$

$$\Omega_m \sim m\pi. \tag{A.10}$$

In Eq. (A.9) $a \ll l$ is the vibration amplitude, and α_m and β_m are defined as

$$\begin{aligned} \alpha_m &= \left(\frac{1}{\epsilon}\right)^{1/2} \left(1 + \sqrt{1 + 2\epsilon\Omega_m^2}\right)^{1/2} \\ \beta_m &= \left(\frac{1}{\epsilon}\right)^{1/2} \left(-1 + \sqrt{1 + 2\epsilon\Omega_m^2}\right)^{1/2}. \end{aligned} \tag{A.11}$$

Note that $\beta_m/\alpha_m \ll 1$ if the mode index is not too large. The mode $u_m(\xi)$ have a sinusoidal shape with an small exponential correction near the edge for the clamped boundary condition. The solutions with intermediate ϵ are given in Ref. [94].

A.2.2 Zero-Order Solution

The products $\{u_m(\xi)u_n(\eta)\}$ are then the solutions of the unperturbed equation. The normal modes of the plate, however, must be symmetrized because of the degeneracy:

$$W_{mn}^{(0)}(\xi,\eta) = \begin{cases} \frac{1}{\sqrt{2}}\Big(u_m(\xi)u_n(\eta) + u_n(\xi)u_m(\eta)\Big), & m > n \\ \frac{1}{\sqrt{2}}\Big(u_m(\xi)u_n(\eta) - u_n(\xi)u_m(\eta)\Big), & m < n \\ u_m(\xi)u_m(\eta), & m = n \end{cases} \tag{A.12}$$

$$\Omega_{mn}^{(0)\ 2} = \Omega_m^2 + \Omega_n^2. \tag{A.13}$$

The orthogonality condition is

$$\frac{1}{a^2}\int_0^1\int_0^1 W_{mn}^{(0)}(\xi,\eta)W_{m'n'}^{(0)}(\xi,\eta)d\xi d\eta = \delta_{mm'}\delta_{nn'}. \tag{A.14}$$

A.2.3 First Order Correction

It turns out the zero-order solution is already an excellent approximation. To see that, we now calculate the first-order correction due to the perturbation term. Note that for $m \neq n$, $\Omega_{mn}^{(0)} = \Omega_{nm}^{(0)}$, i.e., the modes $W_{mn}^{(0)}(\xi,\eta)$ and $W_{nm}^{(0)}(\xi,\eta)$ are degenerate. Hence we need degenerate perturbation theory. Note that the perturbation operator is diagonalized in the basis set $\{W_{mn}^{(0)}(\xi,\eta)\}$. Thus, we can easily calculate the eigenfrequencies to first order Ω_{mn} and the mode shapes with the first order correction $W_{mn}(\xi,\eta)$. We can estimate the contribution from the first-order correction by the following calculation:

$$\begin{aligned} &\left|\frac{\Omega_{mn}{}^2 - \Omega_{mn}^{(0)\ 2}}{\Omega_{mn}^{(0)\ 2}}\right| \sim \frac{\epsilon\pi^2 m^2 n^2}{m^2+n^2} \ll 1 \\ &\left|\frac{1}{a^2}\int_0^1\int_0^1 W_{mn}(\xi,\eta)W_{m'n'}^{(0)}(\xi,\eta)d\xi d\eta\right| \leq \frac{2\pi^2\epsilon^{3/2}mm'nn'}{|m^2+n^2-m'^2-n'^2|} \ll 1, \qquad \Omega_{mn}^{(0)} \neq \Omega_{m'n'}^{(0)}, \end{aligned} \tag{A.15}$$

assuming $\beta_p/\alpha_p \ll 1$ for $p \in \{m,n,m',n'\}$, or equivalently $\epsilon\pi^2\max\{m,m',n,n'\}^2/2 \ll 1$. We see that these two quantities are much smaller than 1. Therefore, we use $\{W_{mn}^{(0)}(\xi,\eta)\}$ as the approximated solution.

A.2.4 1D Eigensolution in the Small λm Limit

I define a dimensionless parameter $\lambda = \sqrt{2\epsilon} = \sqrt{E'h^2/3\sigma l^2}$. In the limit of small λm, which holds for our membranes and other high-tension resonators [11, 28, 29, 95], Eq. (A.11) becomes

$$\begin{aligned}\alpha_m &= \left(\frac{1}{\epsilon}\right)^{1/2}\left(1+\sqrt{1+2\epsilon\Omega_m^2}\right)^{1/2} \sim \left(\frac{2}{\epsilon}\right)^{1/2} \equiv \frac{2}{\lambda} \\ \beta_m &= \left(\frac{1}{\epsilon}\right)^{1/2}\left(-1+\sqrt{1+2\epsilon\Omega_m^2}\right)^{1/2} \sim m\pi. \end{aligned} \tag{A.16}$$

The beam equations Eqs. (A.8)-(A.10) become (back to coordinate x)

$$u_m(x) = \begin{cases} v_m(x), & 0 \le x \le \frac{l}{2} \\ (-1)^{m+1} v_m(l-x), & \frac{l}{2} < x \le l \end{cases} \tag{A.17}$$

$$v_m(x) = \sqrt{2a}\left\{\sin\left[\frac{m\pi x}{l}\right] + \frac{\lambda m\pi}{2}\left(\exp\left[\frac{-x}{\lambda l/2}\right] - \cos\left[\frac{m\pi x}{l}\right]\right)\right\} \tag{A.18}$$

$$\omega_m \sim \frac{m\pi}{l}\sqrt{\frac{\sigma}{\rho}}. \tag{A.19}$$

A.2.5 Mode Functions of Bilayer Plate

For the fully or near fully metallized plates, we calculate mode functions by using a single-layer plate with a thickness of 100 nm, an effective stress, Young's modulus, mass density, and Poisson's ratio. The effective Young's modulus $E = E_1 = 135$ GPa is the average of the Young's modulus of Si_3N_4 and Al weighted by their thickness. The mass density ρ of Al and Si_3N_4 are very similar, and hence we use an effective mass density of $\rho \sim 2.7$ g/cm^3. We use an effective Poisson's ratio of $\nu = 0.31$.

A.3 Anelastic Loss of a High-Stressed Plate

We place the xy plane at the middle plane of the plate and let the plate oscillate with a small amplitude at an angular frequency ω in the z-direction. The oscillation of plate $We^{i\omega t}$

induces a variation of local bending and overall elongation [11], and thus gives oscillating strains of

$$\tilde{\boldsymbol{\varepsilon}}(t) \equiv \begin{pmatrix} \tilde{\varepsilon}_{xx}(t) \\ \tilde{\varepsilon}_{yy}(t) \\ \tilde{\varepsilon}_{xy}(t) \end{pmatrix} = \underbrace{\begin{pmatrix} -z\frac{\partial^2}{\partial x^2}We^{i\omega t} \\ -z\frac{\partial^2}{\partial y^2}We^{i\omega t} \\ -2z\frac{\partial^2}{\partial x\partial y}We^{i\omega t} \end{pmatrix}}_{\text{local bending}\sim\mathcal{O}(W)} + \underbrace{\begin{pmatrix} \frac{1}{2}\left(\frac{\partial}{\partial x}We^{i\omega t}\right)^2 \\ \frac{1}{2}\left(\frac{\partial}{\partial y}We^{i\omega t}\right)^2 \\ 0 \end{pmatrix}}_{\text{elongation}\sim\mathcal{O}(W^2)} \tag{A.20}$$

$$\approx \begin{pmatrix} -z\frac{\partial^2 W}{\partial x^2} \\ -z\frac{\partial^2 W}{\partial y^2} \\ -2z\frac{\partial^2 W}{\partial x\partial y} \end{pmatrix} e^{i\omega t} \equiv \begin{pmatrix} \varepsilon_{xx} \\ \varepsilon_{yy} \\ \varepsilon_{xy} \end{pmatrix} e^{i\omega t} \equiv \boldsymbol{\varepsilon_0} e^{i\omega t}. \tag{A.21}$$

The strain variation is mostly induced by pure bending, as shown in Eq. (A.20). The accompanying variation of stresses are given by the usual constitutive equation of a classical plate [22] with the complex Young's modulus $\tilde{E} = E_1 + iE_2$:

$$\tilde{\boldsymbol{\sigma}}(t) \equiv \begin{pmatrix} \tilde{\sigma}_{xx}(t) \\ \tilde{\sigma}_{yy}(t) \\ \tilde{\tau_{xy}}(t) \end{pmatrix} = \frac{\tilde{E}}{1-\nu^2} \begin{pmatrix} 1 & \nu & 0 \\ \nu & 1 & 0 \\ 0 & 0 & (1-\nu)/2 \end{pmatrix} \tilde{\boldsymbol{\varepsilon}}(t) \equiv \tilde{E}\mathbf{M}\tilde{\boldsymbol{\varepsilon}}(t). \tag{A.22}$$

Note that the stresses can be separated into in-phase and out-of-phase terms as follows:

$$\begin{aligned} \Re[\tilde{\boldsymbol{\sigma}}(t)] &= \Re[\tilde{E}\mathbf{M}\tilde{\boldsymbol{\varepsilon}}(t)] = \Re[\tilde{E}\mathbf{M}\boldsymbol{\varepsilon_0}e^{i\omega t}] \\ &= \underbrace{E_1\mathbf{M}\boldsymbol{\varepsilon_0}\cos(\omega t)}_{\text{in-phase}} - \underbrace{E_2\mathbf{M}\boldsymbol{\varepsilon_0}\sin(\omega t)}_{\text{out-of-phase}}. \end{aligned} \tag{A.23}$$

The mechanical work done per unit volume per oscillation is then given by

$$\begin{aligned} \Delta w &= \oint \Re[\tilde{\boldsymbol{\sigma}}^{\mathrm{T}}]\Re[\frac{d\tilde{\boldsymbol{\varepsilon}}}{dt}]dt \\ &= \int_0^{\frac{2\pi}{\omega}} \left[E_1\cos(\omega t)\boldsymbol{\varepsilon_0}^{\mathrm{T}}\mathbf{M} - E_2\sin(\omega t)\boldsymbol{\varepsilon_0}^{\mathrm{T}}\mathbf{M}\right]\Re[\boldsymbol{\varepsilon_0}\frac{de^{i\omega t}}{dt}]dt \\ &= \pi E_2\boldsymbol{\varepsilon_0}^T\mathbf{M}\boldsymbol{\varepsilon_0} \geq 0. \end{aligned} \tag{A.24}$$

This leads to dissipation. Meanwhile, the bending energy supplied by the in-phase stresses is stored in the system.

$$u_{\text{bending}} = \int_0^{\pi/2\omega} \Re[\tilde{\boldsymbol{\sigma}}(t)] \cdot \Re[\frac{d\tilde{\boldsymbol{\varepsilon}}}{dt}]dt = E_1 \boldsymbol{\varepsilon_0}^T \mathbf{M} \boldsymbol{\varepsilon_0}/2 = \frac{E_1}{E_2}\frac{\Delta w}{2\pi}. \tag{A.25}$$

Eq. (A.25) is consistent with the strain energy density of a pure bending plate derived in Ref. [23]. We can see that the local dissipation Δw is proportional to the density of stored bending energy. In other words, the bending energy supplied by the out-of-phase stresses is converted irreversibly to heat.

To find the total dissipation per cycle, we integrate Eq. (A.24) over the entire volume of the plate and insert the strain-displacement relations [Eq. (A.20)]. We have

$$\begin{aligned}
\Delta U &= \int \Delta w dV = \int \pi E_2 \boldsymbol{\varepsilon_0}^T \mathbf{M} \boldsymbol{\varepsilon_0}\, dV \\
&= \iiint \frac{\pi E_2(x,y)}{(1-\nu^2)} \Big\{ (\varepsilon_{xx}+\varepsilon_{yy})^2 - 2(1-\nu)(\varepsilon_{xx}\varepsilon_{yy} - \varepsilon_{xy}^2/4) \Big\} dxdydz \qquad \text{(A.26)} \\
&= \int \frac{2\pi E_2(x,y)}{(1+\nu)} \Big\{ \frac{(\varepsilon_{xx}+\varepsilon_{yy})^2}{2(1-\nu)} + \frac{\varepsilon_{xy}^2}{4} - \varepsilon_{xx}\varepsilon_{yy} \Big\} dV \qquad \text{(A.27)} \\
&= \int z^2 dz \iint \frac{\pi E_2(x,y)}{(1-\nu^2)} \Bigg\{ \underbrace{\left(\frac{\partial^2 W}{\partial x^2} + \frac{\partial^2 W}{\partial y^2} \right)^2}_{(\text{mean curvature})^2} - 2(1-\nu) \underbrace{\left[\frac{\partial^2 W}{\partial x^2}\frac{\partial^2 W}{\partial y^2} - \left(\frac{\partial^2 W}{\partial x \partial y} \right)^2 \right]}_{\text{Gaussian curvature}} \Bigg\} dxdy.
\end{aligned} \tag{A.28}$$

The total loss is given by the integration of curvatures over the plate plane.

A.3.1 Stored Energy

In order to evaluate the quality factor $Q = 2\pi U/\Delta U$, we need to calculate the stored energy U and energy loss ΔU. We calculated ΔU above, and here we analyze the stored energy, which can be obtained from the maximum kinetic energy or the maximum elastic energy. The maximum kinetic energy is

$$U_{\text{kinetic}} = \frac{\rho h \omega^2}{2} \iint W(x,y)^2 dxdy = 2\rho\pi^2 f^2 \int W(x,y)^2 dV. \tag{A.29}$$

The maximum elastic energy for a tensioned resonator is the sum of the displacement-induced elongation energy and the bending energy [11]. These two energies are given by

$$U_{\text{elongation}} = \frac{\sigma h}{2} \iint \left\{ \left(\frac{\partial W}{\partial x} \right)^2 + \left(\frac{\partial W}{\partial y} \right)^2 \right\} dxdy \tag{A.30}$$

$$U_{\text{bending}} = \int u_{\text{bending}} dV = \int \frac{E_1}{E_2} \frac{\Delta w}{2\pi} dV. \tag{A.31}$$

A.3.2 Effective Loss Modulus

Using the expressions for U_{mn} and ΔU_{mn} above, and assuming $E_2(x, y)$ is constant over the metallized area, we can evaluate the quality factor or damping rate for each mode with only one unknown quantity E_2. In our data analysis we extract an effective E_2 for the 100 nm bilayer membrane from the data using a least-squares fit, as discussed in the main text. The loss modulus of Al can then be estimated by $E_2(h_{\text{Si}_3\text{N}_4} + h_{\text{Al}})/h_{\text{Al}}$, where $h_{\text{Si}_3\text{N}_4}$ and h_{Al} are the thickness of the Si_3N_4 and the Al, respectively.

A.4 Interpretation

A.4.1 Isotropic Plates

For a plate with uniform thickness and constant E_2, we can simplify Eq. (A.28) using Green's theorem. The integration of Gaussian curvature is zero for a clamped plate (CCCC):

$$\iint \left[\frac{\partial^2 W}{\partial x^2} \frac{\partial^2 W}{\partial y^2} - \left(\frac{\partial^2 W}{\partial x \partial y} \right)^2 \right] dxdy = \oint \frac{\partial^2 W}{\partial y^2} \frac{\partial W}{\partial x} dy - \oint \frac{\partial^2 W}{\partial x \partial y} \frac{\partial W}{\partial x} dx = 0.$$

Thus Eq. (A.28) becomes

$$\Delta U = \frac{\pi E_2 h^3}{12(1-\nu^2)} \iint \left(\frac{\partial^2 W}{\partial x^2} + \frac{\partial^2 W}{\partial y^2} \right)^2 dxdy. \tag{A.32}$$

Note $\partial^2 W/\partial x^2$ is the curvature of the mode in the x direction, and $\partial^2 W/\partial y^2$ is the curvature in the y direction. The sum of the two curvatures is the mean curvature.

A.4.2 Curvature Induced near the Clamped Edge and around the Antinodes

In our anelastic model, the local dissipation of a clamped plate is proportional to the square of the mean curvature, as shown in Eq. (A.32). Hence, it is important to understand its spatial dependence. Since our 2D normal modes are the product of 1D modes, we start by calculating the curvature of a 1D mode u_n. In the limit of $\lambda n \ll 1$, we can approximate the square of the curvature as

$$\left(\frac{d^2u_n(x)}{dx^2}\right)^2 \sim \frac{2n^2\pi^2 a}{l^4}\left(\frac{4}{\lambda^2}\exp\left[\frac{-x}{\lambda l/4}\right] + n^2\pi^2\sin^2\left[\frac{n\pi x}{l}\right]\right), \qquad 0 \le x \le \frac{l}{2}. \tag{A.33}$$

The equation above describes the x dependence of the curvature in the x direction. Note that the coefficient of the first term is much larger than that of the second term. This first exponential term is concentrated in a small range $\lambda l/4 = h\sqrt{E'/48\sigma}$, leading to significant loss near the edge. The second term distributes over the entire length with sinusoidal dependence, just like the curvature of a simply-supported beam.

For the 2D case, in addition to the above-mentioned features, the large curvature induced near the edge oscillates sinusoidally along the plate edge. To see that, we calculate the mean curvature square of the diagonal mode (n, n) at the edge $x = 0$:

$$\left(\frac{\partial^2 W_{nn}}{\partial x^2} + \frac{\partial^2 W_{nn}}{\partial y^2}\right)^2 \Bigg|_{x=0} \sim \frac{16n^2\pi^2a^2}{\lambda^2 l^4}\sin^2\left[\frac{n\pi y}{l}\right]. \tag{A.34}$$

See Fig. A.1 for an illustration of the square of the mean curvature over the entire plate plane.

A.4.3 Edge Loss and the Frequency Dependence of the Quality Factor

To understand the role of loss induced near the clamped edge, here we study Q of a mode (m, n) in the limit of small λn and λm. First, we calculate the maximum kinetic energy. Applying Eq. (A.14) to Eq. (A.29), we have

$$U_{mn} \sim \rho h a^2 l^2(\omega_m^2 + \omega_n^2)/2 \sim \sigma h a^2(m^2 + n^2)\pi^2/2. \tag{A.35}$$

Second, we calculate the loss per cycle drawing on our earlier curvature analysis. Here we use $W_{mn}(x,y) = u_m(x)u_n(y)$. We have verified that the result is the same as using the symmetrized mode functions in Eq. (A.12):

$$
\begin{aligned}
\Delta U_{mn} &= \frac{\pi E_2}{1-\nu^2}\int z^2 dz \iint \left(\frac{\partial^2 W_{mn}}{\partial x^2}+\frac{\partial^2 W_{mn}}{\partial y^2}\right)^2 dxdy \\
&= \frac{\pi E_2 h^3}{12(1-\nu^2)}\iint \left(\frac{d^2u_m(x)}{dx^2}u_n(y)+u_m(x)\frac{d^2u_n(y)}{dy^2}\right)^2 dxdy \\
&= \frac{\pi E_2 h^3}{12(1-\nu^2)}\left\{\int\left(\frac{d^2u_m(x)}{dx^2}\right)^2 dx\int u_n(y)^2dy+\int u_m(x)^2dx\int\left(\frac{d^2u_n(y)}{dy^2}\right)^2 dy\right. \\
&\qquad\left. +2\int\frac{d^2u_m(x)}{dx^2}u_m(x)dx\int\frac{d^2u_n(y)}{dy^2}u_n(y)dy\right\} \\
&= \frac{\pi E_2 h^3}{12(1-\nu^2)}\left\{2al\int_0^{l/2}\left(\frac{d^2u_m(x)}{dx^2}\right)^2 dx+2al\int_0^{l/2}\left(\frac{d^2u_n(y)}{dy^2}\right)^2 dy\right. \\
&\qquad\left. +8\int_0^{l/2}\frac{d^2u_m(x)}{dx^2}u_m(x)dx\int_0^{l/2}\frac{d^2u_n(y)}{dy^2}u_n(y)dy\right\} \\
&\sim \frac{\pi E_2 h^3}{12(1-\nu^2)}\left\{\underbrace{\frac{16m^2\pi^2a^2}{l^3\lambda^2}\int_0^{l/2}\exp\left[\frac{-x}{\lambda l/4}\right]dx+\frac{16n^2\pi^2a^2}{l^3\lambda^2}\int_0^{l/2}\exp\left[\frac{-y}{\lambda l/4}\right]dy}_{\text{“edge loss”}}\right. \\
&\qquad +\underbrace{\frac{4m^4\pi^4a^2}{l^3}\int_0^{l/2}\sin^2\left[\frac{m\pi x}{l}\right]dx+\frac{4n^4\pi^4a^2}{l^3}\int_0^{l/2}\sin^2\left[\frac{n\pi y}{l}\right]dy}_{\text{“antinode loss”}} \\
&\qquad\left. +\underbrace{8\Big(-\frac{2m\pi^2a}{l^2}\int_0^{l/2}\sin^2\left[\frac{m\pi x}{l}\right]dx\Big)\Big(-\frac{2n\pi^2a}{l^2}\int_0^{l/2}\sin^2\left[\frac{n\pi y}{l}\right]dy\Big)}_{\text{“antinode loss”}}\right\} \\
&\sim \frac{\pi E_2 h^3}{12(1-\nu^2)}\left\{\underbrace{\frac{4(m^2+n^2)\pi^2a^2}{l^2\lambda}}_{\text{edge}}+\underbrace{\frac{(m^2+n^2)^2\pi^4a^2}{l^2}}_{\text{antinode}}\right\} \qquad \text{(A.36)} \\
&\sim \frac{(m^2+n^2)\pi^3E_2h^3a^2}{3(1-\nu^2)l^2\lambda}\left\{\underbrace{1}_{\text{edge}}+\underbrace{\lambda\frac{(m^2+n^2)\pi^2}{4}}_{\text{antinode}}\right\}. \qquad \text{(A.37)}
\end{aligned}
$$

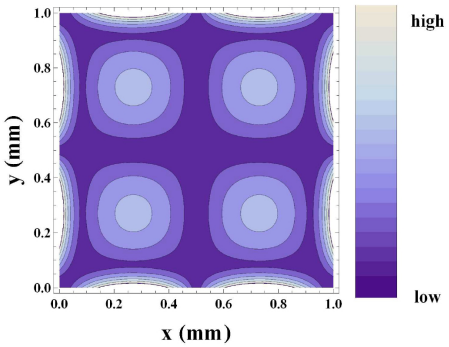

Figure A.1: The spatial dependence of the mean curvature square of the mode $(2, 2)$ over the entire plate plane. A low stress of 0.1 MPa is used, and the values of curvature are scaled nonlinearly to make the structure more visible.

We see that the ratio of the antinode loss to the edge loss is given by $\lambda(m^2 + n^2)\pi^2/4$. Combining Eq. (A.35) and (A.37), we obtain

$$Q_{mn} = \frac{2\pi U_{mn}}{\Delta U_{mn}} \sim \frac{3(1-\nu^2)\sigma l^2 \lambda}{E_2 h^2} \left(1 + \lambda \frac{(m^2+n^2)\pi^2}{4}\right)^{-1} \sim \frac{1}{\lambda}\frac{E_1}{E_2}\left(\underbrace{1}_{\text{edge}} + \underbrace{\lambda \frac{(m^2+n^2)\pi^2}{4}}_{\text{antinode}}\right)^{-1}. \tag{A.38}$$

Similarly, we can derive the formula for a 1D string (with $\nu = 0$)

$$Q_n \sim \frac{1}{\lambda}\frac{E_1}{E_2}\left(1 + \lambda \frac{n^2\pi^2}{4}\right)^{-1}. \tag{A.39}$$

For small λ as low as $10^{-4}-10^{-3}$ in our devices and Ref. [28, 29, 95], Eq. (A.38) and Eq. (A.39) correspond to a slightly decreasing Q as a function of frequency. For $\lambda \sim 2 \times 10^{-2}$ as in Ref. [11], the edge loss and the antinode loss are comparable when $n = 4$. This gives a stronger dependence on n, and hence frequency.

A.4.4 Physical Meaning of λ

To investigate the physical meaning of λ, we calculate the elongation energy of the (m, n) mode in the limit of small λn:

$$\begin{aligned} U_{\text{elongation}} &= \frac{\sigma h}{2} \iint \left\{ \left(\frac{du_m(x)}{dx} \right)^2 u_n(y)^2 + u_m(x)^2 \left(\frac{du_n(y)}{dy} \right)^2 \right\} dxdy \\ &= \sigma hla \left\{ \int_0^{l/2} \left(\frac{dv_m(x)}{dx} \right)^2 dx + \int_0^{l/2} \left(\frac{dv_n(y)}{dy} \right)^2 dy \right\} \\ &\sim \frac{2\pi^2 \sigma h a^2}{l} \left\{ m^2 \int_0^{l/2} \cos^2 \left[\frac{m\pi x}{l} \right] dx + n^2 \int_0^{l/2} \cos^2 \left[\frac{n\pi y}{l} \right] dy \right\} \\ &= \pi^2 \sigma h a^2 (m^2 + n^2)/2 = U_{\text{kinetic}} = U_{\text{elastic}}. \end{aligned} \tag{A.40}$$

This means that the maximum elastic energy is dominated by the elongation energy. Thus,

$$Q_{mn} = \frac{2\pi U_{mn}}{\Delta U_{mn}} \sim \frac{2\pi U_{\text{elongation}}}{2\pi (E_2/E_1) U_{\text{bending}}} = \frac{E_1}{E_2} \frac{U_{\text{elongation}}}{U_{\text{bending}}}. \tag{A.41}$$

Using Eq. (A.38) and Eq. (A.41), we find

$$\begin{aligned} \frac{U_{\text{elongation}}}{U_{\text{bending}}} &= \frac{1}{\lambda} \left(1 + \lambda \frac{(m^2 + n^2)\pi^2}{4} \right)^{-1} \\ &\sim \frac{1}{\lambda}, \quad \text{for} \quad (n, m) = (1, 1). \end{aligned} \tag{A.42}$$

Thus, λ is the ratio of the bending energy to the elongation energy for the fundamental mode.

Appendix B

Calculation of Optical Spectra of the Squeezed Light

In this appendix we describe our solution to the Heisenberg-Langevin equations of motion for our optomechanical system. We then compute the expected output optical quadrature spectrum, and the spectrum obtained from balanced homodyne detection and direct photodetection.

B.0.1 Heisenberg-Langevin Equations

We begin with the following Hamiltonian, $H = H_0 + H_\kappa + H_\Gamma$, where H_0 describes the intracavity coherent dynamics, H_κ represents the coupling of the optical system to external fields, and H_Γ represents the external thermal coupling to the mechanics [86, 63, 64, 5, 96].

$$H_0 = \hbar\omega_m c^\dagger c + \hbar\omega_c a^\dagger a + \hbar G Z_{\rm zp}(c + c^\dagger)a^\dagger a \tag{B.1}$$

where ω_m is the mechanical resonance frequency, c ($c^\dagger$) is the mechanical annihilation (creation) operator, ω_c is the optical resonance frequency, a ($a^\dagger$) is the optical intracavity annihilation (creation) operator, G is the optomechanical coupling constant, and $Z_{\rm zp} = \sqrt{\hbar/2m\omega_m}$ is the mechanical zero point motion, with m the mechanical resonator effective mass. We define a single photon optomechanical coupling rate $g = GZ_{\rm zp}$, and a dimensionless mechanical displacement operator $z = \left(c + c^\dagger\right) - \langle c + c^\dagger\rangle$. The Hamiltonian is linearized by assuming a large optical coherent state amplitude compared to the vacuum level, $a = (\bar{a} + d(t))e^{i\omega_L t}$, where ω_L is the optical drive frequency, $\bar{a} = \langle a\rangle$ is the intracavity coherent state amplitude,

assumed to be real, and $d(t)$ is an operator containing the quantum and classical noise on the optical field. Terms of order d^2 are neglected. The linearized Hamiltonian that encapsulates the basic interaction is

$$\begin{aligned} H_0 =& \hbar\omega_m c^\dagger c + \hbar\omega_c a^\dagger a + \\ & \hbar G Z_{\rm zp}(c + c^\dagger)\bar{a}^*\bar{a} + H_{BS} + H_{TMS} \end{aligned} \tag{B.2}$$

$$H_{BS} = \hbar G Z_{\rm zp}\left(\bar{a}^* c^\dagger d + \bar{a} c d^\dagger\right) \tag{B.3}$$

$$H_{TMS} = \hbar G Z_{\rm zp}\left(\bar{a}^* c d + \bar{a} c^\dagger d^\dagger\right) \tag{B.4}$$

The resulting linearized Hamiltonian contains both the beam-splitter (H_{BS}) and the two mode squeezing (H_{TMS}) Hamiltonians.

We solve the Heisenberg-Langevin equations of motion for this system in the frequency domain, using the Fourier transformation convention $f(\omega) \equiv \int_{-\infty}^{\infty} e^{\imath\omega t} f(t) dt$, $f^\dagger(\omega) \equiv \int_{-\infty}^{\infty} e^{\imath\omega t} f^\dagger(t) dt$, $\left(f^\dagger(\omega)\right)^\dagger = f(-\omega)$. We assume thermally driven mechanical motion, with mechanical damping rate Γ_0 and initial thermal occupation $n_{\rm th}$. We include the effects of the additional optical damping beam in an orthogonal cavity mode, by defining effective values for ω_m, Γ_0, and $n_{\rm th}$ for the motion of the mechanical resonator in the presence of the optomechanical damping, spring, and cooling induced by the damping beam [86]. The optomechanical effects of the signal beam are intrinsic in the equations of motion. The optical loss rate to the input port, output port, and internal loss are κ_L, κ_R, and $\kappa_{\rm int}$ respectively, yielding a total cavity damping rate of $\kappa = \kappa_L + \kappa_R + \kappa_{\rm int}$. The external optical input fields consist of a coherent state, of frequency ω_L, incident on the input port of the two-sided Fabry-Perot cavity, and vacuum incident on the output port. An effective detuning of the input signal field from the average value of the optomechanically shifted cavity resonance is given by Δ. The optical output operator, $a_{\rm out} = (\bar{a}_{\rm out} + d_{\rm out}(t))e^{i\omega_L t}$, is computed using the cavity input-output relations $\bar{a}_{\rm out} = \sqrt{\kappa_R}\bar{a}$, $d_{\rm out} + d_{\rm in} = \sqrt{\kappa_R} d$, where $d_{\rm in}$ is the noise operator representing the vacuum field incident on the output port [97].

B.0.2 Optical Output Spectrum

The quadrature output operator is defined as $X_\phi(\omega) = a_{\text{out}}(\omega)e^{i\phi} + a^\dagger_{\text{out}}(\omega)e^{-i\phi}$, where ϕ is the quadrature phase angle. Because we have assumed $\bar{a}$ to be real, the input-output relation indicate $\bar{a}_{\text{out}}$ is also real, and $\phi = 0$ ($\phi = 90$) corresponds to the amplitude (phase) quadrature. The symmetrized power spectrum of the quadrature operator is $S_{XX}(\omega)$.

$$\begin{aligned} S_{XX}(\omega) =& \langle X_\phi(-\omega)X_\phi(\omega)\rangle_s \\ =& \frac{1}{2}\left(\langle X_\phi(-\omega)X_\phi(\omega)\rangle + \langle X_\phi(\omega)X_\phi(-\omega)\rangle\right) \\ =& A_{\zeta\zeta}(\omega) + A_{zz}(\omega) + A_{\zeta z}(\omega) \end{aligned} \tag{B.5}$$

The spectrum consist of three terms. $A_{\zeta\zeta}$ is the shot noise on the output. A_{zz} represents the noise imprinted by the actual mechanical motion. The cross term $A_{\zeta z}$ contains the correlations between shot noise and motion driven by radiation pressure from the shot noise. This term is responsible for any squeezing.

$$A_{zz}(\omega) = \kappa_R|\bar{a}|^2 g^2\Big(|\chi_c(\omega)|^2 + |\chi_c(-\omega)|^2 - \chi_c(\omega)\chi_c(-\omega)e^{2i\phi} - \chi_c^*(\omega)\chi_c^*(-\omega)e^{-2i\phi}\Big)\langle z(-\omega)z(\omega)\rangle_s$$

$$\begin{aligned} A_{\zeta z}(\omega) = i\sqrt{\kappa_R}\bar{a}g\Big(&(-\chi_c(-\omega)e^{2i\phi} + \chi_c^*(\omega))\langle z(-\omega)\zeta(\omega)\rangle_s + (-\chi_c(\omega)e^{2i\phi} + \chi_c^*(-\omega))\langle \zeta(-\omega)z(\omega)\rangle_s + \\ &(\chi_c^*(\omega)e^{-2i\phi} - \chi_c(-\omega))\langle z(-\omega)\zeta^\dagger(\omega)\rangle_s + (\chi_c^*(-\omega)e^{-2i\phi} - \chi_c(\omega))\langle \zeta^\dagger(-\omega)z(\omega)\rangle_s\Big) \end{aligned}$$

$$A_{\zeta\zeta}(\omega) = \langle \zeta^\dagger(-\omega)\zeta(\omega)\rangle_s + \langle \zeta(-\omega)\zeta^\dagger(\omega)\rangle_s = 1$$

The output shot noise operator is $\zeta(\omega) = \chi_c(\omega)\sqrt{\kappa_L\kappa_R}\xi_L(\omega) + \chi_c(\omega)\sqrt{\kappa_{\text{int}}\kappa_R}\xi_{\text{int}}(\omega) + (\chi_c(\omega)\kappa_R - 1)\xi_R(\omega)$. ξ_L, ξ_R, and ξ_{int} are the Langevin vacuum noise operators for the input port, output port, and internal loss of the cavity respectively.

$$\langle z(-\omega)z(\omega)\rangle_s = \frac{1}{|\mathcal{N}(\omega)|^2}\left(\Gamma_0\left(\frac{n_{\text{th}} + 1/2}{|\chi_m(\omega)|^2} + \frac{n_{\text{th}} + 1/2}{|\chi_m(-\omega)|^2}\right) + 2\omega_m^2 g^2\kappa|\bar{a}|^2\left(|\chi_c(\omega)|^2 + |\chi_c(-\omega)|^2\right)\right)$$

$$\langle z(-\omega)\zeta(\omega)\rangle_s = \frac{-\omega_m\bar{a}g\sqrt{\kappa_R}}{\mathcal{N}(-\omega)}\chi_c(\omega); \qquad \langle \zeta(-\omega)z(\omega)\rangle_s = \frac{-\omega_m\bar{a}g\sqrt{\kappa_R}}{\mathcal{N}(\omega)}\chi_c(-\omega)$$

$$\langle \zeta^\dagger(-\omega)\zeta(\omega)\rangle_s = \langle \zeta(-\omega)\zeta^\dagger(\omega)\rangle_s = \frac{1}{2}$$

We have introduced the following notation. The cavity susceptibility is $\chi_c(\omega) = (\kappa/2 - i(\Delta+\omega))^{-1}$. The mechanical susceptibility is $\chi_m(\omega) = (\Gamma_0/2 - i(\omega-\omega_m))^{-1}$. The optomechanical damping and spring effects are encompassed in $\mathcal{N}(\omega) = (\chi_m(\omega)\chi_m^*(-\omega))^{-1} - i2\omega_m g^2|\bar{a}|^2(\chi_c(\omega) - \chi_c^*(-\omega))$. We also assume the mechanical thermal and optical vacuum baths are uncorrelated at different times $\langle \xi(-\omega')\xi(\omega)\rangle = \delta(\omega-\omega')$, for noise operator ξ, and we assume integration over ω' for physically relevant quantities.

Any loss in the optical detection system, including propagation losses between the cavity and detector, imperfect mode matching to the homodyne detector, or finite photodetector conversion efficiency can be modeled by a single effective loss port with fractional loss ϵ_{ext}. The loss port attenuates the signal reaching the detector $\bar{a}_{\text{out}} \to \sqrt{\epsilon_{\text{ext}}}\bar{a}_{\text{out}}$, and injects vacuum noise leading an effective quadrature spectrum of $S_{XX}(\omega) \to \epsilon_{\text{ext}}S_{XX}(\omega) + (1-\epsilon_{\text{ext}})$.

The homodyne detection consists of combining a strong optical local oscillator with the output from the cavity on a beam splitter. Both outputs of the beam splitter are recorded on photodetectors and the two photocurrents are subtracted. Assuming an equal splitting on the beam splitter, the subtracted photocurrent signal is proportional to $(\bar{a}_{\text{out}}\bar{a}_{\text{LO}}e^{i\phi} - \bar{a}_{\text{out}}\bar{a}_{\text{LO}}e^{-i\phi}) + \bar{a}_{\text{out}}(d_{\text{LO}} + d_{\text{LO}}^\dagger) + \bar{a}_{\text{LO}}(d_{\text{out}}e^{i\phi} + d_{\text{out}}^\dagger e^{-i\phi})$, where the annihilation operator of the local oscillator is $a_{\text{LO}} = (\bar{a}_{\text{LO}} + d_{\text{LO}}(t))e^{i\omega_L t+\phi}$, and we have neglected terms of order d^2. The third terms is proportional to X_ϕ. The second term which represents the local oscillator vacuum noise beating against the coherent portion of the cavity output field is negligible when $\bar{a}_{\text{LO}} \gg \bar{a}_{\text{out}}$, and is typically ignored. However, in the homodyne detection system described in the main text, we are limited to a local oscillator power which is less than 10 times larger than the signal beam power in order to ensure the photodetectors to remain in their linear range. In this case, the local oscillator noise term must be included to quantitatively model the homodyne data. The one-sided, symmetrized, shot noise normalized spectra, $S_\phi(\omega)$ in

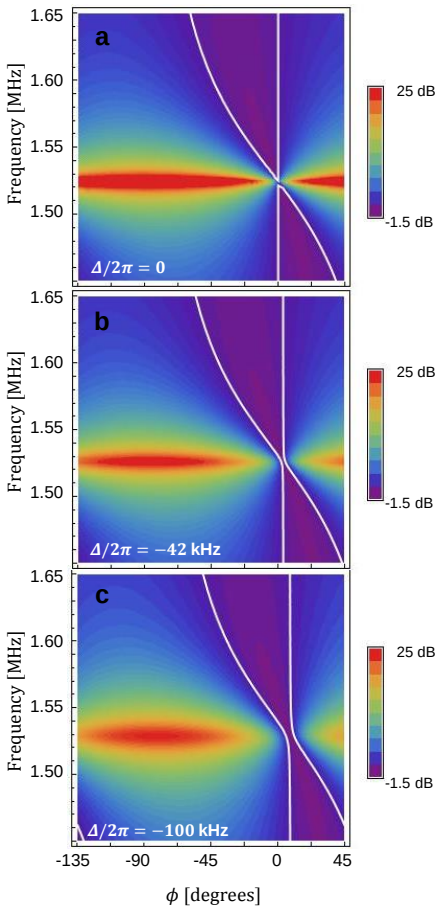

Figure B.1: Calculated Homodyne Spectrum for finite signal beam detuning. Homodyne transmission spectra, S_ϕ, are calculated for three signal beam-cavity detunings: (a) $\Delta/2\pi = 0$, (b) $\Delta/2\pi = -42$ kHz, (c) $\Delta/2\pi = -100$ kHz. The other parameters used are $g/2\pi = 33$ Hz, $m = 6.75 \times 10^{-12}$ kg, $\omega_m^{\rm eff}/2\pi = 1.5243$ MHz, $\Gamma_0^{\rm eff}/2\pi = 2560$ Hz, $T^{\rm eff} = 3.8 \times 10^{-4}$ K, $\epsilon_{\rm ext} = 0.55$, $\kappa/2\pi = 1.7$ MHz, $\kappa_R = 0.6\kappa$, $\bar{N} = 1.1 \times 10^8$, $\epsilon_{\rm ext}|\bar{a}_{\rm out}|^2/|\bar{a}_{\rm LO}|^2 = 0.1$. The parameters of panel (b) match the parameters of the measured spectrum presented in Fig. 5.8. With those parameters, the mechanical damping from the signal beam is 6 kHz. Calculated spectra are displayed on a logarithmic scale. The region between the white 0 dB contours is squeezed.

the main text are then given by:

$$S_\phi(\omega) = \frac{2\left(|\bar{a}_{\rm LO}|^2(\epsilon_{\rm ext}S_{XX}(\omega) + (1-\epsilon_{\rm ext})) + \epsilon_{\rm ext}|\bar{a}_{\rm out}|^2\right)}{2\left(|\bar{a}_{\rm LO}|^2 + \epsilon_{\rm ext}|\bar{a}_{\rm out}|^2\right)} \tag{B.6}$$

Using this full expression, one sees the level of perceived squeezing is reduced by the additional uncorrelated noise floor of the local oscillator.

The one-sided, symmetrized, shot-noise-normalized, direct photodetection spectrum,

discussed in the main text requires $S_{XX}(\omega)$ to be evaluated at $\phi = 0$.

$$S_I(\omega) = \epsilon_{\text{ext}} S_{XX}(\omega)|_{\phi=0} + (1 - \epsilon_{\text{ext}}) \tag{B.7}$$

Appendix C

Laser Classical Noise Measurement

Laser noise has two different origins: quantum noise and classical noise. The laser quantum noise is fundamental; it is a consequence of the Heisenberg Uncertainty Principle. It cannot be eliminated by any technical trick. The laser classical noise is technical; it is arising, for example, from excess noise of the pump source or from vibrations of the laser resonator. It can be reduced by methods such as passing the laser beam through a filter cavity or employing a difference detection scheme.

Many quantum optomechanics experiments concerns the study of optomechanical effects from quantum shot noise of the laser. The radiation pressure of the quantum fluctuations produces many interesting quantum phenomena such as optomechanically squeezed light described in Chapter 5, sideband asymmetry and ratio thermometry described in Chapter 6, quantum measurement backaction, and quantum backaction limit of optomechanical sideband cooling. However, the amplitude fluctuation and phase fluctuation from the laser classical noise, could produce similar optomechanical effects as well. To isolate interesting quantum effects from the these classical noise effects, we need to minimize the laser classical noise. My goal in this appendix is to provide methods and theories for detecting the laser classical noise, and summarize the measurements of classical noise in Chapter 6 and recent experiments in our lab.

I first present the methods for detecting the laser classical noise. For each method, I provide a simple description, mathematical formulation, and the formula for the detected

spectrum. In the end, I summarize the measurements of classical laser noise in the labs B236 and X1B40 in the year of 2014. The measurements are done by me and Bob, respectively. The optical setup in the lab B236 did the sideband asymmetry thermometry measurements, while that in the lab X1B40 did the measurement of quantum backaction limit of laser cooling. For each measurement, I show the data and specify the detection method. Then I describe the data analysis for extracting the values of the laser classical noise. The extracted numbers are summarized in Table C.1.

C.1 Mathematical Description of the Laser Noise

In this section, I provide the mathematical description of the laser noise and define the measurable quantity that represent the size of the laser classical noise. The optical field with laser noise can be described by [90]:

$$\hat{a}(t) = \left(\bar{a} + \hat{\xi}_l(t) + \frac{1}{2}(\delta x(t) + i\delta y(t))\right) e^{i\omega_l t}, \tag{C.1}$$

where $\hat{a}(t)$ is the quantized complex amplitude of the laser electric field, $\bar{a} = \sqrt{P/\hbar\omega_l}$, P is the total laser power, ω_l is the laser frequency, $\hat{\xi}_l(t)$ is the vacuum noise operator in which

$$\begin{aligned} \langle\hat{\xi}(t)\hat{\xi}^\dagger(t')\rangle &= \delta(t-t') \\ \langle\hat{\xi}^\dagger(t)\hat{\xi}(t')\rangle &= 0. \end{aligned} \tag{C.2}$$

$\langle\hat{\xi}(t)\hat{\xi}^\dagger(t')\rangle = \delta(t-t')$ and $\langle\hat{\xi}^\dagger(t)\hat{\xi}(t')\rangle = 0$. $\delta x(t)$ and $\delta y(t)$ are classical laser amplitude and frequency noise variables, respectively. Since we are only concerned with noise near the mechanical frequency, a white noise model can be used:

$$\begin{aligned} \langle\delta x(t)\delta x(t')\rangle &\equiv C_{xx}\delta(t-t') \\ \langle\delta y(t)\delta y(t')\rangle &\equiv C_{yy}\delta(t-t') \\ \langle\delta x(t)\delta y(t')\rangle &\equiv C_{xy}\delta(t-t'), \end{aligned} \tag{C.3}$$

where $C_{xx}, C_{yy} \geq 0$ and C_{xy} are real numbers. C_{xy} is bounded by $C_{xy}^2 \leq C_{xx}C_{yy}$, as dictated by the Cauchy-Bunyakovsky-Schwarz inequality. They represent the laser amplitude and frequency noise. We assume they are proportional to laser power.

C.2 Classical Amplitude Noise Measurement

In this section, we describe two nearly-calibration-free methods to measure the classical amplitude noise.

The key to measure C_{xx} is to measure the intensity noise spectrum and the shot noise spectrum. The first spectrum has both the classical amplitude noise and the shot noise, while the second spectrum has only the shot noise. By dividing the two spectra, we can extract C_{xx}. The only requirement is the quantum efficiency of the photodiode.

The first method we employ is a balanced detection (Fig. C.1). The laser beam is divided into two beams of equal power with a beam splitter and detected by two identical photodiodes. The photo-currents on the two photodiodes are added or subtracted electronically. The power spectral density of the added (subtracted) signal, called the sum (difference) spectrum, is calculated from a digitalized signal with a computer. Several thousand spectra are averaged to reduce the statistical fluctuation. The sum spectrum is the intensity noise spectrum and the difference spectrum is the shot noise spectrum.

Alternatively, one could use a direct detection that only requires a single photodiode and no electronics. That is, one directly shine the laser beam or a flashlight on a photodiode and calculate the power spectral density of the photocurrent. In this case, the laser spectrum has both the classical laser noise and the shot noise, while the flashlight spectrum has only the shot noise. If the power of the laser beam and the flashlight are the same, by dividing the laser spectrum with the flashlight spectrum we can extract C_{xx}. The drawback is that the flashlight power can not be stabilized and may decrease during the measurement as the voltage of the battery decays.

We note that we can also mix the two methods. For example, we can measure the

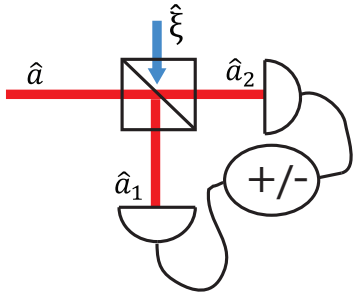

Figure C.1: Optical Setup for balanced detection.

intensity noise spectrum with the direct detection and the shot noise spectrum with the balanced detection. We can use this method if we don't have the electronics to do the sum but can do the difference of the photocurrents.

C.2.1 Mathematical Description of the Direct Detection

Here we calculate the power spectral density in the direct detection. We first calculate the photocurrents on the diodes, and then calculate their auto-correlation functions. The spectrum is calculated by performing Fourier transform to the auto-correlation functions.

We start with a mode described by $\hat{a}(t) = \left(\bar{a} + \hat{\xi}_l(t) + \frac{1}{2}(\delta x(t) + i\delta y(t))\right) e^{i\omega_l t}$. The mode experienced by the photodiode is attenuated and added by a new vacuum noise because of the finite quantum efficiency σ_p of the photodiode:

$$\begin{pmatrix} \hat{A}(t) \\ \text{loss} \end{pmatrix} = \begin{pmatrix} \sqrt{\sigma_p} & i\sqrt{1-\sigma_p} \\ i\sqrt{1-\sigma_p} & \sqrt{\sigma_p} \end{pmatrix} \begin{pmatrix} \hat{a}(t) \\ \hat{\xi}(t) \end{pmatrix} \tag{C.4}$$

Let the gain of the photodetector be G. The photocurrent is given by

$$\begin{aligned} \hat{I}(t) = G[\hat{A}(t)]^\dagger \hat{A}(t) &= G\bar{a}^2\sigma_p + G\bar{a}\sigma_p\delta x(t) + G\bar{a}\sqrt{\sigma_p}\left(\sqrt{\sigma_p}\hat{\xi}_l(t) + i\sqrt{1-\sigma_p}\hat{\xi}(t) + h.c.\right) \\ &\equiv G\bar{a}^2\sigma_p + G\bar{a}\sigma_p\delta x(t) + G\bar{a}\sqrt{\sigma_p}\left(\hat{\xi}_s(t) + \hat{\xi_s}^\dagger(t)\right), \end{aligned} \tag{C.5}$$

where $\hat{\xi}_s(t) \equiv \sqrt{\sigma_p}\hat{\xi}_l(t) + i\sqrt{1-\sigma_p}\hat{\xi}(t)$ is the incoherent sum of the vacuum operators. Note that because $\hat{\xi}_s(t)$ and $\hat{\xi}(t)$ are not correlated, $\hat{\xi}_s(t)$ still obeys Eq. (C.2). We next calculate

the auto-correlation:

$$R(t') = \langle \hat{I}(t)\hat{I}(t+t')\rangle = G^2\bar{a}^4\sigma_p^2 + G^2\bar{a}^2\sigma_p^2 C_{xx}\delta(t') + G^2\bar{a}^2\sigma_p\delta(t') \tag{C.6}$$

The single-sided power spectral density is then:

$$S(\omega) = 2S_{II}(\omega) = 2\int_{-\infty}^{\infty} R(t')e^{-i\omega t'}dt' = 2G^2\bar{a}^2\sigma_p(1+\sigma_p C_{xx}) \tag{C.7}$$

For the flashlight we expect $C_{xx} = 0$. Therefore for the same light power (same voltage on the photodetector)

$$S_{\text{laser}}(\omega)/S_{\text{flashlight}}(\omega) = 1 + \sigma_p C_{xx}. \tag{C.8}$$

C.2.2 Mathematical Description of the Balanced Detection

Here we calculate the sum and the difference spectrum in the balanced detection.

Again we start with an input laser mode $\hat{a}(t)$. The two beams on the two photodiodes, $\hat{a_1}(t)$ and $\hat{a_2}(t)$, can be expressed as follows:

$$\begin{pmatrix} \hat{a_1}(t) \\ \hat{a_2}(t) \end{pmatrix} = \begin{pmatrix} \frac{1}{\sqrt{2}} & \frac{i}{\sqrt{2}} \\ \frac{i}{\sqrt{2}} & \frac{1}{\sqrt{2}} \end{pmatrix} \begin{pmatrix} \hat{a}(t) \\ \hat{\xi}(t) \end{pmatrix}. \tag{C.9}$$

The modified modes due to the finite quantum efficiency σ_p of the photodiode are $\hat{A}_1(t)$ and $\hat{A}_2(t)$. The sum and the difference current are

$$\begin{aligned} \hat{I}_{\text{sum}}(t) &= \hat{I}_1(t) + \hat{I}_2(t) = G[\hat{A}_1(t)]^\dagger\hat{A}_1(t) + G[\hat{A}_2(t)]^\dagger\hat{A}_2(t) \\ &= G\bar{a}^2\sigma_p + G\bar{a}\sigma_p\delta x(t) + G\bar{a}\sqrt{\sigma_p}\left(\hat{\xi_s}(t) + \hat{\xi_s}^\dagger(t)\right) \qquad \text{(C.10)} \\ \hat{I}_{\text{diff}}(t) &= \hat{I}_2(t) - \hat{I}_1(t) = G[\hat{A}_2(t)]^\dagger\hat{A}_2(t) - G[\hat{A}_1(t)]^\dagger\hat{A}_1(t) \\ &= G\bar{a}\sqrt{\sigma_p}\left(\hat{\xi_d}(t) + \hat{\xi_d}^\dagger(t)\right). \qquad \text{(C.11)} \end{aligned}$$

Here we rewrite the vacuum noise terms as $\hat{\xi_s}$ and $\hat{\xi_d}$. They both obey Eq. C.2. The one-sided

power spectral densities are therefore

$$S_{\text{sum}}(\omega) = 2\int_{-\infty}^{\infty} \langle \hat{I}_{\text{sum}}(t)\hat{I}_{\text{sum}}(t+t')\rangle e^{-i\omega t'} dt' = 2G^2\bar{a}^2\sigma_p(1+\sigma_p C_{xx}) \tag{C.12}$$

$$S_{\text{diff}}(\omega) = 2\int_{-\infty}^{\infty} \langle \hat{I}_{\text{diff}}(t)\hat{I}_{\text{diff}}(t+t')\rangle e^{-i\omega t'} dt' = 2G^2\bar{a}^2\sigma_p. \tag{C.13}$$

We can extract the C_{xx} via

$$S_{\text{sum}}(\omega)/S_{\text{diff}}(\omega) = 1 + \sigma_p C_{xx}. \tag{C.14}$$

C.3 Classical Frequency Noise Measurement

In this section, I describe the detection method for measuring classical frequency noise. Similar to the measurement of classical amplitude noise, we want a measurement scheme that, ideally, only detects the classical frequency noise and the shot noise. And we divide the spectrum by the shot-noise-only spectrum to extract C_{yy}.

Here we employ a delayed-line technique (Fig. C.2). The delayed-line converts frequency fluctuations of a beam to frequency-dependent phase fluctuations. These phase fluctuations are sensed by the heterodyne or the homodyne detection. The optical setup (Fig. C.2) starts with a laser beam that splits into a signal beam and a strong local oscillator (LO). The signal beam passes through a 8 m fiber that provides a time delay τ of approximately $\sim$ 50 ns. To perform heterodyne detection, we shift the frequency of the LO by $\omega_{\text{LO}} = 17$ MHz via an AOM. The signal beam and the LO are then recombined, co-propagated, and split equally to make a balanced detection. The difference spectrum of the photo-currents is then measured.

The shot noise spectrum can be measured with a balanced detection. We can easily have that by blocking the light on the arm with a delayed line. Note that we can also employ homodyne detection. In that case, we do not need an AOM to shift the LO frequency.

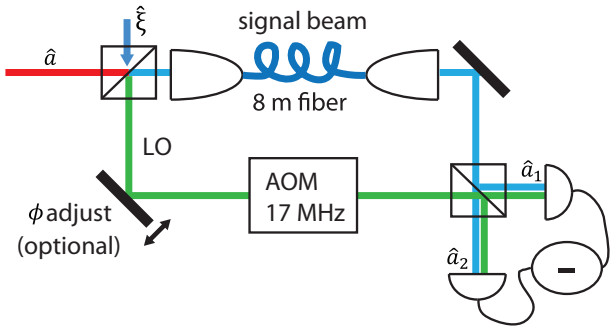

Figure C.2: Setup for measuring laser classical frequency noise. The beam to be measured is split into a signal beam and a local oscillator (LO). The signal beam passes a 8 m fiber so that it is delayed by approximately 50 ns compared with the LO. Then the two beams are recombined and split equally to make a balanced heterodyne detection.

C.3.1 Mathematical Description of the Delayed-Line Heterodyne (Homodyne) with Balanced Detection

The optical modes which shine on the two photodiodes, $\hat{a_1}(t)$ and $\hat{a_2}(t)$, can be described by

$$\begin{pmatrix} \hat{a_1}(t) \\ \hat{a_2}(t) \end{pmatrix} = \begin{pmatrix} \frac{1}{\sqrt{2}} & \frac{i}{\sqrt{2}} \\ \frac{i}{\sqrt{2}} & \frac{1}{\sqrt{2}} \end{pmatrix} \begin{pmatrix} e^{i\omega_{\mathrm{LO}}t} & 0 \\ 0 & e^{i\phi(t)}e^{-i\omega\tau}\hat{T}(-\tau) \end{pmatrix} \begin{pmatrix} \alpha & i\beta \\ i\beta & \alpha \end{pmatrix} \begin{pmatrix} \hat{a}(t) \\ \hat{\xi}(t) \end{pmatrix}, \tag{C.15}$$

where $\hat{T}(-\tau)$ is the time-delay operator. For any function $g(t)$, $\hat{T}(-\tau)g(t) = g(t-\tau)$. α^2 (β^2) is the ratio of the signal beam (LO) power to the total power, $\alpha^2 + \beta^2 = 1$, and $\phi(t)$ is the relative phase fluctuation between the two arms (derived from fluctuations of the fiber length, mirror position, etc.). Note that the formula describes both heterodyne ($\omega_{LO} \neq 0$) and homodyne ($\omega_{LO} = 0$).

Following the same procedures in the previous section, we calculate the difference spectrum for the case of homodyne and heterodyne separately.

C.3.2 Heterodyne

In this section we derive the formula without locking the phase. Without the phase lock, we should calculate the phase-averaged, one-sided spectrum $\bar{S}_{\mathrm{diff}}(\omega) = \frac{1}{2\pi}\int_0^{2\pi} S_{\mathrm{diff}}(\omega)d\phi$:

$$2G^2\bar{a}^2\sigma + 2\alpha^2\beta^2G^2\bar{a}^2\sigma^2\Big\{C_{xx}(1+\cos[\omega\tau]\cos[\omega_{\mathrm{LO}}\tau])+ \\ C_{yy}(1-\cos[\omega\tau]\cos[\omega_{\mathrm{LO}}\tau])+2C_{xy}\cos[\omega\tau]\sin[\omega_{\mathrm{LO}}\tau]\Big\}, \tag{C.16}$$

where $\sigma = \sigma_p\epsilon^2$ is the total quantum efficiency, and ϵ is the visibility of the interferometer. The ratio of the difference spectrum to the shot noise spectrum under the same laser power

is then

$$r = 1 + \alpha^2\beta^2\sigma\Big\{C_{xx}(1 + \cos[\omega\tau]\cos[\omega_{\rm LO}\tau]) + \tag{C.17}$$

$$C_{yy}(1 - \cos[\omega\tau]\cos[\omega_{\rm LO}\tau]) - 2C_{xy}\cos[\omega\tau]\sin[\omega_{\rm LO}\tau]\Big\} \tag{C.18}$$

$$= 1 + \alpha^2\beta^2\sigma(C_{xx} + C_{yy}) + \cos[\omega\tau]\alpha^2\beta^2\sigma\Big\{(C_{xx} - C_{yy})\cos[\omega_{\rm LO}\tau] - 2C_{xy}\sin[\omega_{\rm LO}\tau]\Big\}. \tag{C.19}$$

The function r has a constant offset plus an oscillating term with the frequency period $2\pi/\tau$. From the constant offset one can measure $C_{xx} + C_{yy}$. To measure C_{xx}, C_{yy}, and C_{xy} separately, in principle one can set ω_{LO} such that $\sin[\omega_{LO}] = 1$ or $\sin[\omega_{LO}] = 0$. However, this is hard to do in our case because we need 30 MHz to rotate $\pi/2$ in phase, and the detection bandwidth is only about 20 MHz. The ideal length of delayed line is > 100 m so that the we only need < 3 MHz.

We note that given the same laser power, the signal is maximized when the power of the signal beam and the LO are equal, $\alpha^2 = \beta^2 = 1/2$. This is also true for the homodyne delay line (see below for the formula).

C.3.3 Homodyne

The difference spectrum with phase ϕ between the LO and the signal beam can be expressed as

$$S_\phi(\omega) = 2G^2\bar{a}^2\sigma + 8\alpha^2\beta^2G^2\bar{a}^2\sigma^2\left(C_{xx}\cos^2[\frac{\omega\tau}{2}]\cos^2[\phi] + C_{yy}\sin^2[\frac{\omega\tau}{2}]\sin^2[\phi]\right). \tag{C.20}$$

We can lock the phase at the FM quadrature $\phi = \pi/2$:

$$S_\phi(\omega) = 2G^2\bar{a}^2\sigma + 8\alpha^2\beta^2G^2\bar{a}^2\sigma^2C_{yy}\sin^2[\frac{\omega\tau}{2}]. \tag{C.21}$$

The ratio of the difference spectrum to the shot noise spectrum is therefore

$$r = 1 + 4\alpha^2\beta^2\sigma C_{yy}\sin^2[\frac{\omega\tau}{2}]. \tag{C.22}$$

This technique gives a pure frequency noise measurement if we have the locking capability.

C.4 Data and Analysis

In this section, we summarize the measurements of classical laser noise in the labs B236 and X1B40 in the year of 2014. The optical setup in the lab B236 did the sideband asymmetry thermometry measurements, while that in the lab X1B40 did the measurement of quantum backaction limit of laser cooling. We summarize the method, data, and extracted classical noise values (Table C.1).

C.4.1 Classical amplitude noise C_{xx} measurement

For B236, we employ the balanced detection discussed in section C.2. The data is shown in Fig. C.3 (a) and (b). Using Eq. C.14, we find $C_{xx} < 0.01$ at 25 μW. For X1B40, we use the direct detection discussed in section C.2. The data is shown in Fig.C.3 (c) and (d). Using Eq. C.8, we extract $C_{xx} < 0.004$ at 10 μW.

C.4.2 Classical frequency noise C_{yy} measurement

For B236, we employ the heterodyne delayed-line technique with the balanced detection discussed in section C.3. We measure the ratio of the difference spectrum and the shot noise spectrum. The data is shown in Fig. C.4(a). The spectrum of the data is flat over the 6 MHz frequency range. Comparing with Eq. C.19, the flatness of the spectrum indicates that the oscillation term is small compared with the constant term, $C_{xx} + C_{yy}$. From this constant term, we find that $C_{yy} < C_{xx} + C_{yy} < 0.02$ at 25 μW.

For X1B40, we employ the homodyne delayed-line technique with the balanced detection discussed in section C.3. We data of the ratio of the difference spectrum and the shot noise spectrum is shown in Fig.C.4(b). We see a peak around 6 MHz. Assuming the classical noise is white, this peak corresponds to $\sin^2[\frac{\omega\tau}{2}] = 1$ in Eq. C.22. From the magnitude of the peak, we estimate that $C_{yy} < 0.04$ at 10 μW.

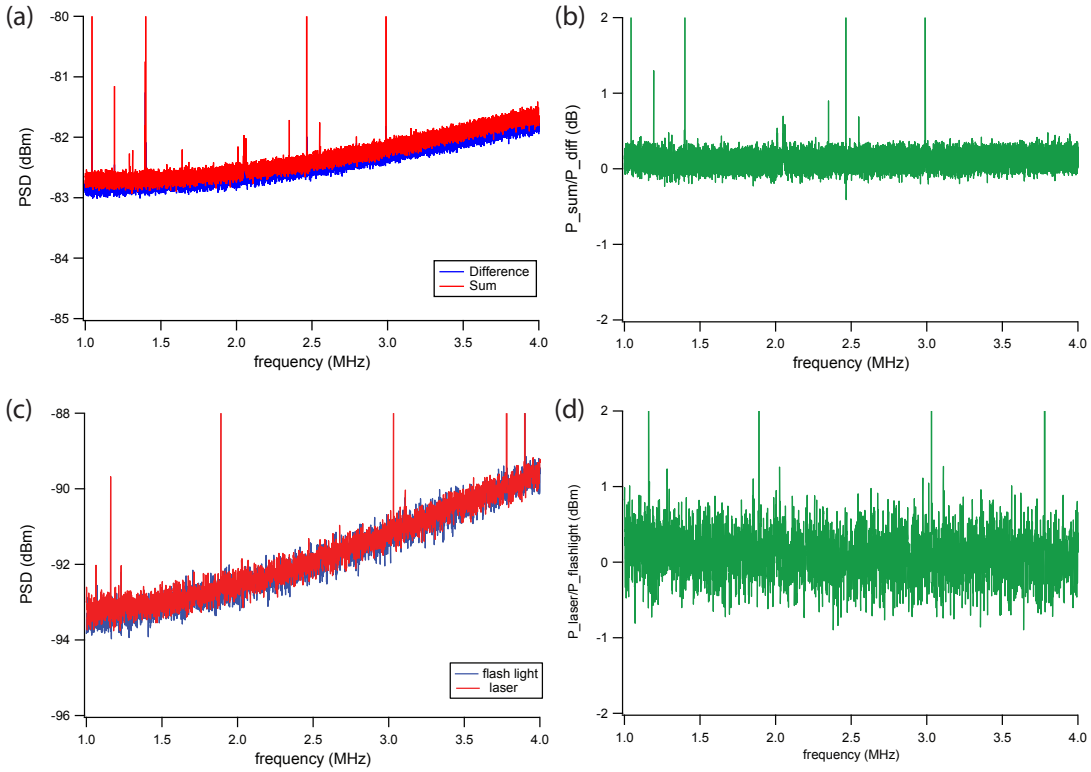

Figure C.3: Measurements of classical amplitude noise C_{xx}. (a) and (b) show the data of laser beam with a power of 25 μW in B236 via the balanced detection. (c) and (d) show the data of the laser beam in X1B40 with the direct detection. (a) The sum and difference spectrum. (b) The ratio of the sum and difference spectrum. (c) The laser and flash light spectrum. (d) The ratio of the laser and flash light spectrum.

C.4.2.1 C_{xy} estimation

We estimate the upper bound of C_{xy} using our knowledge of C_{xx} and C_{yy} and Cauchy-Bunyakovsky-Schwarz inequality.

Table C.1: Measured classical noise in B236 and X1b40

	power	C_{xx}	C_{yy}	C_{xy}
B236	25 μW	< 0.01	< 0.02	< 0.01
X1B40	10 μW	< 0.004	< 0.04	< 0.01

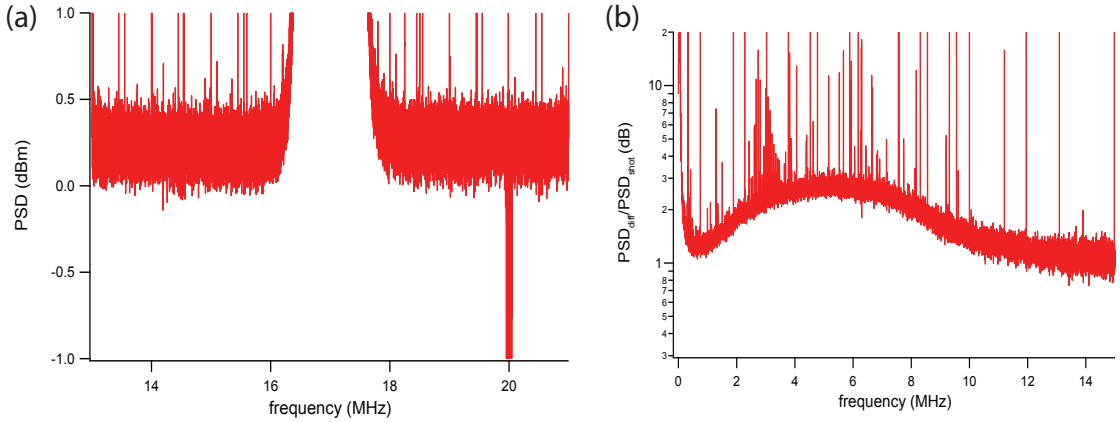

Figure C.4: Measurements of classical amplitude noise C_{yy}. (a) B236 Data from delayed-Line heterodyne technique with the balanced detection. The detected spectrum is normalized to the shot noise spectrum with the balanced detection.. (b) X1B40 Data from delayed-Line homodyne technique. The detected spectrum is normalized to the shot noise spectrum.

Appendix D

Light and Mechanics Spectra with Laser Classical Noise

Following the goal of previous appendix, bounding the size of laser classical noise effects, my goal here is to investigate the optomechanical spectra with laser classical noise.

D.1 Three effects from the classical noise

Like the quantum shot noise effects discussed in Appendix B (Eq. B.5), classical amplitude and phase noise of the laser incident on the cavity give rise to three different noise terms in the output optical spectrum: 1) $S_{\mathrm{c,ln}}(\omega)$, the transmitted laser classical noise itself, 2) $S_{\mathrm{c,disp}}(\omega)$, a component of the measured mechanical motion driven by the radiation pressure of laser classical noise, and 3) $S_{c,\mathrm{corr}}(\omega)$, the interference of the previous two terms.

The expression for the full spectrum therefore has lots of terms. Fortunately, the linear superposition principle allows us to divide the derivation. The classical noise contribution can be calculated without considering the shot noise and the mechanical thermal noise because these noise source are not correlated. Therefore, I can write the output light operator $\hat{d}_o$ and membrane position operator $\hat{x}$ as:

$$\hat{d}_o = \sqrt{\kappa_L}\sqrt{\kappa_R}\chi_c(\omega)\Big\{\frac{1}{2}(\delta x + i\delta y) - ig\bar{a}\hat{x}\Big\} \tag{D.1}$$

$$\hat{x} = -\frac{1}{2}\frac{2\omega_m}{\mathbb{N}(\omega)}g\bar{a}\Big\{\delta x\pi_+(\omega) + \delta y\pi_-(\omega)\Big\} \tag{D.2}$$

$$= -\frac{i}{2}\chi_m^{\mathrm{eff}}(\omega)\Big\{\delta x\pi_+(\omega) + \delta y\pi_-(\omega)\Big\} \tag{D.3}$$

With these two equations, we are ready to calculate the output spectrum. For the heterodyne detection without phase locking, the red sideband spectrum $S_{\rm red}(\omega)$ can be calculated by $\left\langle \hat{d}_o(-\omega)\hat{d}_o^\dagger(\omega)\right\rangle$, while the blue sideband $S_{\rm blue}(\omega)$ can be calculated by $\left\langle \hat{d}_o^\dagger(-\omega)\hat{d}_o(\omega)\right\rangle$. To distinct the three effects in both sidebands, we define

$$\left\langle \hat{d}_o(-\omega)\hat{d}_o^\dagger(\omega)\right\rangle = S_{\rm red}(\omega) = S_{\rm c,ln}^{\rm red}(\omega) + S_{\rm c,disp}^{\rm red}(\omega) + S_{\rm c,corr}^{\rm red}(\omega) \tag{D.4}$$

$$\left\langle \hat{d}_o^\dagger(-\omega)\hat{d}_o(\omega)\right\rangle = S_{\rm blue}(\omega) = S_{\rm c,ln}^{\rm blue}(\omega) + S_{\rm c,disp}^{\rm blue}(\omega) + S_{\rm c,corr}^{\rm blue}(\omega). \tag{D.5}$$

Note that here we assume the local oscillator beam has negligible classical noise per power compared with the signal beam. It follows that the classical noise floor are given by

$$\begin{aligned} S_{\rm c,ln}^{\rm red}(\omega) =& \frac{1}{4}\epsilon_d\kappa_L\kappa_R\left|\chi_c(-\omega)\right|^2(C_{xx}+C_{yy}) \equiv \frac{1}{4}f(-\omega)\left(\tilde{C}_{xx}+\tilde{C}_{yy}\right) \\ S_{\rm c,ln}^{\rm blue}(\omega) =& \frac{1}{4}\epsilon_d\kappa_L\kappa_R\left|\chi_c(\omega)\right|^2(C_{xx}+C_{yy}) \equiv \frac{1}{4}f(\omega)\left(\tilde{C}_{xx}+\tilde{C}_{yy}\right), \end{aligned} \tag{D.6}$$

where $f(\omega) \equiv \epsilon_d\kappa_R\left|\chi_c(\omega)\right|^2 = \epsilon\kappa\left|\chi_c(\omega)\right|^2$, $\tilde{C}_{xx} = \kappa_L C_{xx}$, and $\tilde{C}_{yy} = \kappa_L C_{yy}$. Note that C_{xx}, C_{yy}, and C_{xy} is a function of laser power or $\bar{a}$. The spectra of the mechanical motion driven by the radiation pressure of the laser classical noise are:

$$S_{\rm c,disp}^{\rm red}(\omega) = f(-\omega)(g\bar{a})^2|\chi_m^{\rm eff}(\omega)|^2\Gamma n_{\rm c,ba} \tag{D.7}$$

$$S_{\rm c,disp}^{\rm blue}(\omega) = f(\omega)(g\bar{a})^2|\chi_m^{\rm eff}(\omega)|^2\Gamma n_{\rm c,ba} \tag{D.8}$$

$$n_{\rm c,ba} = \frac{(g\bar{a})^2}{4\Gamma}\Big(\left|\pi_+(\omega)\right|^2\tilde{C}_{xx} + \left|\pi_-(\omega)\right|^2\tilde{C}_{yy} - 4\mathbb{I}m\left[\chi_c(-\omega)\chi_c(\omega)\right]\tilde{C}_{xy}\Big). \tag{D.9}$$

The interference spectra are:

$$\begin{aligned} S_{c,\rm corr}^{\rm red}(\omega) =& \frac{1}{2}f(-\omega)(g\bar{a})^2\{\tilde{C}_{xx}\mathbb{I}m\left[i\chi_m^{\rm eff}(\omega)\pi_+(\omega)\right] - \tilde{C}_{xy}\mathbb{I}m\left[i\chi_m^{\rm eff}(\omega)\pi_-(\omega)\right] \\ &+ \tilde{C}_{xy}\mathbb{R}e\left[i\chi_m^{\rm eff}(\omega)\pi_+(\omega)\right] - \tilde{C}_{yy}\mathbb{R}e\left[i\chi_m^{\rm eff}(\omega)\pi_-(\omega)\right]\} \\ S_{c,\rm corr}^{\rm blue}(\omega) =& \frac{1}{2}f(\omega)(g\bar{a})^2\{-\tilde{C}_{xx}\mathbb{I}m\left[i\chi_m^{\rm eff}(\omega)\pi_+(\omega)\right] + \tilde{C}_{xy}\mathbb{I}m\left[i\chi_m^{\rm eff}(\omega)\pi_-(\omega)\right] \\ &+ \tilde{C}_{xy}\mathbb{R}e\left[i\chi_m^{\rm eff}(\omega)\pi_+(\omega)\right] - \tilde{C}_{yy}\mathbb{R}e\left[i\chi_m^{\rm eff}(\omega)\pi_-(\omega)\right]\}. \end{aligned} \tag{D.10}$$

Fig. D.1 show all three classical noise effects on sideband spectra under excessive phase noise. See the caption for their qualitative features.

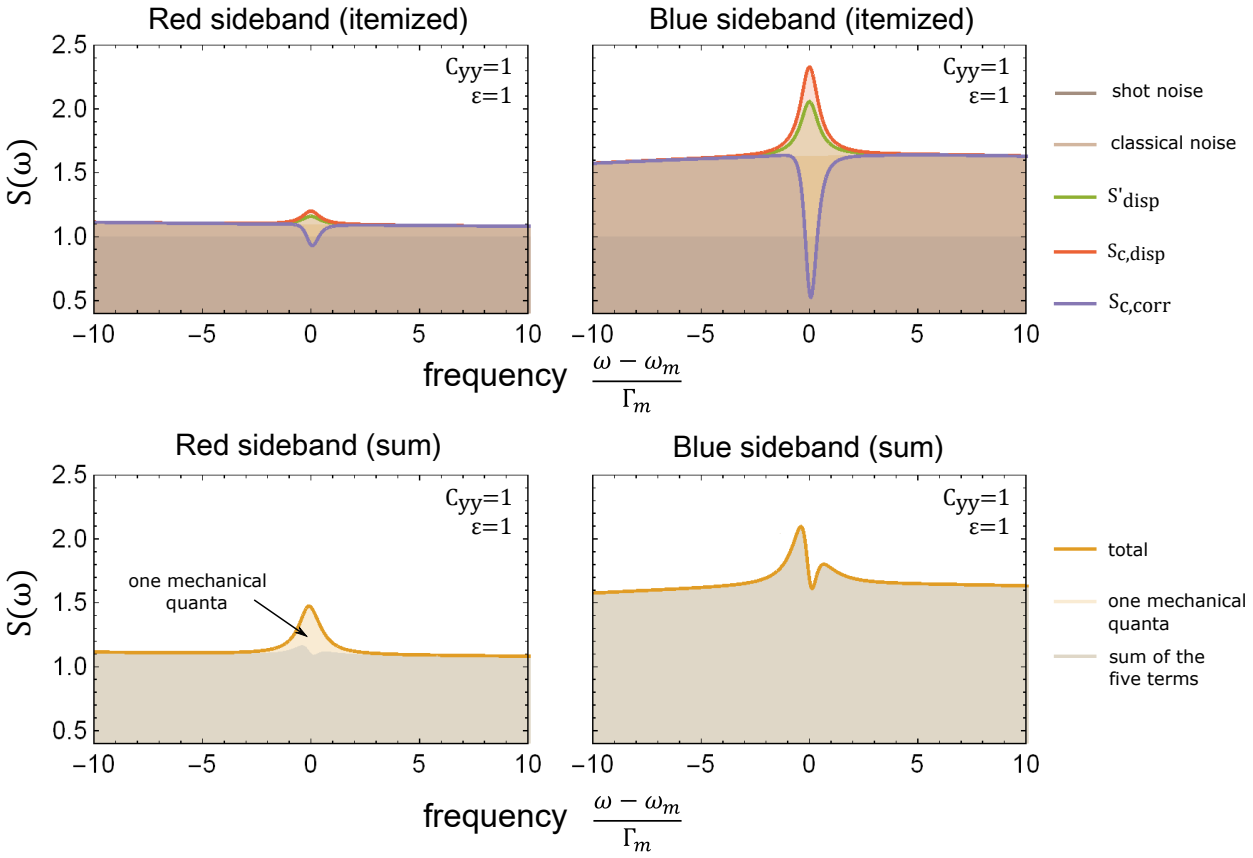

Figure D.1: (Color) Illustration of classical noise effects on red and blue sideband spectra. Here we model a red-detuned laser with excessive classical phase noise. The quantum efficiency is assumed to be perfect, 1. The upper two plots show each classical noise effects on the spectra, while the lower two plots show the sum of classical noise effects and the overall shapes. $S'_{\rm disp}$: the spectrum of the mechanical motion if there is no classical noise. The classical noise floor (as well as the size of other classical noise effects) is asymmetric on both sidebands due to cavity susceptibility. The shot noise floor remain symmetric. $S_{\rm c,disp}$ is always positive. $S_{\rm c,corr}$ is negative when there is excessive classical phase noise. In general, $S_{\rm c,corr}$ can be positive or negative (Eq. D.10). For the overall shapes, spectrum with one mechanical quanta noise is added to the red sideband due to the "sideband asymmetry" arising from the zero-point motion and the correlation of RPSN and shot noise [93]. The parameters are: $C_{xx} = 0.002$ and $C_{yy} = 1$ at laser power of 5 μW, $\epsilon = 1$, $g\bar{a}/2\pi = 1.4 \times 10^5$, $\omega_m/2\pi = 1.48$ MHz, $Q_m = 8 \times 10^6$, $\kappa/2\pi$=2.6 MHz, $\Delta/2\pi = -1.62$ MHz, $T_{\rm bath} = 360$ mK.

D.2 Error analysis in ratio thermometry

In this section, we analysis the systematic error in sideband-asymmetry thermometry due to laser classical noise. As shown in Fig. D.1, the three effects described in the previous section modify the sideband ratio R. This is a source of systematic measurement error to the phonon occupation measurement. Namely,

$$\Delta\bar{n} = \frac{1}{R^{\text{est}}/s - 1} - \frac{1}{R/s - 1}, \tag{D.11}$$

where R^{est} is the modified sideband ratio and s is the sideband ratio due to cavity susceptibility only.

The first noise term contributes local white noise to both sidebands with different size on top of the shot noise floor. This causes a systematic error due to the normalization in our data analysis. We normalize the spectra such that the noise floor is 1, the value of shot noise in our theory. Therefore we introduce an extra factor in the sideband-ratio:

$$R^{\text{est}}/s = \frac{\bar{n}+1}{\bar{n}} \Bigg/ \frac{1+S^{\text{red}}_{\text{c,ln}}}{1+S^{\text{red}}_{\text{c,ln}}} = R/s \Bigg/ \frac{1+S^{\text{red}}_{\text{c,ln}}}{1+S^{\text{red}}_{\text{c,ln}}}. \tag{D.12}$$

The second and the third noise terms comprise the majority of the laser noise error. They add or subtract the sideband height. Here we convert their contributions into unit of mechanical quanta and express their effects on modified sideband ratio as:

$$R^{\text{est}}/s = \frac{\bar{n} + 1 + \bar{n}_{\text{c,ba}} + \bar{n}^{\text{red}}_{\text{c,corr}}(\omega_m)}{\bar{n} + \bar{n}_{\text{c,ba}} + \bar{n}^{\text{blue}}_{\text{c,corr}}(\omega_m)} \tag{D.13}$$

where $n_{c,ba}$ come from the second noise, and $\bar{n}^{\text{red}}_{\text{c,corr}}(\omega_m)$ and $\bar{n}^{\text{blue}}_{\text{c,corr}}(\omega_m)$ are defined by

$$\begin{aligned}
\bar{n}^{\text{red}}_{\text{c,corr}}(\omega_m) \equiv & S^{\text{red}}_{\text{c,corr}}(\omega_m)/\{f^{\text{red}}(\omega)(g\bar{a})^2|\chi^{\text{eff}}_m(\omega)|^2\Gamma\} \\
\bar{n}^{\text{blue}}_{\text{c,corr}}(\omega_m) \equiv & S^{\text{blue}}_{c,\text{corr}}(\omega_m)/\{f^{\text{blue}}(\omega)(g\bar{a})^2|\chi^{\text{eff}}_m(\omega)|^2\Gamma\}
\end{aligned} \tag{D.14}$$

Here we apply the theory to analyze the effect of potential classical noise sources on the measurement of quantum backaction limit of optomechanical cooling in Ref. [98]. I plot the

classical noise effects in Fig. D.2 with the experimental parameters. Using Eq. D.11 andD.13, the error due to the classical noise of the cooling laser is bounded by $\Delta\bar{n}_{\mathrm{laser}} \approx 0.006$. Another systematic error is the presence of o-resonant substrate mechanical modes that rise above the shot noise oor [4, 99, 16]. The normalization of sideband amplitude in our analysis to the o-resonant shot noise level is aected by this noise. However, since $\bar{n}$ is a function of the sideband ratio, not their absolute amplitudes, it is not strongly aected, and again leads to a small $\Delta\bar{n}_{\mathrm{sub}} \approx 0.006$. Additional confirmation of the substrate noise's small effect is that the measured mechanical sidebands retain a Lorentzian lineshape [90] as shown by comparing Fig. D.1 and Fig. D.2. Because both laser noise and substrate noise are small, we otherwise do not include the eects of classical noise directly in the data presentation in Ref. [98].

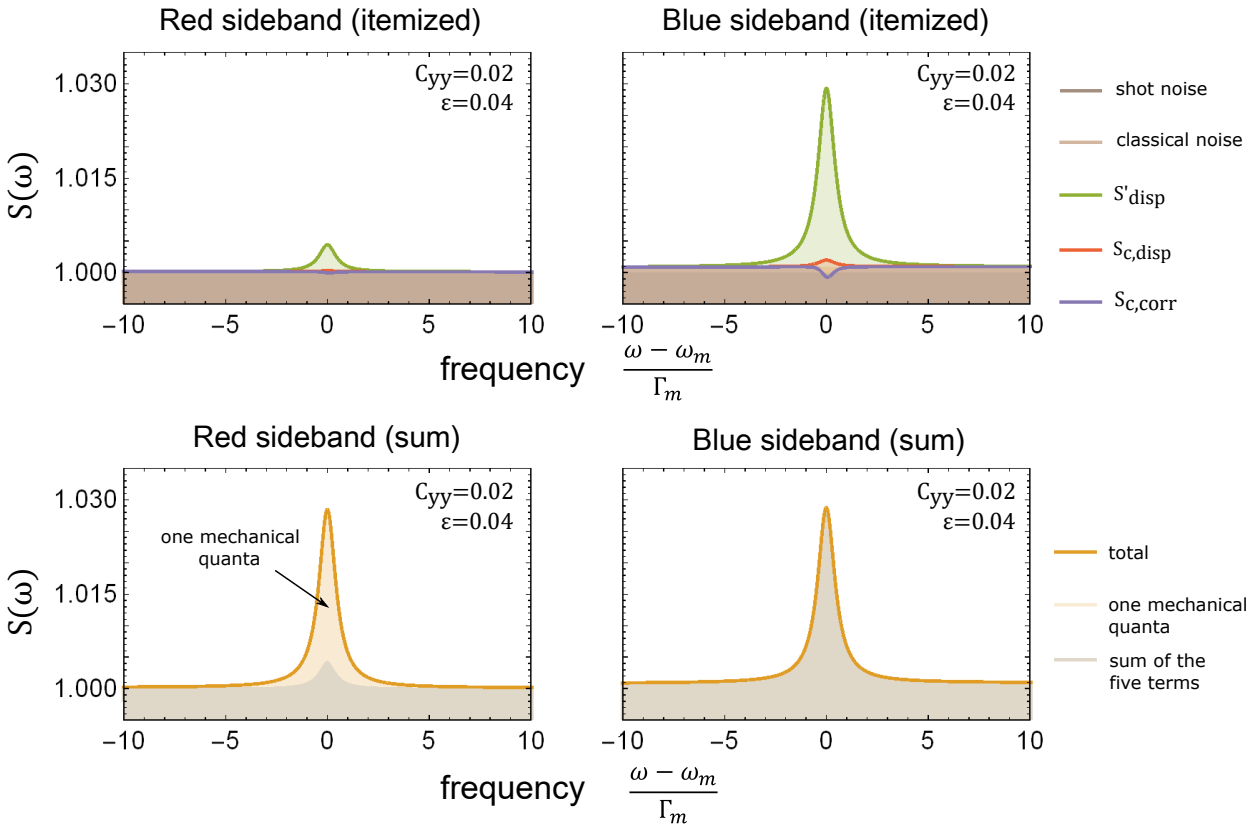

Figure D.2: (Color) An example of sideband spectra with small laser classical noise and small quantum efficiency. Here we plot each classical noise effect and the sum of them as in Fig. D.1. The effect due to laser classical noise floor is negligible. The other two effects are small and have opposite signs. These plots indicate that classical amplitude and phase noise are not significant systematic errors in the measurement of quantum backaction noise ($S'_{\rm disp}$). The parameters are set to: $C_{xx} = 0.002$ and $C_{yy} = 0.02$ at laser power of 5 μW, $\epsilon = 0.04$, $g\bar{a}/2\pi = 1.4 \times 10^5$, $\omega_m/2\pi = 1.48$ MHz, $Q_m = 8 \times 10^6$, $\kappa/2\pi$=2.6 MHz, $\Delta/2\pi = -1.62$ MHz, $T_{\rm bath} = 360$ mK.

Bibliography

[1] M. Aspelmeyer, T. J. Kippenberg, and F. Marquardt, "Cavity optomechanics," Rev. Mod. Phys. **86**, 1391 (2014), URL http://link.aps.org/doi/10.1103/RevModPhys.86.1391.

[2] B. M. Zwickl, W. E. Shanks, A. M. Jayich, C. Yang, A. C. Bleszynski Jayich, J. D. Thompson, and J. G. E. Harris, "High quality mechanical and optical properties of commercial silicon nitride membranes," Appl. Phys. Lett. **92**, 103125 (2008), URL http://dx.doi.org/10.1063/1.2884191.

[3] J. D. Thompson, B. M. Zwickl, A. M. Jayich, F. Marquardt, S. M. Girvin, and J. G. E. Harris, "Strong dispersive coupling of a high-finesse cavity to a micromechanical membrane," Nature **452**, 72 (2008), URL http://www.nature.com/nature/journal/vaop/ncurrent/full/nature06715.html.

[4] T. P. Purdy, R. W. Peterson, P.-L. Yu, and C. A. Regal, "Cavity optomechanics with SiN membranes at cryogenic temperatures," New J. Phys. **14**, 115021 (2012), URL http://dx.doi.org/10.1088/1367-2630/14/11/115021.

[5] T. P. Purdy, R. W. Peterson, and C. A. Regal, "Observation of Radiation Pressure Shot Noise on a Macroscopic Object," Science **339**, 801 (2013), URL http://www.sciencemag.org/content/339/6121/801.short.

[6] T. P. Purdy, P.-L. Yu, R. W. Peterson, N. S. Kampel, and C. A. Regal, "Strong Optomechanical Squeezing of Light," Phys. Rev. X **3**, 031012 (2013), URL http://link.aps.org/doi/10.1103/PhysRevX.3.031012.

[7] T. P. Purdy, P.-L. Yu, N. S. Kampel, R. W. Peterson, K. Cicak, R. W. Simmonds, and C. A. Regal, "Optomechanical Raman-ratio thermometry," Phys. Rev. A **92**, 031802(R) (2015), URL http://link.aps.org/doi/10.1103/PhysRevA.92.031802.

[8] R. W. Andrews, R. W. Peterson, T. P. Purdy, K. Cicak, R. W. Simmonds, C. A. Regal, and K. W. Lehnert, "Bidirectional and efficient conversion between microwave and optical light," Nature Phys. **10**, 321 (2014), URL http://dx.doi.org/10.1038/nphys2911.

[9] S. S. Verbridge, J. M. Parpia, R. B. Reichenbach, L. M. Bellan, and H. G. Craighead, "High quality factor resonance at room temperature with nanostrings under high tensile stress," J. Appl. Phys. **99**, 124304 (2006), URL http://scitation.aip.org/content/aip/journal/jap/99/12/10.1063/1.2204829.

[10] D. R. Southworth, R. A. Barton, S. S. Verbridge, B. Ilic, a. D. Fefferman, H. G. Craighead, and J. M. Parpia, "Stress and Silicon Nitride: A Crack in the Universal Dissipation of Glasses," Phys. Rev. Lett. **102**, 225503 (2009), URL http://link.aps.org/doi/10.1103/PhysRevLett.102.225503.

[11] Q. P. Unterreithmeier, T. Faust, and J. P. Kotthaus, "Damping of Nanomechanical Resonators," Phys. Rev. Lett. **105**, 027205 (2010), URL http://link.aps.org/doi/10.1103/PhysRevLett.105.027205.

[12] S. Schmid, K. D. Jensen, K. H. Nielsen, and A. Boisen, "Damping mechanisms in high-Q micro and nanomechanical string resonators," Phys. Rev. B **84**, 165307 (2011), URL http://link.aps.org/doi/10.1103/PhysRevB.84.165307.

[13] I. Wilson-Rae, R. Barton, S. Verbridge, D. Southworth, B. Ilic, H. Craighead, and J. Parpia, "High-Q Nanomechanics via Destructive Interference of Elastic Waves," Physical Review Letters **106**, 1 (2011), URL http://link.aps.org/doi/10.1103/PhysRevLett.106.047205.

[14] P.-L. Yu, Magnetic reconnection : from resistive MHD to two-fluid physics, Tech. Rep. (2012).

[15] P.-L. Yu, T. P. Purdy, G. D. Cole, and C. A. Regal, "New Directions in High-Q Optomechanical Membrane Resonators," CLEO: Science and Innovations (OSA Technical Digest) p. No. CW3F.8 (2013).

[16] P.-L. Yu, K. Cicak, N. S. Kampel, Y. Tsaturyan, T. P. Purdy, R. W. Simmonds, and C. A. Regal, "A phononic bandgap shield for high-Q membrane microresonators," Appl. Phys. Lett. **104**, 023510 (2014), URL http://scitation.aip.org/content/aip/journal/apl/104/2/10.1063/1.4862031.

[17] J. D. Teufel, T. Donner, D. Li, J. W. Harlow, M. S. Allman, K. Cicak, A. J. Sirois, J. D. Whittaker, K. W. Lehnert, and R. W. Simmonds, "Sideband cooling of micromechanical motion to the quantum ground state," Nature **475**, 359 (2011), URL http://dx.doi.org/10.1038/nature10261.

[18] C. A. Regal and K. W. Lehnert, "From cavity electromechanics to cavity optomechanics," JPCS **264**, 012025 (2011), URL http://dx.doi.org/10.1088/1742-6596/264/1/012025.

[19] J. Taylor, A. Sorensen, C. Marcus, and E. Polzik, "Laser Cooling and Optical Detection of Excitations in a LC Electrical Circuit," Phys. Rev. Lett. **107**, 273601 (2011), URL http://link.aps.org/doi/10.1103/PhysRevLett.107.273601.

[20] P. Rabl, P. Cappellaro, M. V. G. Dutt, L. Jiang, J. R. Maze, and M. D. Lukin, "Strong magnetic coupling between an electronic spin qubit and a mechanical resonator," Phys. Rev. B **79**, 1 (2009), URL http://link.aps.org/doi/10.1103/PhysRevB.79.041302.

[21] C. Zener, "Internal Friction in Solids II. General Theory of Thermoelastic Internal Friction," Phys. Rev. **53**, 90 (1938), URL http://link.aps.org/doi/10.1103/PhysRev.53.90.

[22] A. W. Leissa, Vibration of plates (NASA, Washington, D.C., 1969), ISBN 9781420053951.

[23] S. Timoshenko, Vibration Problems in Engineering (D. Van Nostrand Company, Inc., New York, 1937).

[24] G. Sosale, K. Das, L. Fréchette, and S. Vengallatore, "Controlling damping and quality factors of silicon microcantilevers by selective metallization," J. Microelectromech. Syst. **21**, 105010 (2011), URL http://dx.doi.org/10.1088/0960-1317/21/10/105010.

[25] B. S. Berry and W. C. Pritchet, "Deffect studies of thin layers by the vibrating-reed technique," J. Phys. Colloques **42**, C5 (1981), URL http://dx.doi.org/10.1051/jphyscol:19815172.

[26] M. Prieler, H. G. Bohn, W. Schilling, and H. Trinkaus, "Grain boundary sliding in thin substrate-bonded Al films," J. Alloys Compd. **211/212**, 424 (1994), URL http://www.sciencedirect.com/science/article/pii/0925838894905363.

[27] F. Hoehne, Y. A. Pashkin, O. Astafiev, L. Faoro, L. B. Ioffe, Y. Nakamura, and J. S. Tsai, "Damping in high-frequency metallic nanomechanical resonators," Phys. Rev. B **81**, 184112 (2010), URL http://link.aps.org/doi/10.1103/PhysRevB.81.184112.

[28] I. Wilson-Rae, R. A. Barton, S. S. Verbridge, D. R. Southworth, B. Ilic, H. G. Craighead, and J. M. Parpia, "High-Q Nanomechanics via Destructive Interference of Elastic Waves," Phys. Rev. Lett. **106**, 047205 (2011), URL http://link.aps.org/doi/10.1103/PhysRevLett.106.047205.

[29] A. Jockel, M. T. Rakher, M. Korppi, S. Camerer, D. Hunger, M. Mader, and P. Treutlein, "Spectroscopy of mechanical dissipation in micro-mechanical membranes," Appl. Phys. Lett. **99**, 143109 (2011), URL http://link.aip.org/link/?APPLAB/99/143109/1.

[30] A. K. Pandey, O. Gottlieb, O. Shtempluck, and E. Buks, "Performance of an AuPd micromechanical resonator as a temperature sensor," Appl. Phys. Lett. **96**, 203105 (2011).

[31] T. Larsen, S. Schmid, L. Gronberg, A. O. Niskanen, J. Hassel, S. Dohn, and A. Boisen, "Ultrasensitive string-based temperature sensors," Appl. Phys. Lett. **98**, 121901 (2011), URL http://dx.doi.org/10.1063/1.3567012.

[32] M. D. LeHaye, O. Buu, B. Camarota, and K. C. Schwab, "Approaching the quantum limit of a nanomechanical resonator," Science **304**, 74 (2004), URL http://www.sciencemag.org/content/304/5667/74.

[33] C. A. Regal, J. D. Teufel, and K. W. Lehnert, "Measuring nanomechanical motion with a microwave cavity interferometer," Nature Phys. **4**, 555 (2008), URL http://dx.doi.org/10.1038/nphys974.

[34] U. Kemiktarak, M. Metcalfe, M. Durand, and J. Lawall, "Mechanically compliant grating reflectors for optomechanics," Appl. Phys. Lett. **100**, 061124 (2012), URL http://link.aip.org/link/APPLAB/v100/i6/p061124/s1{&}Agg=doi.

[35] C. H. Bui, J. Zheng, S. W. S. Hoch, L. Y. T. Lee, J. G. E. Harris, and C. W. Wong, "High-reflectivity, high-Q micromechanical membranes via guided resonances for enhanced optomechanical coupling," Appl. Phys. Lett. **100**, 021110 (2012), URL http://link.aip.org/link/APPLAB/v100/i2/p021110/s1{&}Agg=doi.

[36] S. Chakram, Y. S. Patil, L. Chang, and M. Vengalattore, "Dissipation in ultrahigh quality factor SiN membrane resonators," Phys. Rev. Lett. **112**, 127201 (2013), URL http://link.aps.org/doi/10.1103/PhysRevLett.112.127201.

[37] L. Villanueva and S. Schmid, "Evidence of surface loss as ubiquitous limiting damping mechanism in SiN micro-and nanomechanical resonators," Phys. Rev. Lett. **113**, 227201 (2014), URL http://link.aps.org/doi/10.1103/PhysRevLett.113.227201.

[38] D. J. Wilson, C. A. Regal, S. B. Papp, and H. J. Kimble, "Cavity optomechanics with stoichiometric SiN films," Phys. Rev. Lett. **103**, 207204 (2009), URL http://link.aps.org/doi/10.1103/PhysRevLett.103.207204.

[39] B. M. Zwickl, Progress Toward Observation of Radiation Pressure Shot Noise, Ph.D. thesis, Yale University (2011).

[40] V. Narayanamurti, H. L. Störmer, M. A. Chin, A. C. Gossard, and W. Wiegmann, "Selective Transmission of High-Frequency Phonons by a Superlattice: The "Dielectric" Phonon Filter," Phys. Rev. Lett. **43**, 2012 (1979), URL http://link.aps.org/doi/10.1103/PhysRevLett.43.2012.

[41] M. M. Sigalas and E. N. Economou, "Elastic and acoustic wave band structure," J. Sound Vib. **158**, 377 (1992), URL http://www.sciencedirect.com/science/article/pii/0022460X92900597.

[42] M. S. Kushwaha, P. Halevi, L. Dobrzynski, and B. Djafari-Rouhani, "Acoustic band structure of periodic elastic composites," Phys. Rev. Lett. **71**, 2022 (1993), URL http://link.aps.org/doi/10.1103/PhysRevLett.71.2022.

[43] R. Martínez-Sala, J. Sancho, J. V. Sánchez, V. Gómez, J. Llinares, and F. Meseguer, "Sound attenuation by sculpture," Nature **378**, 241 (1995), URL http://dx.doi.org/10.1038/378241a0.

[44] M. Maldovan, "Sound and heat revolutions in phononics," Nature **503**, 209 (2013), URL http://dx.doi.org/10.1038/nature12608.

[45] S. Mohammadi, A. A. Eftekhar, W. D. Hunt, and A. Adibi, "High-Q micromechanical resonators in a two-dimensional phononic crystal slab," Appl. Phys. Lett. **94**, 051906 (2009), URL http://link.aip.org/link/?APPLAB/94/051906/1.

[46] J. Chan, T. P. M. Alegre, A. H. Safavi-Naeini, J. T. Hill, A. Krause, S. Groeblacher, M. Aspelmeyer, and O. Painter, "Laser cooling of a nanomechanical oscillator into its quantum ground state," Nature **478**, 89 (2011), URL http://www.nature.com/nature/journal/v478/n7367/abs/nature10461.html.

[47] A. H. Safavi-Naeini and O. Painter, "Design of optomechanical cavities and waveguides on a simultaneous bandgap phononic-photonic crystal slab," Opt. Express **18**, 14926 (2010), URL http://www.opticsinfobase.org/oe/abstract.cfm?uri=oe-18-14-14926.

[48] T. P. M. Alegre, A. Safavi-Naeini, M. Winger, and O. Painter, "Quasi-two-dimensional optomechanical crystals with a complete phononic bandgap," Opt. Express **19**, 5658 (2010), URL http://www.opticsinfobase.org/oe/abstract.cfm?uri=oe-19-6-5658.

[49] Y. Tsaturyan, Understanding and engineering high- Q micro-mechanical resonators in COMSOL, Tech. Rep. (2013).

[50] V. B. Braginsky and F. Y. Khalili, Quantum Measurement (Cambridge University Press, Melbourne, 1992).

[51] C. M. Caves, "Quantum-mechanical noise in an interferometer," Phys. Rev. D **23**, 1693 (1981), URL http://dx.doi.org/10.1103/PhysRevD.23.1693.

[52] W. G. Unruh, "Quantum Noise and QND Measurements," in "Quantum Optics, Experimental Gravitation, and Measurement Theory," , edited by P. Meystre and M. O. Scully (Plenum, New York, 1982), p. 661.

[53] M. T. Jaekel and S. Reynaud, "Quantum Limits in Interferometric Measurements," Europhys. Lett. **13**, 301 (1990), URL http://dx.doi.org/10.1209/0295-5075/13/4/003.

[54] H. J. Kimble, Y. Levin, A. B. Matsko, K. S. Thorne, and S. P. Vyatchanin, "Conversion of conventional gravitational-wave interferometers into quantum nondemolition interferometers by modifying their input and/or output optics," Phys. Rev. D **65**, 1 (2001), 0008026, URL http://link.aps.org/doi/10.1103/PhysRevD.65.022002.

[55] R. E. Slusher, L. W. Hollberg, B. Yurke, J. C. Mertz, and J. F. Valley, "Observation of Squeezed States Generated by Four-Wave Mixing in an Optical Cavity," Phys. Rev. Lett. **55**, 2409 (1985), URL http://link.aps.org/doi/10.1103/PhysRevLett.55.2409.

[56] R. M. Shelby, M. D. Levenson, S. H. Perlmutter, R. G. DeVoe, and D. F. Walls, "Broad-Band Parametric Deamplification of Quantum Noise in an Optical Fiber," Phys. Rev. Lett. **57**, 691 (1986), URL http://link.aps.org/doi/10.1103/PhysRevLett.57.691.

[57] L.-A. Wu, H. J. Kimble, J. L. Hall, and H. Wu, "Generation of Squeezed States by Parametric Down Conversion," Phys. Rev. Lett. **57**, 2520 (1986), URL http://link.aps.org/doi/10.1103/PhysRevLett.57.2520.

[58] T. Eberle, S. Steinlechner, J. Bauchrowitz, V. Händchen, H. Vahlbruch, M. Mehmet, H. Müller-Ebhardt, and R. Schnabel, "Quantum Enhancement of the Zero-Area Sagnac Interferometer Topology for Gravitational Wave Detection," Phys. Rev. Lett. **104**, 251102 (2010), URL http://link.aps.org/doi/10.1103/PhysRevLett.104.251102.

[59] The LIGO Scientific Collaboration, "A gravitational wave observatory operating beyond the quantum shot-noise limit," Nat. Phys. **7**, 962 (2011), URL http://dx.doi.org/doi:10.1038/nphys2083.

[60] M. A. Taylor, J. Janousek, V. Daria, J. Knittel, B. Hage, H.-A. Bachor, and W. P. Bowen, "Biological measurement beyond the quantum limit," Nature Photonics **7**, 229 (2013).

[61] M. A. Castellanos-Beltran, K. D. Irwin, G. C. Hilton, L. R. Vale, and K. W. Lehnert, "Amplification and squeezing of quantum noise with a tunable Josephson metamaterial," Nature Phys. **4**, 929 (2008).

[62] L. Hilico, J. M. Courty, C. Fabre, E. Giacobino, I. Abram, and J. L. Oudar, "Squeezing with χ-3 materials," Appl. Phys. B **55**, 202 (1992), URL http://dx.doi.org/10.1007/BF00325007.

[63] C. Fabre, M. Pinard, S. Bourzeix, A. Heidmann, E. G. S. Reynaud, E. Giacobino, and S. Reynaud, "Quantum-noise reduction using a cavity with a movable mirror," Phys. Rev. A **49**, 1337 (1994), URL dx.doi.org/10.1103/PhysRevA.49.1337.

[64] S. Mancini and P. Tombesi, "Quantum noise reduction by radiation pressure," Phys. Rev. A **49**, 4055 (1994), URL http://link.aps.org/doi/10.1103/PhysRevA.49.4055.

[65] T. Corbitt, Y. Chen, F. Khalili, D. Ottaway, S. Vyatchanin, S. Whitcomb, and N. Mavalvala, "Squeezed-state source using radiation-pressure-induced rigidity," Phys. Rev. A **73**, 23801 (2006), URL http://link.aps.org/doi/10.1103/PhysRevA.73.023801.

[66] V. B. Braginskii, A. B. Manukin, V. B. Braginsky, and A. B. Manukin, "Ponderomotive effects of electromagnetic radiation," Sov. Phys. JETP **25**, 653 (1967).

[67] A. Heidmann, Y. Hadjar, and M. Pinard, "Quantum nondemolition measurement by optomechanical coupling," Appl. Phys. B **64**, 173 (1997), URL http://link.springer.com/10.1007/s003400050162.

[68] A. Dorsel, J. D. McCullen, P. Meystre, E. Vignes, and H. Walther, "Optical bistability and mirror confinement induced by radiation pressure," Phys. Rev. Lett. **51**, 1550 (1983), URL http://dx.doi.org/10.1103/PhysRevLett.51.1550.

[69] D. W. C. Brooks, T. Botter, S. Schreppler, T. P. Purdy, N. Brahms, and D. M. Stamper-Kurn, "Non-classical light generated by quantum-noise-driven cavity optomechanics." Nature **488**, 476 (2012), URL http://www.ncbi.nlm.nih.gov/pubmed/22895194.

[70] A. Safavi-Naeini, S. Gröblacher, J. Hill, J. Chan, M. Aspelmeyer, and O. Painter, "Squeezed light from a silicon micromechanical resonator," Nature **500**, 185 (2013), URL http://www.nature.com/nature/journal/v500/n7461/abs/nature12307.html.

[71] C. Gerry and P. Knight, Introductory Quantum Optics (Cambridge University Press, New York, 2004).

[72] H.-A. Bachor and T. C. Ralph, A Guide to Experiments in Quantum Optics (WILEY-VCH, Weinheim, Germany, 2004), 2nd ed.

[73] R. W. Boyd, Nonlinear Optics (Academic Press, New York, 2008).

[74] J. P. Dakin, D. J. Pratt, J. N. Ross, and G. W. Bibby, "Distributed Anti-Stokes Ratio Thermometry," in "Proc. Conf. on Optical-Fiber Sensors 3," (San Diego, 1985), URL http://dx.doi.org/10.1364/OFS.1985.PDS3.

[75] T. R. Hart, R. L. Aggarwal, and B. Lax, "Temperature Dependence of Raman Scattering in Silicon," Phys. Rev. B **1**, 638 (1970), URL http://link.aps.org/doi/10.1103/PhysRevB.1.638.

[76] B. J. Kip and R. J. Meier, "Determination of the Local Temperature at a Sample during Raman Experiments Using Stokes and Anti-Stokes Raman Bands," Appl. Spectrosc. **44**, 707 (1990), URL http://www.opticsinfobase.org/as/abstract.cfm?uri=as-44-4-707.

[77] J. B. Cui, K. Amtmann, J. Ristein, and L. Ley, "Noncontact temperature measurements of diamond by Raman scattering spectroscopy," J. Appl. Phys. **83**, 7929 (1998), URL http://scitation.aip.org/content/aip/journal/jap/83/12/10.1063/1.367972.

[78] A. C. Eckbreth, Laser Diagnostics for Combustion Temperature and Species (Gordon and Breach, Amsterdam, Netherlands, 1996), 2nd ed.

[79] A. H. Safavi-Naeini, J. Chan, J. T. Hill, T. P. M. Alegre, A. Krause, and O. Painter, "Observation of Quantum Motion of a Nanomechanical Resonator," Phys. Rev. Lett. **108**, 1 (2012), URL http://link.aps.org/doi/10.1103/PhysRevLett.108.033602.

[80] N. Brahms, T. Botter, S. Schreppler, D. W. C. Brooks, and D. M. Stamper-Kurn, "Optical Detection of the Quantization of Collective Atomic Motion," Phys. Rev. Lett. **108**, 133601 (2012), URL http://link.aps.org/doi/10.1103/PhysRevLett.108.133601.

[81] A. J. Weinstein, C. U. Lei, E. E. Wollman, J. Suh, A. Metelmann, A. A. Clerk, and K. C. Schwab, "Observation and interpretation of motional sideband asymmetry in a quantum electro-mechanical device," Phys. Rev. X **041003** (2014), URL http://link.aps.org/doi/10.1103/PhysRevX.4.041003.

[82] F. Diedrich, J. C. Bergquist, W. M. Itano, and D. J. Wineland, "Laser Cooling to the Zero-Point Energy of Motion," Phys. Rev. Lett. **62**, 403 (1989), URL http://link.aps.org/doi/10.1103/PhysRevLett.62.403.

[83] C. Monroe, D. M. Meekhof, B. E. King, S. R. Jefferts, W. M. Itano, D. J. Wineland, and P. Gould, "Resolved-Sideband Raman Cooling of a Bound Atom to the 3D Zero-Point Energy," Phys. Rev. Lett. **75**, 4011 (1995), URL http://link.aps.org/doi/10.1103/PhysRevLett.75.4011.

[84] P. S. Jessen, C. Gerz, P. D. Lett, W. D. Phillips, S. L. Rolston, R. J. C. Spreeuw, and C. I. Westbrook, "Observation of quantized motion of Rb atoms in an optical field," Phys. Rev. Lett. **69**, 49 (1992), URL http://link.aps.org/doi/10.1103/PhysRevLett.69.49.

[85] A. M. Kaufman, B. J. Lester, and C. A. Regal, "Cooling a Single Atom in an Optical Tweezer to Its Quantum Ground State," Phys. Rev. X **2**, 41014 (2012), URL http://link.aps.org/doi/10.1103/PhysRevX.2.041014.

[86] F. Marquardt, J. P. Chen, A. A. Clerk, and S. M. Girvin, "Quantum Theory of Cavity-Assisted Sideband Cooling of Mechanical Motion," Phys. Rev. Lett. **99**, 093902 (2007), URL http://link.aps.org/doi/10.1103/PhysRevLett.99.093902.

[87] I. Wilson-Rae, N. Nooshi, W. Zwerger, and T. J. Kippenberg, "Theory of Ground State Cooling of a Mechanical Oscillator Using Dynamical Backaction," Phys. Rev. Lett. **99**, 093901 (2007), URL http://link.aps.org/doi/10.1103/PhysRevLett.99.093901.

[88] Y. Tsaturyan, A. Barg, A. Simonsen, L. G. Villanueva, S. Schmid, A. Schliesser, and E. S. Polzik, "Demonstration of suppressed phonon tunneling losses in phononic bandgap shielded membrane resonators for high-Q optomechanics," Opt. Express **22**, 6810 (2014), URL http://www.opticsexpress.org/abstract.cfm?URI=oe-22-6-6810.

[89] S. Weis, R. Rivière, S. Deleglise, E. Gavartin, O. Arcizet, A. Schliesser, and T. J. Kippenberg, "Optomechanically Induced Transparency," Science **330**, 1520 (2010), URL http://dx.doi.org/10.1126/science.1195596.

[90] A. M. Jayich, J. C. Sankey, K. Borkje, D. Lee, C. Yang, M. Underwood, L. Childress, A. Petrenko, S. M. Girvin, and J. G. E. Harris, "Cryogenic optomechanics with a Si3N4 membrane and classical laser noise," New J. Phys. **14**, 115018 (2012), URL iopscience.iop.org/1367-2630/14/11/115018.

[91] A. Pontin, C. Biancofiore, E. Serra, A. Borrielli, F. S. Cataliotti, F. Marino, G. A. Prodi, M. Bonaldi, F. Marin, and D. Vitali, "Frequency-noise cancellation in optomechanical systems for ponderomotive squeezing," Phys. Rev. A **89**, 033810 (2014), URL http://link.aps.org/doi/10.1103/PhysRevA.89.033810.

[92] A. B. Shkarin, N. E. Flowers-Jacobs, S. W. Hoch, A. D. Kashkanova, C. Deutsch, J. Reichel, and J. G. E. Harris, "Optically Mediated Hybridization between Two Mechanical Modes," Phys. Rev. Lett. **112**, 013602 (2014), URL http://link.aps.org/doi/10.1103/PhysRevLett.112.013602.

[93] F. Y. Khalili, H. Miao, H. Yang, A. H. Safavi-Naeini, O. Painter, and Y. Chen, "Quantum back-action in measurements of zero-point mechanical oscillations," Phys. Rev. A **86**, 1 (2012), URL http://link.aps.org/doi/10.1103/PhysRevA.86.033840.

[94] A. Bokaian, "Natural frequencies of beams under tensile axial loads," J. Sound Vib **142**, 481 (1990), URL http://dx.doi.org/10.1016/0022-460X(90)90663-K.

[95] S. Schmid, B. Malm, and A. Boisen, "Quality factor improvement of silicon nitride micro string resonators," Micro Electro Mechanical Systems (MEMS), 2011 IEEE 24th International Conference pp. 481–484 (2011), URL http://ieeexplore.ieee.org/lpdocs/epic03/wrapper.htm?arnumber=5734466.

[96] T. Botter, D. W. C. Brooks, N. Brahms, S. Schreppler, and D. M. Stamper-Kurn, "Linear amplifier model for optomechanical systems," Phys. Rev. A **85**, 13812 (2012), URL http://link.aps.org/doi/10.1103/PhysRevA.85.013812.

[97] D. Walls and G. J. Milburn, Quantum Optics (Springer-Verlag, Berlin, 2008), ISBN 978-3-540-28573-1.

[98] R. W. Peterson, T. P. Purdy, N. S. Kampel, R. W. Andrews, P.-L. Yu, K. W. Lehnert, and C. A. Regal, "Laser cooling of a micromechanical membrane to the quantum backaction limit," to be appeared in Phys. Rev. Lett. (2016), URL http://arxiv.org/abs/1510.03911.

[99] Y. Zhao, D. J. Wilson, K.-K. Ni, and H. J. Kimble, "Suppression of extraneous thermal noise in cavity optomechanics," Opt. Express **20**, 3586 (2012), URL https://www.osapublishing.org/oe/abstract.cfm?uri=oe-20-4-3586.